Alma Mater Studiorum · University of Bologna

School of Science
Department of Physics and Astronomy
Master Degree in Physics

Neutrino beam monitoring with the SAND detector at the DUNE near site

Supervisor:
Prof. Gabriele Sirri

Submitted by:
Francesco Barilari

Co-supervisors:
Dr. Matteo Tenti
Dr. Federico Battisti

Academic Year 2023/2024

Abstract

The Deep Underground Neutrino Experiment (DUNE) is a next-generation long-baseline neutrino experiment, consisting of a new high-intensity beam facility, a Near Detector at Fermilab, and a Far Detector with four liquid Argon time-projection chambers located at $\sim$ 1300 km distance. The Near Detector will include three distinct detectors, one of which, SAND (System for on-Axis Neutrino Detection), will play a crucial role in constraining systematic uncertainties to validate the measurements obtained at the Far Detector. For this purpose, beam monitoring is critical for detecting any potential variations of the beam caused by issues in accelerator operations. This study investigates the feasibility of beam monitoring by analyzing the muon momentum distributions obtained from the simulations of neutrino interactions in the SAND upstream calorimeter. A set of 93 different neutrino beam anomalies were considered, and the SAND beam monitoring capabilities were analyzed using two-sample hypothesis testing.

Contents

Introduction

Since their discovery, neutrino oscillations have become one of the most direct evidence that the Standard Model of particle physics is not a complete theory and must be extended. Over the years, many parameters that govern oscillations have been measured, exploiting different experimental techniques and different neutrino sources, both artificial and natural. However, some questions in this field remain open, and the DUNE experiment aims to address some of them.

DUNE will be a next-generation long-baseline accelerator neutrino experiment. Its main goal is to measure the CP violation neutrino oscillation parameter (δ_{CP}) and determine the neutrino mass ordering. The experiment will consist of a new high-intensity beam facility, a Near Detector Complex at Fermilab, and a Far Detector with four liquid argon time projection Chambers located at $\sim$ 1300 km distance.

The Near Detector will include three distinct detectors, one of which, SAND (System for on-Axis Neutrino Detection), is permanently located on axis and will play a crucial role in constraining systematic uncertainties to validate the measurements obtained at the Far Detector. The other two detectors NDLAr, NDGAr will be moving off-axis to measure the beam profile.

SAND consists of a magnet, an electromagnetic calorimeter, an inner tracker, and a Liquid Argon target. The magnet and the calorimeter will be re-used from the KLOE experiment which ran in Frascati until 2018. The inner tracker is a stack of graphite or polyethylene targets and straw tubes.

The study of beam monitoring is a critical aspect of neutrino experiments as it allows for the detection of potential anomalies in the beam or target complex.

This thesis investigates the feasibility of performing beam monitoring using the SAND detector. The primary objective is to assess the ability of the SAND detector to identify variations in the neutrino beam, with particular attention to events that interact in the front calorimeter and have muons correctly reconstructed in the inner tracker.

The analysis is based on a simulated sample corresponding to 4.4×10^{18} Protons on Target (POT), or 20 hours of beam time. The sample selection focuses on charged current events with energies below 20 GeV, where the muon is reconstructed. The study first characterizes neutrino interactions within this sample, including muon momentum reconstruction efficiency and resolution, as well as the distribution of vertex positions.

A set of 93 different neutrino beam anomalies were considered, and the beam monitoring is carried out by comparing the nominal reconstructed muon momentum spectrum with the varied one, utilizing two-sample tests, such as the Kolmogorov-Smirnov and Anderson-Darling tests.

The dissertation is organized as follows:

- **Chapter 1** gives an overview of neutrino physics, considering both the theoretical aspect, focusing on the neutrino oscillation phenomenon, and the current experimental results;
- **Chapter 2** describes the DUNE experiment and its main scientific goals;
- **Chapter 3** describes the SAND detector, its components, and its experimental physics opportunities;
- **Chapter 4** describes the simulation tools used, also considering the input and the output of each step;
- **Chapter 5** describes the analysis performed and the obtained results.

Chapter 1

Neutrino physics

The Standard Model of particles is a theory that classifies all the fundamental particles according to their properties also introduces rules that determine which interactions are possible and their rates. It was developed in the second half of the 20th century and all fundamental particles in it have been discovered, the last being the Higgs bosons [1, 2]. It works very well in the predicting a wide variety of phenomena but there are some of them that need an explanation beyond it. Phenomena like dark matter, neutrino oscillations and others that cannot be explained using only the Standard Model, so it must be extended. Moreover, it does not include a description of gravity.

In this Chapter, we will discuss about how neutrinos, and the interactions in which they are involved, are described in the Standard Model. We will also discuss some experiments that measured neutrino oscillation parameters.

1.1 Flavor and mass terms in the Lagrangian

The Standard Model (SM) is a theory based on the symmetry group $SU(3)_C \times SU(2)_L \times U(1)_Y$ where C, L, Y refer respectively to color, left-handed and weak hypercharge. In particular the group $SU(3)_C$ describes the strong interaction while the group $SU(2)_L \times U(1)_Y$ the electroweak one. The fundamental particles contained in it are: spin-$\frac{1}{2}$ fermions (quarks and leptons), spin-1 mediator bosons and a spin-0 Higgs boson. The list of fundamental particles is reported in Fig. (1.1). Fermions are organized in left-handed doublets and right-handed singlets under the $SU(2)_L$ gauge group. Leptons only experience the electro-weak force and their doublets are organized in three generations as follow:

$$\begin{pmatrix} \nu_e \\ e^- \end{pmatrix} \begin{pmatrix} \nu_\mu \\ \mu^- \end{pmatrix} \begin{pmatrix} \nu_\tau \\ \tau^- \end{pmatrix}$$

The important parameters in the electroweak interaction are the electric charge (Q), the third component of the isospin (I_3) and the weak hypercharge (Y) that are connected by the Gell-Mann-Nishijima relation:

$$Q = I_3 + \frac{Y}{2} \tag{1.1}$$

Neutrinos are colorless neutral particles, so they participate only in weak processes, which are mediated by the Z^0 (neutral current) and $W^\pm$ (charged current) bosons. The terms

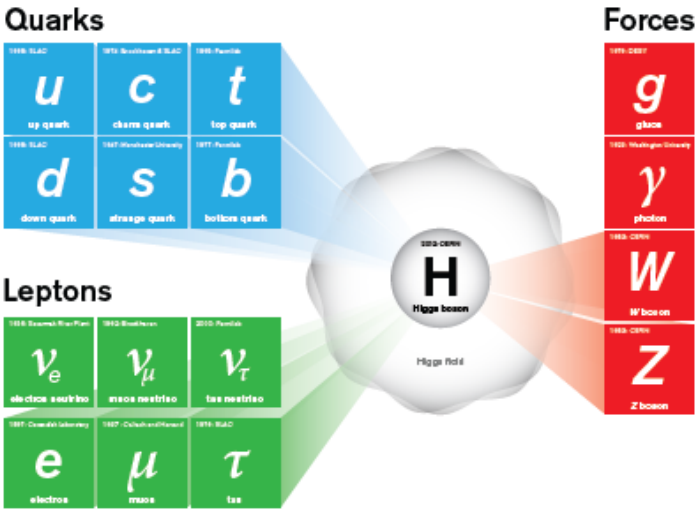

Figure 1.1: Scheme of particles in the Standard Model. They are divided in fermions and bosons. fermion are divided in quark, that feel strong interaction, and leptons that do not [3].

in electroweak Lagrangian that regulate these processes are:

$$\mathscr{L}^{CC} = -\frac{g}{2\sqrt{2}} j_\alpha^{CC} W^\alpha \tag{1.2}$$

$$\mathscr{L}^{NC} = -\frac{g}{2\cos\theta_W} j_\alpha^{NC} Z^\alpha \tag{1.3}$$

Neutrino fields, decomposed in chiral terms, are described by the equations of motion

$$i\gamma^\mu \partial_\mu \nu_L = m\nu_R \qquad\qquad i\gamma^\mu \partial_\mu \nu_R = m\nu_L \tag{1.4}$$

that can be deduced by the Dirac Lagrangian

$$\mathscr{L} = \overline{\nu_L} i\partial\!\!\!/ \nu_L + \overline{\nu_R} i\partial\!\!\!/ \nu_R - m(\overline{\nu_L}\nu_R + \overline{\nu_R}\nu_L) \tag{1.5}$$

From the Madame Wu experiment [4], which indicates that neutrino violates maximally the parity symmetry, neutrinos are assumed massless in the Standard Model.

The evidence of neutrino oscillation proved that neutrinos must have a mass different from zero, so the Standard Model must be extended. The *minimally extended Standard Model*, the simplest extension of it, includes also the right-handed component of the neutrino fields, that are therefore singlets for the $SU(2)_L$ group and do not feel the weak interaction (*sterile neutrinos*). In this framework, lepton sector is organized as follow [5]:

$$L'_L = \begin{pmatrix} \nu'_L \\ \ell'_L \end{pmatrix} \quad \nu'_R \quad \ell'_R$$

where L'_L is the weak doublet while ℓ'_R and ν'_R are respectively the right-handed components of charged leptons and of neutrinos. Using this simple extension, the Higgs-Yukawa Lagrangian, that uses the Higgs mechanism to give mass to the particles, is:

$$\mathscr{L}_{H,L} = -\sum_{\alpha\beta=e,\mu,\tau} \left[Y'^{\ell}_{\alpha\beta}\, \overline{L'_{\alpha L}}\, \Phi\, \ell'_{\beta R} + Y'^{\nu}_{\alpha\beta}\, \overline{L'_{\alpha L}}\, \tilde{\Phi}\, \nu'_{\beta R} \right] + h.c. \tag{1.6}$$

where Φ and $\tilde{\Phi}$ are:

$$\Phi = \frac{1}{\sqrt{2}} \begin{pmatrix} 0 \\ v + H \end{pmatrix} \qquad \tilde{\Phi} = i\sigma_2 \Phi^* = \frac{1}{\sqrt{2}} \begin{pmatrix} v + H \\ 0 \end{pmatrix} \tag{1.7}$$

The factors Y'^l and Y'^ν are 3×3 complex matrices that can be diagonalized applying the unitary transformations

$$V_L^{\nu\dagger} Y'^\nu V_R^\nu = Y^\nu \qquad V_L^{l\dagger} Y'^\ell V_R^l = Y^\ell \tag{1.8}$$

with

$$Y_{kj}^\nu = y_k^\nu \delta_{kj} \tag{1.9}$$

After these transformations, the neutrino mass eigenstates, the ones that diagonalizes the matrices, are:

$$\mathbf{n}_L = V_L^{\nu\dagger} \nu_L' = \begin{pmatrix} \nu_{1L} \\ \nu_{2L} \\ \nu_{3L} \end{pmatrix} \qquad \mathbf{n}_R = V_R^{\nu\dagger} \nu_R' = \begin{pmatrix} \nu_{1R} \\ \nu_{2R} \\ \nu_{3R} \end{pmatrix} \tag{1.10}$$

Thus, the eq (1.6) can be rewritten as:

$$\mathscr{L}_{H,L} = -\left(\frac{v + H}{\sqrt{2}}\right) \left[\sum_{\alpha=e,\mu,\tau} y_\alpha^\ell \, \overline{\ell_{\alpha L}} \, \ell_{\alpha R} + \sum_{k=1}^{3} y_k^\nu \, \overline{\nu}_{kL} \, \nu_{kR} \right] + h.c. \tag{1.11}$$

The terms that multiply v describe the mass of the particles while the terms with H describe the interaction with the Higgs field. For what concerns neutrino masses, they are expressed as:

$$m_k = \frac{y_k^\nu v}{\sqrt{2}} \tag{1.12}$$

As the other particles that acquire mass with this mechanism, also in this case the mass of the particle (neutrino) depends on the *vacuum expectation value* (v). The term y_k^ν is a free parameter of the theory and there is no explanation, in the Standard Model, of its smallness. To find the neutrino flavor eigenstates involved in the weak interactions is useful to write the leptonic weak charged current (the one mediated by W bosons)

$$j_{W,L}^\mu = 2\,\overline{\nu}_L' \gamma^\mu \ell_L' = 2\,\overline{n}_L V_L^{\nu\dagger} V_L^\ell \gamma^\mu \ell_L = 2\,\overline{n}_L U \gamma^\mu \ell_L = 2\,\overline{\nu}_L \gamma^\mu \ell_L \tag{1.13}$$

where ν_L are the flavor eigenstates and are related to the mass ones by

$$\boldsymbol{\nu}_L = U \mathbf{n}_L \tag{1.14}$$

The matrix U is called PMNS (Pontecorvo-Maki-Nakagawa-Sakata) matrix and is parametrized as:

$$U^{PMNS} = \begin{pmatrix} c_{12}c_{13} & s_{12}c_{13} & s_{13}e^{-i\delta} \\ -s_{12}c_{23} - c_{12}s_{23}s_{13}e^{i\delta} & c_{12}c_{23} - s_{12}s_{23}s_{13}e^{i\delta} & s_{23}c_{13} \\ s_{12}s_{23} - c_{12}c_{23}s_{13}e^{i\delta} & -c_{12}s_{23} - s_{12}c_{23}s_{13}e^{i\delta} & c_{23}c_{13} \end{pmatrix} \tag{1.15}$$

where c_{ij} and s_{ij} are respectively the cosine and the sine of the mixing angle between the mass states indicated as subscript. The parameter δ describes instead the CP violation:

the difference in behavior between ν and $\overline{\nu}$. The PMNS matrix can be factorized in three different submatrices each considering the mixing between two different states only (as in a two flavor case).

$$U = \begin{pmatrix} 1 & 0 & 0 \\ 0 & c_{23} & s_{23} \\ 0 & -s_{23} & c_{23} \end{pmatrix} \begin{pmatrix} c_{13} & 0 & s_{13}e^{-i\delta} \\ 0 & 1 & 0 \\ -s_{13}e^{i\delta} & 0 & c_{13} \end{pmatrix} \begin{pmatrix} c_{12} & s_{12} & 0 \\ -s_{12} & c_{12} & 0 \\ 0 & 0 & 1 \end{pmatrix} \tag{1.16}$$

1.2 Neutrino as Majorana particle

As seen before, a massive neutrino can be described by a 4-components Dirac spinor only introducing the RH component of it; using just the LH chiral field, it is possible to describe only the massless case. However, it is not the only way to do it; in fact Majorana in 1937 [6] discovered that it is possible to resolve (1.4), in the massive case, using a two-components spinor. The way to do it is to assume that the two components of the Dirac spinor are not independent, but related by:

$$\nu_R = \mathcal{C}\,\overline{\nu_L}^T = \nu_L^C \tag{1.17}$$

where $\mathcal{C}$ is the conjugation matrix. The Dirac equations became in this way the Majorana equation for the left-handed field:

$$i\gamma^\mu \partial_\mu \nu_L = m\nu_L^C \tag{1.18}$$

Decomposing the field in its chiral components and using the eq. (1.17) we obtain the Majorana relation:

$$\nu = \nu_L + \nu_R = \nu_L + \nu_L^C \tag{1.19}$$

or in other terms:

$$\nu = \nu^C \tag{1.20}$$

This implies also that neutrino field coincides with antineutrino one. This can be possible for neutral particle only by looking the Dirac equation for a fermion with charge q in a electromagnetic field A_μ:

$$(i\gamma^\mu \partial_\mu - q\gamma^\mu A_\mu - m)\nu = 0 \tag{1.21}$$

$$(i\gamma^\mu \partial_\mu + q\gamma^\mu A_\mu - m)\nu^C = 0 \tag{1.22}$$

Clearly, if $q \neq 0$ the two relations are different, so the only case in which is possible to use Majorana spinors is with neutrinos that are the only neutral fermions in the Standard Model. In the massless case the Majorana and Dirac descriptions are the same because only the left handed component of the Dirac field is involved. Differences arise in case of massive neutrinos and can be noted only looking at the effect that involve the mass: the *neutrinoless double β-decay*. This is a particular case of double beta decay possible only if neutrino is a Majorana particle. Looking at the spectrum of the sum of the electrons produced, it's possible to distinguish the Dirac case (continuous spectrum from zero to the Q-value of the reaction) from the Majorana one (spectrum as a delta peaked at the Q-value). The most important experiments in this field are double-beta decay experiments,

like CUORE [7]. In case of neutrinos as Majorana particles, also the PMNS matrix is modified adding two new phases to the theory:

$$U^M = U^{PMNS} \begin{pmatrix} 1 & 0 & 0 \\ 0 & e^{i\lambda_2} & 0 \\ 0 & 0 & e^{i\lambda_3} \end{pmatrix} \tag{1.23}$$

1.2.1 See-saw mechanism

Considering only one generation of neutrino, the chiral fields are the building blocks of the Lagrangian. The left-handed exists while the right-handed is allowed by the SM but we don't know if it exists. Assuming that also RH neutrino exists, the mass term for the Lagrangian is composed of:

$$\mathscr{L}^{D+M}_{mass} = \mathscr{L}^{L}_{mass} + \mathscr{L}^{R}_{mass} + \mathscr{L}^{D}_{mass} \tag{1.24}$$

The terms $\mathscr{L}^{L}_{mass}$ and $\mathscr{L}^{R}_{mass}$ describe respectively the Majorana mass terms for the LH and RH component of the field:

$$\mathscr{L}^{L}_{mass} = \frac{1}{2} m_L \nu_L \nu_L^T C^\dagger \nu_L + h.c. \tag{1.25}$$

$$\mathscr{L}^{R}_{mass} = \frac{1}{2} m_R \nu_R \nu_R^T C^\dagger \nu_R + h.c. \tag{1.26}$$

The term $\mathcal{L}^{D}_{mass}$ is instead the Dirac mass term:

$$\mathscr{L}^{D}_{mass} = -m_D \overline{\nu_R} \nu_L + h.c. \tag{1.27}$$

Using the column vector:

$$N_L = \begin{pmatrix} \nu_L \\ \nu_R^C \end{pmatrix} \tag{1.28}$$

it is possible to rewrite the Lagrangian in eq. (1.24) as

$$\mathscr{L}^{D+M}_{mass} = \frac{1}{2} N_L^T \mathscr{C}^\dagger M N_L + h.c. \tag{1.29}$$

with M the symmetric mass matrix:

$$M = \begin{pmatrix} m_L & m_D \\ m_D & m_R \end{pmatrix} \tag{1.30}$$

The LH Majorana term is not symmetric under the $SU(2)_L \times U(1)_Y$ transformation, so it is not allowed by the SM: the solution is to put the mass equal to zero ($m_L = 0$). The mass matrix is not diagonal, so the fields ν_L and ν_R are not mass eigenstates and they don't have a definite mass. A unitary transformation U is necessary to pass to the massive chiral fields

$$n_L = \begin{pmatrix} \nu_{1L} \\ \nu_{2L} \end{pmatrix} \tag{1.31}$$

and to diagonalize the matrix

$$U^T M U = \begin{pmatrix} m_1 & 0 \\ 0 & m_2 \end{pmatrix} \tag{1.32}$$

with m_1 and m_2 real and positive. An interesting case is the one in which:

$$m_D << m_R \qquad\qquad m_L = 0 \tag{1.33}$$

The mass of the massive field are:

$$m_1 \simeq \frac{m_D^2}{m_R} \tag{1.34}$$

$$m_2 \simeq m_R \tag{1.35}$$

It's evident that the ν_2 field is much heavier than the ν_1 field, that is very light. This is called *see-saw mechanism*. A very large mass difference is responsible of a small mixing angle, implying ν_1 to be composed mainly of active neutrino ν_L while ν_2 of sterile neutrino ν_R:

$$\nu_{1L} \simeq -i\nu_L \qquad\qquad \nu_{2L} \simeq \nu_R^C \tag{1.36}$$

This mechanism can be extended to the case of three active neutrinos but, in addition to that, also N_s right-handed neutrinos are present, which do not take part in the weak interaction. In this case, the column vector in eq. (1.28) becomes:

$$N_L' = \begin{pmatrix} \nu_{eL}' \\ \nu_{\mu L}' \\ \nu_{\tau L}' \\ \nu_{s_1 R}'^C \\ \vdots \\ \nu_{N_s R}'^C \end{pmatrix} \tag{1.37}$$

that contains $N = 3 + N_s$ elements. The number of right-handed neutrinos N_s is not limited by the theory. The Lagrangian term in eq. (1.24) ca be written as:

$$\mathscr{L}_{mass}^{D+M} = \frac{1}{2} N_L'^T \mathcal{C}^\dagger M^{D+M} N_L' + H.c. \tag{1.38}$$

where the matrix M^{D+M} is the $N \times N$ symmetric mass matrix:

$$M^{D+M} = \begin{pmatrix} M^L & M^{D^T} \\ M^D & M^R \end{pmatrix} \tag{1.39}$$

As done before, the Majorana left-handed part is forbidden by the Standard Model and must be set to zero Also in this case, the mass matrix is not diagonal and a unitary transformation U must be done in order to find the mass eigenstates

$$\boldsymbol{n} = \begin{pmatrix} \nu_1 \\ \vdots \\ \nu_N \end{pmatrix} \tag{1.40}$$

The diagonal mass matrix is:

$$U^T M U = \begin{pmatrix} M_l & 0 \\ 0 & M_h \end{pmatrix} \tag{1.41}$$

where M_l is the 3×3 diagonal mass matrix of the light neutrino fields while M_h is the $N_s \times N_s$ diagonal mass matrix of the heavy neutrinos. With the same considerations made before, it's possible to say that light neutrino states are composed mainly by the three active neutrinos already known, while the heavy neutrinos are composed of right-handed ones.

1.3 Oscillations

As said before, neutrino oscillations are the prove that neutrinos have a mass different from zero, differently from what expected from the Standard Model. This is very interesting because it means that neutrino physics can be the probe to go beyond the Standard Model, putting the attention of the researchers community on this branch of physics.

1.3.1 Oscillations in vacuum

Neutrino mass eigenstates and the flavor ones do not coincide. To pass from one basis to the other, there is the so called PMNS matrix [8].

$$\begin{pmatrix} \nu_1 \\ \nu_2 \\ \nu_3 \end{pmatrix} = U^{PMNS} \begin{pmatrix} \nu_e \\ \nu_\mu \\ \nu_\tau \end{pmatrix} \tag{1.42}$$

In this way it is possible to express a flavor eigenstate in terms of mass eigenstates and viceversa.

$$|\nu_\alpha\rangle = \sum_k U^*_{\alpha k} |\nu_k\rangle \qquad\qquad |\nu_k\rangle = \sum_\alpha U_{\alpha k} |\nu_\alpha\rangle \tag{1.43}$$

The massive neutrino states are eigenstates (denoted with latin letter) of the Hamiltonian

$$\mathcal{H} |\nu_k\rangle = E_k |\nu_k\rangle \tag{1.44}$$

with energy eigenvalues

$$E_k = \sqrt{\vec{p}^2 + m_k^2} \tag{1.45}$$

that evolve in time as plane waves

$$|\nu_k(t)\rangle = e^{-iE_k t} |\nu_k\rangle \tag{1.46}$$

Considering now a flavor eigenstate ν_α created at $t = 0$ that evolves in time, it is described, in term of the mass eigenstates, as

$$|\nu_\alpha(t)\rangle = \sum_k U^*_{\alpha k}\, e^{-iE_k t} |\nu_k\rangle \tag{1.47}$$

Using eq. (1.43), it is possible to substitute the mass eigenstates with the flavor ones, describing a certain flavor state at time t as superimposition of initial ones of same basis.

$$|\nu_\alpha(t)\rangle = \sum_{\beta=e,\mu,\tau} \left(\sum_k U^*_{\alpha k} e^{-iE_k t} U_{\beta k} \right) |\nu_\beta\rangle \tag{1.48}$$

So there is an amplitude different from zero for the transition $\nu_\alpha \to \nu_\beta$

$$A_{\nu_\alpha \to \nu_\beta}(t) = \langle \nu_\beta | \nu_\alpha(t) \rangle = \sum_k U^*_{\alpha k} U_{\beta k}\, e^{-iE_K t} \tag{1.49}$$

from which is possible to write the transition probability of the same process

$$P_{\nu_\alpha \to \nu_\beta}(t) = \left| A_{\nu_\alpha \to \nu_\beta}(t) \right|^2 = \sum_{k,j} U^*_{\alpha k} U_{\beta k} U_{\alpha j} U^*_{\beta j}\, e^{-i(E_K - E_j)t} \tag{1.50}$$

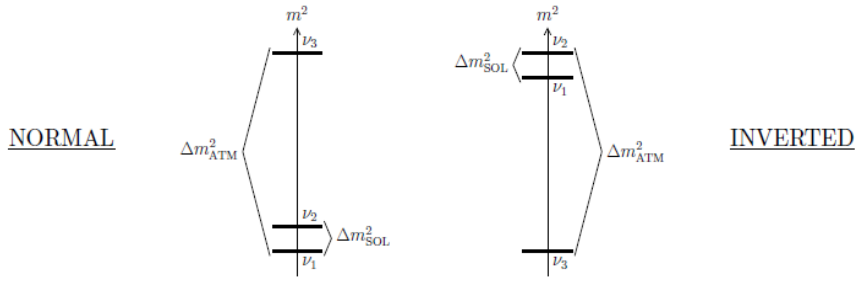

Figure 1.2: Representation of the mass hierarchy problem: the ordering between ν_1 and ν_2 is known while the one of ν_3 is still unknown. So, it can be the heaviest (normal ordering) or the lightest (inverted ordering) [9].

This is the phenomenon of oscillation: a certain neutrino flavor state created at $t = 0$ (at the source) can change its flavor at $t \neq 0$ (at the detector point). In the ultrarelativistic limit (always valid due to the smallness of the neutrinos masses) the energy dispersion relation can be approximated as

$$E_k \simeq E + \frac{m_k^2}{2E} \tag{1.51}$$

and the probability in eq. (1.50) is expressed as:

$$P_{\nu_\alpha \to \nu_\beta}(L, E) = \sum_{k,j} U^*_{\alpha k} U_{\beta k} U_{\alpha j} U^*_{\beta j}\, exp\left(-i \frac{\Delta m^2_{kj} L}{2E}\right) \tag{1.52}$$

where the term Δm^2_{kj} is the difference between the square of the mass eigenstates k and j

$$\Delta m^2_{kj} = m^2_k - m^2_j \tag{1.53}$$

so, it can be both positive or negative. Experiments found that the square mass difference Δm^2_{13} is of the same order of Δm^2_{23}. They are compatible with the value measured for atmospheric neutrinos, called atmospheric square mass difference. The problem here is that the sign of this value has not been measured. Instead for what concerns the Δm^2_{12} square mass difference, called solar mass difference, the sign has been measured: ν_1 state is lighter than ν_2. The situation can be summarized as:

$$\Delta m^2_{12} << \left|\Delta m^2_{13}\right| \simeq \left|\Delta m^2_{23}\right| \tag{1.54}$$

So, concerning the ordering of neutrino mass eigenstates, two different scenarios are possible: *normal hierarchy* and *inverted hierarchy*. In normal hierarchy the ordering of the mass states is $m_1 < m_2 < m_3$ while in inverted hierarchy is $m_3 < m_1 < m_2$ as shown in Fig (1.2).

Oscillation probability depends only on neutrino mass square differences, their mixing angles and the CP violation angle δ; so it is not possible to determine their absolute masses in oscillation experiments. There are other kind of experiments to do it, for examples the ones that study the endpoint of the beta decay like KATRIN [10].

1.3.2 Two flavors case

A simpler case with respect to the previous one regards the hypothesis of the presence of only two neutrino species. In this case, the PMNS matrix can be factorized in three mixing terms involving only two states. The mixing matrix becomes a simple 2×2 rotation matrix and the relation (1.42) can be written, considering for example only electron and muon neutrinos, as:

$$\begin{pmatrix}\nu_e\\ \nu_\mu\end{pmatrix} = \begin{pmatrix}\cos\theta & \sin\theta\\ -\sin\theta & \cos\theta\end{pmatrix}\begin{pmatrix}\nu_1\\ \nu_2\end{pmatrix} \tag{1.55}$$

Following the same steps as in the three neutrino species case, the superimposition relation at $t = 0$ and $t \neq 0$ are:

$$|\nu_e(t=0)\rangle = \cos\theta\,|\nu_1\rangle + \sin\theta\,|\nu_2\rangle \tag{1.56}$$

$$|\nu_e(t\neq0)\rangle = \cos\theta e^{-iE_1t}\,|\nu_1\rangle + \sin\theta e^{-iE_2t}\,|\nu_2\rangle \tag{1.57}$$

Recovering now the consideration made on the ultrarelativistic limit, the transition probability from a certain flavor to another one in eq. (1.50) becomes:

$$P_{\nu_e\to\nu_\mu}(L,E) = \sin 2\theta^2 \sin^2\left(1.27\,\Delta m^2\frac{L}{E}\right) \tag{1.58}$$

It is possible to define also the *survival probability* as the probability to not change the flavor and it is defined as the complementary to the transition one.

$$P_{\nu_e\to\nu_e}(L,E) = 1 - P_{\nu_e\to\nu_\mu}(L,E) \tag{1.59}$$

Oscillation probability and survival one for the two flavors case are shown in Fig. (1.3). Also from the figure, it is possible to see that the oscillation probability and the survival one are complementary.

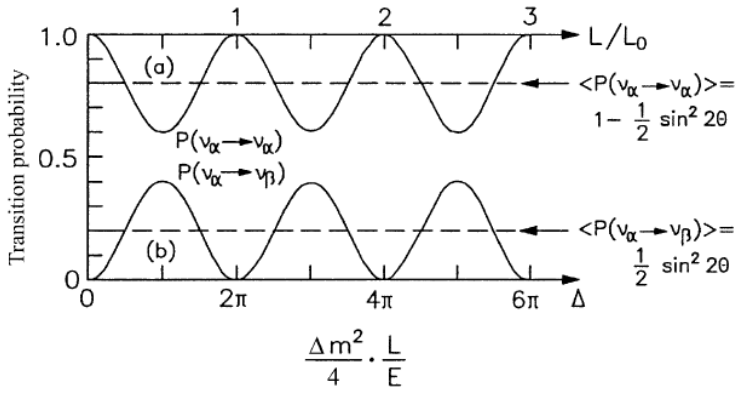

Figure 1.3: Transition and survival probability for the two-flavor case [11]. Dashed lines represent the mean.

1.3.3 Oscillations in matter

Oscillations of neutrinos in matter are different from those in vacuum because neutrinos can interact along their path. In particular, the differences arise from the behavior of electron neutrino. All neutrino species undergo weak NC interaction with matter, introducing

a potential in the Hamiltonian:

$$V_{NC} = -\frac{\sqrt{2}}{2} G_F \, n_n \tag{1.60}$$

where G_F is the Fermi constant and n_n the number density of neutron. Due to the fact that this interaction is felt in the same way by all neutrino species, this contribution gives no difference between the vacuum case. Neutrinos can undergo also CC interaction which introduces an additional potential in the Hamiltonian:

$$V_{CC} = \sqrt{2} \, G_F \, n_e \tag{1.61}$$

where n_e is the number density of electron. Given that electrons are the only leptons present in matter, CC interaction is felt by electron neutrinos only. This is the cause of the difference between oscillations in vacuum and in matter. This additional potential can be added to the vacuum Hamiltonian as:

$$\mathcal{H} = \mathcal{H}_{vacuum} + \mathcal{H}_{MSW} \tag{1.62}$$

which in the two flavor case can be written as:

$$\mathcal{H} = \frac{\Delta m^2}{4E} \begin{pmatrix} -\cos 2\theta & \sin 2\theta \\ \sin 2\theta & \cos 2\theta \end{pmatrix} + \begin{pmatrix} V_{CC} & 0 \\ 0 & 0 \end{pmatrix} \tag{1.63}$$

that can be diagonalized. The oscillation probability in eq (1.52) can be expressed using the effective angle θ_M and effective mass difference Δm^2_M

$$P_{\nu_e \to \nu_\mu}(L, E) = \sin 2\theta_M{}^2 \sin^2 \left(\frac{\Delta m^2_M L}{4E} \right) \tag{1.64}$$

where

$$\Delta m^2_M = \Delta m^2 \sqrt{\sin^2 (2\theta) + (\cos 2\theta - \zeta)^2} \tag{1.65}$$

$$\sin^2 2\theta_M = \frac{\sin^2 2\theta}{\sin^2 2\theta + (\cos 2\theta - \zeta)^2} \tag{1.66}$$

$$\zeta = \frac{2\sqrt{2} G_F n_e E}{\Delta m^2} \tag{1.67}$$

The term expressed in eq (1.67) is very interesting because it is sensitive to the sign of the mass square difference and can be used to established the hierarchy of the two mass eigenstates involved. Starting from these formulas, some considerations on matter oscillations can be done:

- if there is no matter ($\zeta \to 0$) the vacuum case is recovered;
- if $\theta = 0 \Rightarrow \theta_M = 0$; to have oscillation in matter, oscillation in vacuum are needed;
- if $\zeta \to \infty \Rightarrow \theta_M \to 0$; if the matter is very dense, the oscillation is suppressed even if it occurs in vacuum;
- there is a particular density (ζ_{max}) for which, even if the vacuum angle is tiny, the matter mixing angle is maximal ($\sin^2 2\theta_M = 1$).

$$\zeta_{max} = \frac{2\sqrt{2} \, G_F \, n_e \, E}{\Delta m^2} = \cos 2\theta$$

1.4 CP violation

CP violation in the lepton sector has the same formalism to the quark one. In particular there is CP violation if the conjugate of the PMNS matrix is different from the original one, in general:

$$U^* \neq U \Rightarrow \not{CP}$$

To be more precise, there are also other conditions for CP violation:

- no charged leptons or neutrino are degenerate in mass,
- mixing angles θ_{ij} different from 0 and $\pi/2$,
- CP phase δ_{CP} different from 0 and π.

These conditions are summarize by the relation:

$$\begin{aligned} -2\ J\ &(m^2_{\nu_2} - m^2_{\nu_1})(m^2_{\nu_3} - m^2_{\nu_1})(m^2_{\nu_3} - m^2_{\nu_2}) \\ &(m^2_{\nu_\mu} - m^2_{\nu_e})(m^2_{\nu_\tau} - m^2_{\nu_e})(m^2_{\nu_\tau} - m^2_{\nu_\mu}) \neq 0 \end{aligned} \tag{1.68}$$

where J is the Jarlskog invariant and can be expressed as:

$$\begin{aligned} J &= \mathrm{Im}\left[U_{e2}\ U^*_{e3}\ U^*_{\mu 2}\ U^*_{\mu 3}\right] \\ &= \frac{1}{8} \sin 2\theta_{12}\ \sin 2\theta_{23}\ \cos\theta_{13}\ \sin 2\theta_{13}\ \sin\delta_{CP} \end{aligned} \tag{1.69}$$

The CP transformation corresponds to the substitution of a neutrino with an antineutrino and viceversa reversing the helicity, so $\nu_\alpha \to \overline{\nu}_\alpha$. If there is CP violation, oscillation probability involving neutrino states should be different from the one involving antineutrino ones:

$$P_{\nu_\alpha \to \nu_\beta} \neq P_{\overline{\nu}_\alpha \to \overline{\nu}_\beta} \tag{1.70}$$

and an asymmetry should be observed

$$\mathcal{A}_{CP} = \frac{P_{\nu_\alpha \to \nu_\beta} - P_{\overline{\nu}_\alpha \to \overline{\nu}_\beta}}{P_{\nu_\alpha \to \nu_\beta} + P_{\overline{\nu}_\alpha \to \overline{\nu}_\beta}} \tag{1.71}$$

The experiments that have the aim to measure this parameter must be long baseline ($L \sim 300$ km) accelerator experiments. The parameter δ_{CP} would be strongly correlated to θ_{13}. Some experiments that have this goal are for examples T2K [12], DUNE, HK [13] and NOνA [14].

1.5 Neutrino experiments

Neutrino experiments can be classified in different ways considering different criteria. The first criterion is by the type of search they perform, in particular:

- **appearance mode:** if the experiment searches a neutrino specie different from the one in the beam, so it looks at the appearance probability;
- **disappearance mode:** if the experiment searches neutrinos of the same species of the beam ones, in this case it looks at the survival probability;

Another way to distinguish neutrino experiments is to look at the different types of sources.

- **solar neutrino:** neutrinos originated in the Sun during the *pp-chain* or *CNO-cycle*;
- **atmospheric neutrino:** neutrinos originated in the atmosphere from the interaction of primary cosmic rays;
- **reactor neutrino:** neutrino that are fission products of a reactor; in this case they are mainly electron antineutrinos;
- **accelerator neutrino:** neutrinos produced by an accelerator; In this case it is possible to place the detector off-axis in order to have a more monochromatic beam with respect to the on-axis case, which reduces the statistics.

In the last two cases (reactor and accelerator neutrino) it is possible to choose arbitrarily the distance between the source and the detection point in order to investigate only a certain value of Δm^2_{ij} parameters. Using this criterion, it is possible to make another classification of the neutrino experiments:

- **Short-Baseline (SBL):** these experiments can be accelerator or reactor ones
  - Reactor:
    $$\frac{L}{E} < 10 \text{ m/MeV} \implies \Delta m^2 > 0.1 \text{ eV}^2$$
  - Accelerator:
    $$\frac{L}{E} < 1 \text{ km/GeV} \implies \Delta m^2 > 1 \text{ eV}^2$$
- **Long-Baseline (LBL):** the source is the same as in the Short-Baseline case but the distance between the source and the detection point is different; also atmospheric neutrinos are included in this category
  - Reactor:
    $$\frac{L}{E} < 10^3 \text{ m/MeV} \implies \Delta m^2 > 10^{-3} \text{ eV}^2$$
  - Accelerator:
    $$\frac{L}{E} < 10^3 \text{ km/GeV} \implies \Delta m^2 > 10^{-3} \text{ eV}^2$$
  - Atmospheric:
    $$\frac{L}{E} < 10^4 \text{ km/GeV} \implies \Delta m^2 > 10^{-4} \text{ eV}^2$$
- **Very Long-Baseline (VLB):** the distance between source and detector is 10-100 times grater respect the Long-baseline one; also solar neutrinos can be included here
  - Reactor:
    $$\frac{L}{E} < 10^5 \text{ m/MeV} \implies \Delta m^2 > 10^{-5} \text{ eV}^2$$
  - Accelerator:
    $$\frac{L}{E} < 10^4 \text{ km/GeV} \implies \Delta m^2 > 10^{-4} \text{ eV}^2$$
  - Solar:
    $$\frac{L}{E} < 10^{12} \text{ m/MeV} \implies \Delta m^2 > 10^{-12} \text{ eV}^2$$

1.5.1 Solar neutrinos

They are electron neutrinos only and their flux is $6 \times 10^{10} \mathrm{cm}^{-2}\mathrm{s}^{-1}$ at an energy of the order of 1 MeV. The spectrum of neutrinos produced in the Sun is reported in Fig (1.4) where the sensitivity ranges of some experiments are reported. Despite the flux, detectors must be very large, due to the small cross section of this particles, and properly shielded to exclude cosmic ray interactions. Neutrinos from the Sun are produced mainly by *pp-chain* and *CNO-cycle*.

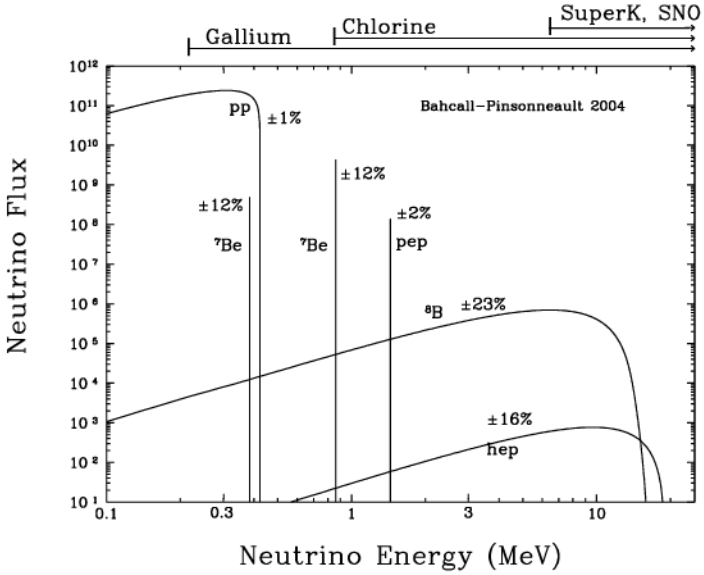

Figure 1.4: Neutrino spectra for each reaction in a star and the experiment sensitive to them [15].

Two main experimental techniques were developed for the detection of solar neutrinos: radiochemical and Cherenkov. The first counts the nuclei produced in neutrino reactions, whereas the second exploits Cherenkov light of leptons produced in charged current interactions.

The first experiment dedicated to the observation of solar neutrinos was Homestake [16] in 1970. The detector was composed of a single cylindrical tank with a volume of 370 m^3 filled with 615 tons of C_2Cl_4. It was located 1478 m below the surface, in the Homestake Gold Mine, in South Dakota. The dept of the detector is 4200 meters of water equivalent in order to shield the cosmic ray. The experiment exploited the inverse beta decay reaction:

$$\nu_e + {}^{37}\mathrm{Cl} \rightarrow {}^{37}\mathrm{Ar} + e^-$$

that has a threshold of $E_\nu^{th} = 0.814\, MeV$, so only medium and high energy neutrinos from the Sun, in particular the ^8B neutrinos, can take part in the process. Every two months, the C_2Cl_4 was extracted using a flow of helium and the number of Ar atoms produced are counted.

Throughout the years, other atoms were used as target for the reaction, for example Gallium:

$$\nu_e + {}^{71}\mathrm{Ga} \rightarrow {}^{71}\mathrm{Ge} + e^-$$

that has a threshold for the neutrino energy of $E_\nu^{th} = 0.233$ MeV, so it is sensitive to a larger number of reactions in the Sun. The experimental technique is the same and one of the most experiment that used this target was GALLEX, improved with GALLEX/GNO, at the Laboratori Nazionali del Gran Sasso (LNGS) [17]. It was made of 30 tons of Gallium and the extraction occurred every 3 weeks.

The other main experimental technique consists of the detection of Cherenkov light produced by charged lepton in the final state. In this way it is possible to reconstruct also direction, interaction point and energy of the neutrino. It also offers the possibility to monitor real-time neutrinos that arrive in the detector, making it possible to study the neutrino flux difference between day and night. Super-Kamiokande [18] is the most famous experiment that uses this technique. It is a 50,000 tons of water Cherenkov detector surrounded by PMTs. It exploits mainly the elastic scattering:

$$\nu_x + e^- \to \nu_x + e^-$$

The experiment has a threshold of $E_\nu = 4.7$ MeV, so it is sensitive only to ^8B neutrinos.

All these experiments agree that the number of detected neutrinos, considering the flux, the cross section and the efficiency of the detector, was less than expected by solar standard model, which predicted the number of neutrinos produced by a star: this is the so-called *Solar Neutrino Problem*. The solution of this problem is to consider the oscillation of electron neutrinos into the other flavors in the path between the Sun and the Earth. By the fact that the PMNS matrix can be factorized in three different sub-matrices, it is possible to consider only two eigenstates at a time. In the case of solar neutrinos, the states involved in the oscillation are ν_1 and ν_2 for the mass eigenstates and ν_e and ν_μ for the flavor ones, while oscillation into tau neutrinos can be neglected.

A new type of experiment, sensitive also to muon neutrinos was necessary to confirm this hypothesis. SNO (Sudbury Neutrino Observatory) was built with this goal [19]. The experiment has an onion-like structure: the inner part (the target for the reaction) is heavy water contained in an acrylic vessel, then there are PMTs to detect Cherenkov light, then an inner and an outer shielding made of normal water that act as VETO. Exploiting also deuterium (d) in heavy water, it can detect three different processes:

$$\nu_e + d \to p + p + e^-$$

$$\nu_x + d \to n + p + \nu_x$$

$$\nu_x + e^- \to \nu_x + e^-$$

The first reaction is mediated by charged current ($E_{th} = 1.4$ MeV), the second by neutral current ($E_{th} = 2.2$ MeV), while the third is an elastic scattering process. The data obtained from SNO are reported in Fig. (1.5), where the three colored bands correspond to CC, ES and NC fluxes. They intersect at the fit values of:

$$\phi^{CC} = (1.68 \pm 0.15) \times 10^6 \text{ cm}^{-2}\text{s}^{-1}$$

$$\phi^{NC} = (5.25 \pm 0.29) \times 10^6 \text{ cm}^{-2}\text{s}^{-1}$$

$$\phi^{ES} = (2.35 \pm 0.37) \times 10^6 \text{ cm}^{-2}\text{s}^{-1}$$

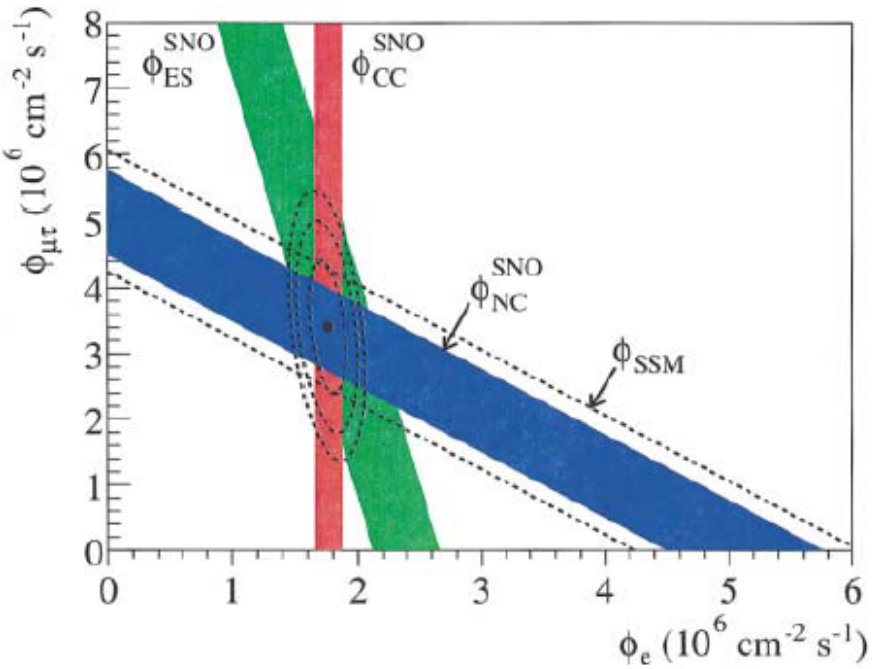

Figure 1.5: Flux of ^{8}B solar neutrinos which are μ or τ flavor vs the electron flux of electron neutrino in SNO [20]. Color bands intersect at the fit values for ϕ_e and $\phi_{\mu\tau}$, indicating that the combined flux results are consistent with neutrino flavor transformation assuming no distortion in the ^{8}B neutrino energy spectrum.

In particular, the value of neutral current, sensitive to all neutrino species is compatible to what expected by solar standard model, while the one of charged current, sensitive only to ^{8}B solar neutrinos, shows a reduction respect to the SSM. This is a confirmation of the oscillation hypothesis.

1.5.2 Atmospheric neutrinos

Atmospheric neutrinos are produced by the interaction of primary cosmic rays (mainly protons) with the atmosphere, as shown in Fig. (1.6). Primary cosmic rays produce secondary cosmic rays which have different components in them, in particular they include hadrons and their decay products [5]. In the production of atmospheric neutrinos the main process is the pion decay:

$$\pi^+ \rightarrow \mu^+ + \nu_\mu$$

$$\pi^- \rightarrow \mu^- + \overline{\nu}_\mu$$

Then muons decay in electrons and neutrinos in the reactions:

$$\mu^+ \rightarrow e^+ + \nu_e + \overline{\nu}_\mu$$

$$\mu^- \rightarrow e^- + \overline{\nu}_e + \nu_\mu$$

The typical energies of atmospheric neutrinos are in a range from 100 MeV to 100 GeV. Looking at their production process, it is possible to deduce the abundance of each neutrino

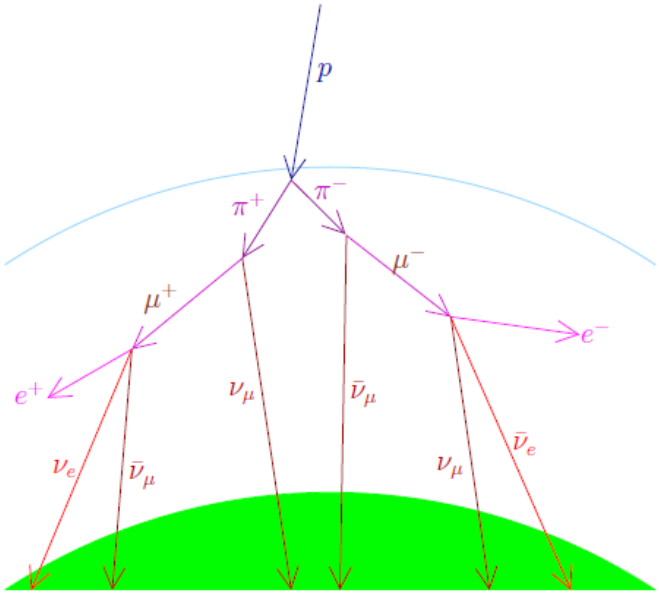

Figure 1.6: The process that produces atmospheric ν: primary cosmic rays interacting with atmosphere produce secondary particles that can decay [5].

flavor in an atmospheric neutrino flux (at low energy):

$$\phi_{\nu_\mu} + \phi_{\overline{\nu}_\mu} = 2\,(\phi_{\nu_e} + \phi_{\overline{\nu}_e}) \tag{1.72}$$

while the amounts of neutrinos and antineutrinos of the same species are roughly the same. From this model there should be a symmetry between the up-going and the down-going direction, due to the fact that cosmic rays in that energy range are isotropically distributed. Atmospheric neutrinos are detected through the scattering on nuclei in underground laboratories in order to be shielded from secondary cosmic rays, in particular muons.

The first experiment that provided a first hint on neutrino oscillation was Kamiokande. It was a water Cherenkov detector made of 3000 tons of water. It was built to search for nucleon decay. Atmospheric neutrino interactions in the detector were considered as background, so its rate was calculated very precisely. The observed muon neutrino interactions were instead less than expected, the so-called *atmospheric neutrino anomaly* [21].

This anomaly was solved by Super-Kamiokande [22], the improvement of Kamiokande experiment, already described in the section before. It was able to distinguish the direction of neutrinos and to measure the up-down asymmetry. Different classes of events can be identified:

- **Contained events:** neutrino interacts with matter inside the detector and also the track of all particles produced in the reactions are contained. For the experiment that has a inner fiducial volume (as Super-Kamiokande) surrounded by an outer detection volume, two subclass of event can be defined:
  - Partially Contained (PC) events: all particles produced and their trajectories are contained in the inner volume,

  - Fully Contained (FC) events: neutrino interact in the inner volume but some products are stopped in the outer part of the detector,

- **Stopping Muons:** tracks of muons that are stopped in the detector. They are generated by neutrino ineracting with rocks outside the detector,

- **Through-going Muons:** tracks of muons that enter in the detector and exit without stopping. They can be also produced by neutrino interacting with rocks,

Super-Kamiokande [23], using Cherenkov light produced in water, was able to distinguish between ν_μ and ν_e CC events:

$$\nu_l + N \to \ell^- + X \qquad\qquad \bar{\nu}_l + N \to \ell^+ + X$$

The charge of the lepton could not be determined, due to the absence of a magnetic field, so no discrimination was possible between charged particles and antiparticles. Electrons and muons have a different behavior when propagating in water: electrons induce electromagnetic showers, while muons are MIPs (Minimum Ionazing Particle), which generate track-like events. Cherenkov light rings produced by electrons exhibit a highly smeared pattern, whereas those produced by muons are more regular and sharply defined, as displayed in Fig. (1.7). The results shown a lack of muon neutrino events with respect to the expected ones, in particular in the up-going direction [22]. This lack of muon neutrinos is the same as the one predicted by the oscillation model, as shown in Fig (1.8). In the same figure it is also possible to see that oscillations, in this particular range of energy and at these distances, don't affect the electric neutrino: predictions with and without oscillation assumption are compatible, and fit with data. So, as in the solar sector, only two neutrino species are mainly involved in the oscillation, here ν_μ and ν_τ.

1.5.3 Reactor neutrinos

Fission reactors are an intense source of electron antineutrinos. A reactor produces a great number of neutrinos from *β-decay* but these are distributed isotropically in space, so the flux is strongly reduced at increasing distances. Reactor neutrino experiments are in disappearance mode due to the small energy of the neutrino involved: muon and tau antineutrinos produced in the oscillation don't have enough energy to produce their weak doublet partner in a charged current interaction. The neutral current interaction instead is too weak to be distinguished from the background. The reaction exploited for the detection of reactor neutrinos is the *inverse β-decay*:

$$\bar{\nu}_e + p \to n + e^+$$

that has an energy threshold for neutrino:

$$E_\nu^{th} = \frac{(m_n + m_e)^2 - m_p^2}{2m_p} \simeq 1.806\,\text{MeV} \tag{1.73}$$

The first experiment to utilize this reaction for neutrino detection was conducted by Reines and Cowan in 1956: the experiment that detected for the first time the neutrino, proving its existence [24]. Experimental apparatus was composed of three layers of

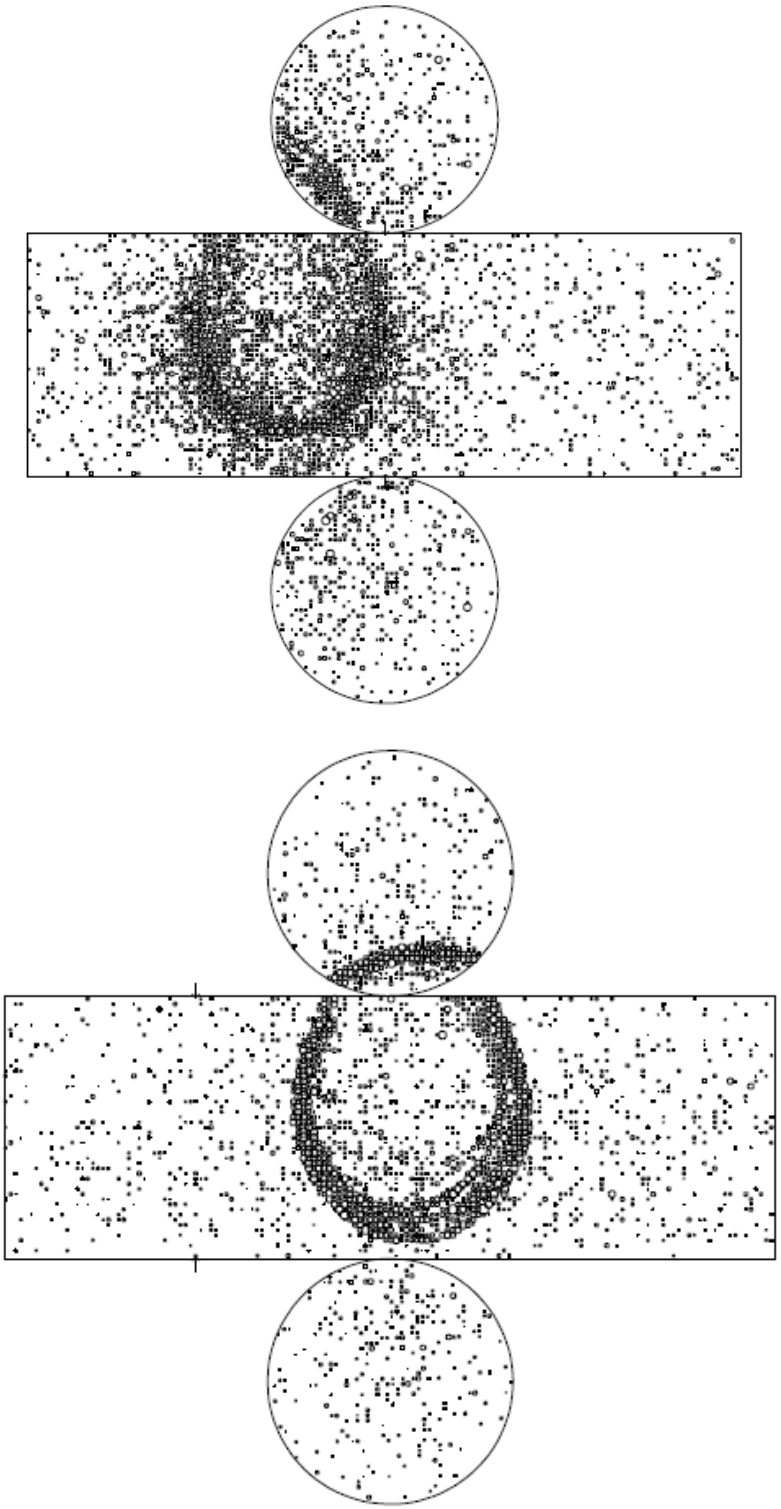

Figure 1.7: Super-Kamiokande event topology, an electron event (top) and a muon (bottom) one [22]. It is possible to see that the ring from to the electron event is smeared respect the one from the muon event that is more defined.

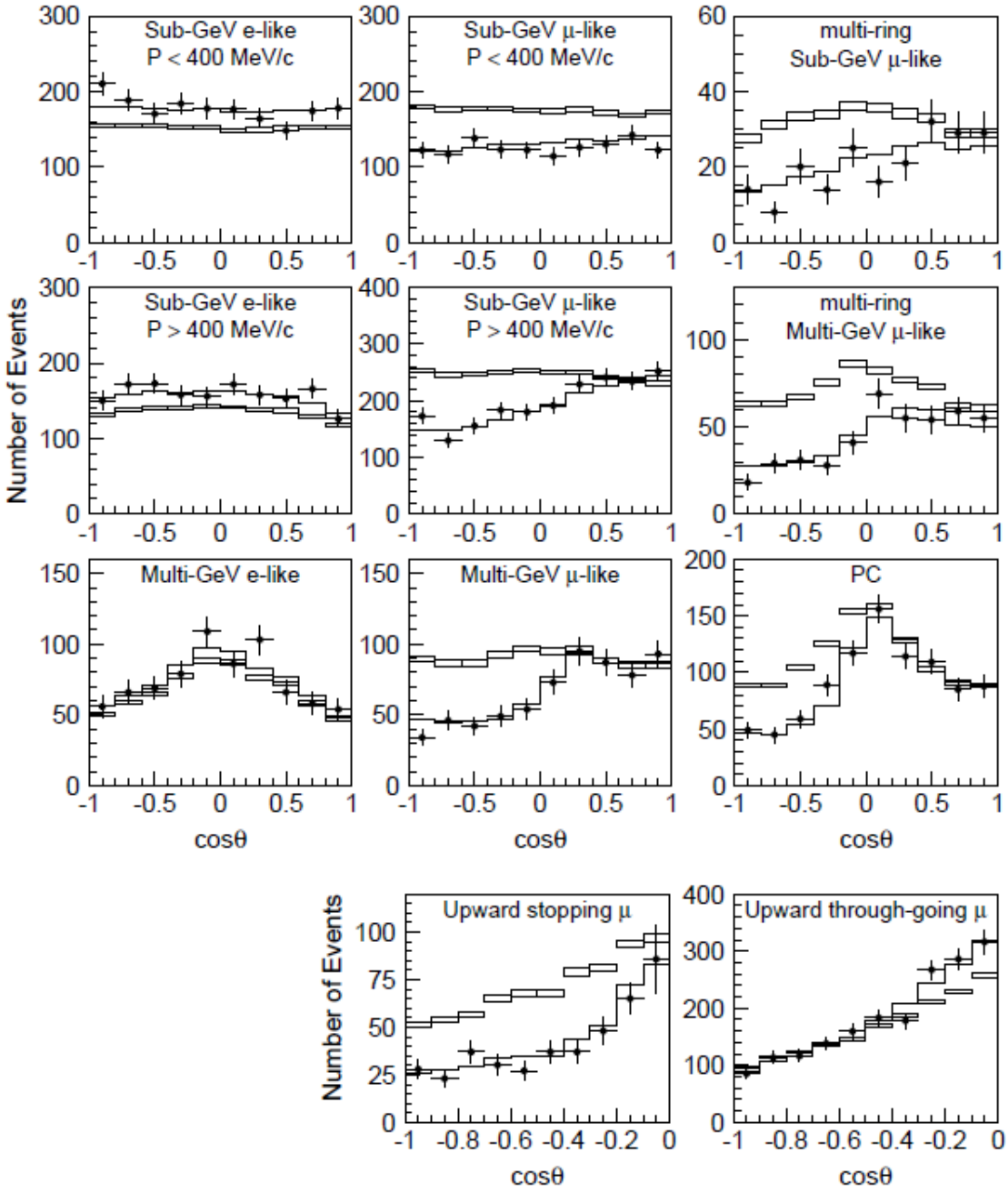

Figure 1.8: Super-Kamiokande experimental results [22] for the atmospheric neutrino sector of different topology of events, in particular the observed events as function of the zenith angle. The box histograms are the Monte Carlo predictions in case of non-oscillation while the lines are the best fit expectations for $\nu_\mu \to \nu_\tau$ oscillation. Data are the points and fit better with the hypothesis of oscillation of only muon neutrino. It is possible to see also that the oscillation in atmospheric sector does not involve electron neutrinos.

scintillator interspersed by two layers of water. Once the reaction took place in water, scintillation light was detected by scintillator. Signal associated to a neutrino event was the coincidence of a prompt and a delayed signals. The prompt signal comes from the annihilation of positron with an electron in water while the delay signal is the result of the nuclear capture of the neutron. This experiment didn't see any evidence of reactor neutrino oscillations.

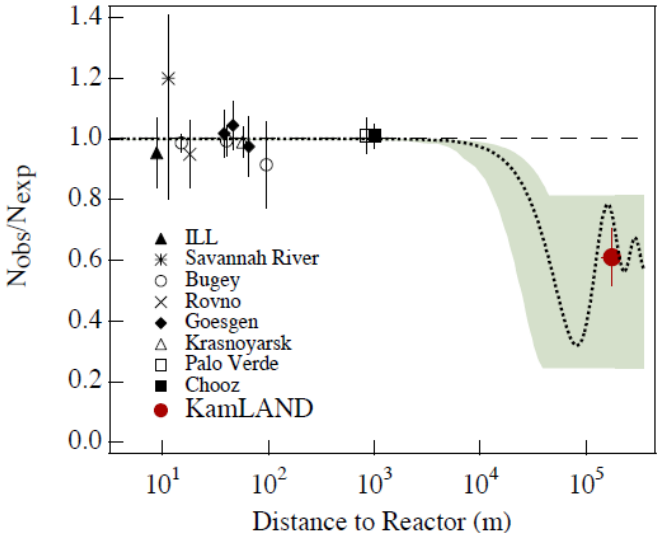

Figure 1.9: Ratio of observed events in function of distance for reactor neutrinos. Clearly, oscillation is visible only after 10^4 m [25].

Due to reactor neutrino energy, experiments that can observe oscillations are the VLBL ones, with a baseline of $\sim 10^5$ m, as can be seen in Fig. (1.9). These have the proper L/E ratio to investigate the solar parameters. The most important experiment in this field was KamLAND. It was a ultra-pure liquid scintillator inside a transparent nylon based balloon with a diameter of about 13 m. The balloon is surrounded by 1879 PMTs. Electron anti-neutrino is detected via *inverse β-decay* reaction, with a threshold for neutrino of 1.8 MeV [26]. It was placed in Japan, in the same site previously occupied by Kamiokande: the Kamioka mine. Electron antineutrinos were produced by 53 reactors placed in Japan and South Korea, with a baseline between 140 km and 250 km. KamLAND observed a disappearance of electron antineutrinos that deviates by about 5σ from the no-oscillation hypothesis. Best fit based on KamLAND data for the oscillation parameters are shown in Fig (1.10).

1.5.4 Accelerator neutrinos

Neutrinos can be also produced in accelerator facilities from a proton beam. In particular, a proton beam is accelerated and impinges on a target to produce mesons, mainly pions and kaons. Then they decay in charged leptons and neutrinos inside the decay pipe; finally the charged lepton are absorbed by a proper material obtaining a neutrino beam. It is composed mainly by ν_μ and $\overline{\nu}_\mu$, but also ν_e and $\overline{\nu}_e$ components are present as background.

An experiment exploiting this technique was K2K [27]. It used neutrinos produced at

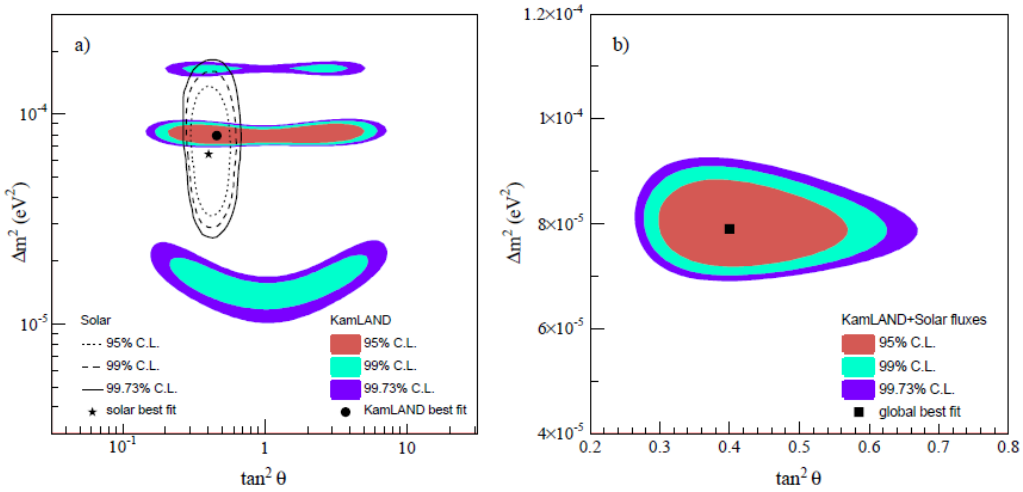

Figure 1.10: Allowed region (left) of Δm^2_{12} and $\tan^2\theta_{12}$ parameters obtained from KamLAND best fit (colored region) and solar neutrino experiments (lines). Also combination of KamLAND and solar neutrino data (right) are provided [26].

KEK proton synchrotron and they were detected at Super-Kamiokande. Neutrino energy is $E \simeq 1.3$ GeV while the distance between the source and the detection point was about 650 km. This experiment had the main goal to check the atmospheric parameters. It observed less muon neutrino events respect to no-oscillation predictions with a discrepancy of 3σ, confirming the oscillation hypothesis. Results are reported in Fig. (1.11). Using accelerator neutrinos it is also possible to put the detector off-axis in order to have a monochromatic and purer beam with the disadvantage to have less statistics. This experiments could observe the channel $\nu_\mu \to \nu_e$ oscillations with the atmospheric parameters opening up the possibility to measure the U_{e3} element of PMNS matrix. This would be the first observation of CP violation in neutrino oscillations and would make possible to determine the hierarchy between the three mass eigenstates.

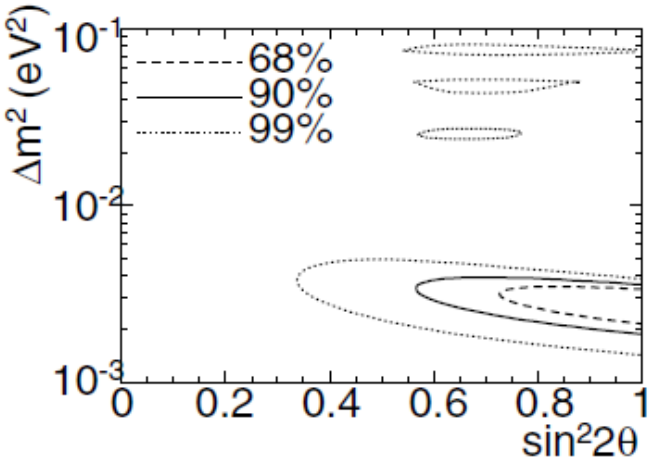

Figure 1.11: Allowed region in the $\Delta m^2 - \sin^2 2\theta$ plane for the disappearance of ν_μ from K2K experiment [27].

1.6 Open questions

The current best values of the oscillation parameters from previous experiments are reported in Fig. (1.12).

NuFIT 5.3 (2024)

		Normal Ordering (best fit)		Inverted Ordering ($\Delta\chi^2 = 2.3$)	
		bfp $\pm 1\sigma$	3σ range	bfp $\pm 1\sigma$	3σ range
without SK atmospheric data	$\sin^2\theta_{12}$	$0.307^{+0.012}_{-0.011}$	$0.275 \to 0.344$	$0.307^{+0.012}_{-0.011}$	$0.275 \to 0.344$
	$\theta_{12}/^\circ$	$33.66^{+0.73}_{-0.70}$	$31.60 \to 35.94$	$33.67^{+0.73}_{-0.71}$	$31.61 \to 35.94$
	$\sin^2\theta_{23}$	$0.572^{+0.018}_{-0.023}$	$0.407 \to 0.620$	$0.578^{+0.016}_{-0.021}$	$0.412 \to 0.623$
	$\theta_{23}/^\circ$	$49.1^{+1.0}_{-1.3}$	$39.6 \to 51.9$	$49.5^{+0.9}_{-1.2}$	$39.9 \to 52.1$
	$\sin^2\theta_{13}$	$0.02203^{+0.00056}_{-0.00058}$	$0.02029 \to 0.02391$	$0.02219^{+0.00059}_{-0.00057}$	$0.02047 \to 0.02396$
	$\theta_{13}/^\circ$	$8.54^{+0.11}_{-0.11}$	$8.19 \to 8.89$	$8.57^{+0.11}_{-0.11}$	$8.23 \to 8.90$
	$\delta_{CP}/^\circ$	197^{+41}_{-25}	$108 \to 404$	286^{+27}_{-32}	$192 \to 360$
	$\frac{\Delta m^2_{21}}{10^{-5}\ \mathrm{eV}^2}$	$7.41^{+0.21}_{-0.20}$	$6.81 \to 8.03$	$7.41^{+0.21}_{-0.20}$	$6.81 \to 8.03$
	$\frac{\Delta m^2_{3\ell}}{10^{-3}\ \mathrm{eV}^2}$	$+2.511^{+0.027}_{-0.027}$	$+2.428 \to +2.597$	$-2.498^{+0.032}_{-0.024}$	$-2.581 \to -2.409$
		Normal Ordering (best fit)		Inverted Ordering ($\Delta\chi^2 = 9.1$)	
		bfp $\pm 1\sigma$	3σ range	bfp $\pm 1\sigma$	3σ range
with SK atmospheric data	$\sin^2\theta_{12}$	$0.307^{+0.012}_{-0.011}$	$0.275 \to 0.344$	$0.307^{+0.012}_{-0.011}$	$0.275 \to 0.344$
	$\theta_{12}/^\circ$	$33.67^{+0.73}_{-0.71}$	$31.61 \to 35.94$	$33.67^{+0.73}_{-0.71}$	$31.61 \to 35.94$
	$\sin^2\theta_{23}$	$0.454^{+0.019}_{-0.016}$	$0.411 \to 0.606$	$0.568^{+0.016}_{-0.021}$	$0.412 \to 0.611$
	$\theta_{23}/^\circ$	$42.3^{+1.1}_{-0.9}$	$39.9 \to 51.1$	$48.9^{+0.9}_{-1.2}$	$39.9 \to 51.4$
	$\sin^2\theta_{13}$	$0.02224^{+0.00056}_{-0.00057}$	$0.02047 \to 0.02397$	$0.02222^{+0.00069}_{-0.00057}$	$0.02049 \to 0.02420$
	$\theta_{13}/^\circ$	$8.58^{+0.11}_{-0.11}$	$8.23 \to 8.91$	$8.57^{+0.13}_{-0.11}$	$8.23 \to 8.95$
	$\delta_{CP}/^\circ$	232^{+39}_{-25}	$139 \to 350$	273^{+24}_{-26}	$195 \to 342$
	$\frac{\Delta m^2_{21}}{10^{-5}\ \mathrm{eV}^2}$	$7.41^{+0.21}_{-0.20}$	$6.81 \to 8.03$	$7.41^{+0.21}_{-0.20}$	$6.81 \to 8.03$
	$\frac{\Delta m^2_{3\ell}}{10^{-3}\ \mathrm{eV}^2}$	$+2.505^{+0.024}_{-0.026}$	$+2.426 \to +2.586$	$-2.487^{+0.027}_{-0.024}$	$-2.566 \to -2.407$

Figure 1.12: Oscillation parameters from the last global fit results [28].

Neutrino physics is far from a complete understanding and many questions remain open. Different experiments are under construction to answer them. The most important questions are:

- **mass ordering:** it is not possible today to establish the ordering between neutrino mass eigenstates, as exposed in section (1.3.1). There are two main approaches to solve this problem:
  - oscillation interference in medium baseline experiments (JUNO [29]);
  - matter enhancement of ν or $\overline{\nu}$ in long baseline experiments (DUNE, HK [13], NOνA [14]);
- CP **violation:** a measurement of the CP phase is still not available;

- **absolute value of neutrino masses:** a measurement of the absolute neutrino mass can be done by looking at the endpoint of the *β-decay* spectrum (KATRIN [10]);
- **Dirac or Majorana particles:** neutrino is the only particle in the SM that can be a Majorana one. To establish it, the only way is to look at the $0\nu\beta\beta$ process (CUORE [7]);
- **sterile neutrinos:** sterile neutrinos can be added to the model to go beyond the $3\nu-$ *paradigm*. There are some anomalies that could suggest their existence (GALLEX [17]).

Chapter 2

DUNE

The Deep Underground Neutrino Experiment (DUNE) will be a next-generation Long-Baseline (LBL) neutrino experiment primarily designed to observe neutrino oscillations [30]. It is composed of three main parts, as shown in Fig. (2.1):

- a new high-intensity neutrino source generated from a megawatt-class proton accelerator at Fermilab;
- a composite Near Detector (ND) located at neutrino source;
- a massive Far Detector (FD) located 1.5 km underground at the Sanford Underground Research Facility (SURF) at a distance of 1300 km from the Near Detector.

This experiment has several goals, the most important of which are to measure the δ_{CP} oscillation parameter and to determine the hierarchy of the neutrino mass states.

In this Chapter, the DUNE beam, the Near and Far detectors, and the scientific program are described.

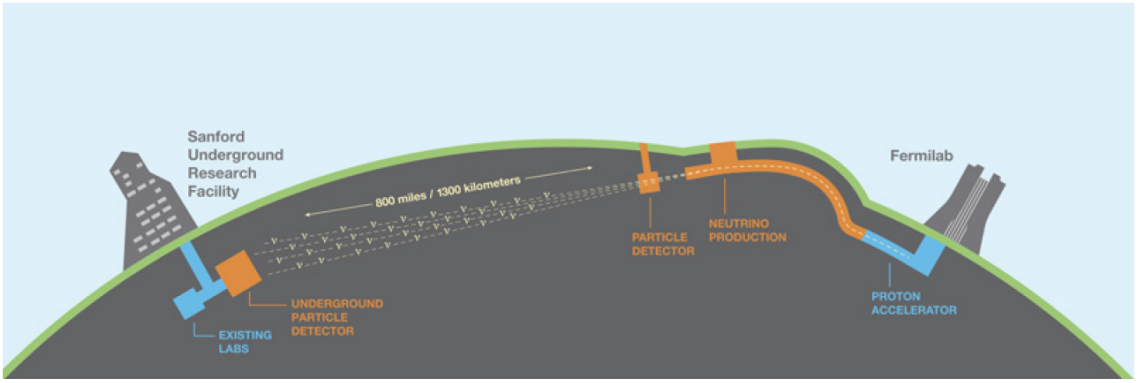

Figure 2.1: Deep Underground Neutrino Experiment cartoons illustration [30].

2.1 Neutrino beam

The neutrino beam is provided by the Long Baseline Neutrino Facility (LBNF) beamline. The primary beam of protons is produced in an energy range of $60 - 120$ GeV at Fermilab

Main Injector (MI) [30]. Once produced, the beam is deviated by the Primary Beam Enclosure in the direction of the Far Detector. Then the protons hit a target producing charged mesons, mainly pions and kaons. Mesons decay in a 194 m long decay pipe, producing $\mu^- + \bar{\nu}_\mu$ or $\mu^+ + \nu_\mu$ depending on the sign of the meson. The sign of the mesons, and consequently the mode of the muon neutrino beam, is selected using a horn in the decay pipe; in particular two different configuration are allowed: Forward Horn Current (FHC) and Reverse Horn Current (RHC). The first configuration produces a ν_μ dominated beam, while the second option a $\overline{\nu}_\mu$ dominated one. At the end of the decay pipe, an absorber hall is placed in order to stop all particles different from neutrinos leaving a neutrino only beam.

In this way, a enough pure ν_μ (or $\bar{\nu}_\mu$) beam is produced, about 90%. The impurities are given by a fraction of muon neutrinos of the wrong sign and a fraction of ν_e and $\bar{\nu}_e$. In fact, muons (antimuons) can decay in electrons (positrons) and $\bar{\nu}_e$ (ν_e), producing part of this impurity in the beam. The main part of the remaining impurity is given by kaon decays produced by protons hitting onto the target. In fact, kaons have different decay channels, some of which have electron or muon neutrinos (antineutrinos) in the decay products [31]. Neutrinos in the beam have an energy in the range $0.5 - 5$ GeV. A representation of neutrino beam facility at Near site is shown in Fig. (2.2).

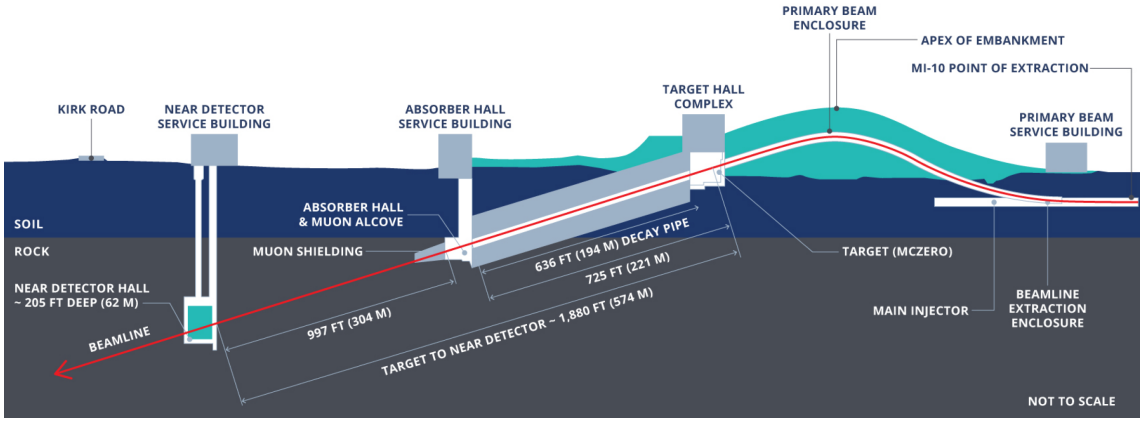

Figure 2.2: DUNE neutrino beamline and near detector site at Fermilab [32].

The facility is designed for initial operation at proton beam power of 1.2 MW with the capability to go at 2.4 MW [33]. The beamline is designed for twenty years of operation. It will operate at 1.2 MW for the first five years, switching to 2.4 MW for the remaining 15 years. The goal of the facility is to accumulate protons of an energy of 120 GeV at the target using a beam power of 1.2 MW [33]. This corresponds to 1.1×10^{11} Proton On Target (POT) per year. The beam is delivered in spills. Each spill lasts 10^{-5} s and corresponds to 7.5×10^{15} POT. Time interval between two consecutive spills is 1.2 s, at a beam power of 1.2 MW. The parameters describing the proton beam are listed in Fig. (2.3). POT per year reported in the figure refers to the solar year, not to the operative time of the accelerator. In fact, during the year the accelerator will be shut down for a specific period. The accelerator operates for 200 days per year.

Parameter	Value	
Energy	60 GeV	120 GeV
Protons per cycle	7.5×10^{13}	7.5×10^{13}
Spill duration	1.0×10^{-5} sec	1.0×10^{-5} sec
Protons on target per year	1.9×10^{21}	1.1×10^{21}
Beam/batch (84 bunches)	12.5×10^{12} nominal; (8×10^{11} commissioning)	
Cycle time	0.7 sec	1.2 sec
Beam Power	1.03 MW	1.2 MW

Figure 2.3: Beam configuration parameters at 1.0 and 1.2 MW [33].

2.2 DUNE detectors

The DUNE experiments has detectors placed in two different sites: the Near and the Far sites. In this way, Far site can observe discrepancy from the unoscillated beam measured at Near site. In other words, the Near Detector is required to validate the observation made at Far site.

2.2.1 Near Detector

The near detector complex will be placed at Fermilab and is composed of three detectors: SAND, NDLAr, NDGAr. The SAND detector is placed fixed on-axis while NDLAr and NDGAr can be moved on-axis and off-axis by a system called DUNE Precision Reaction-Independent Spectrum Measurement (DUNE-PRISM), as it is possible to see from Fig. (2.4).

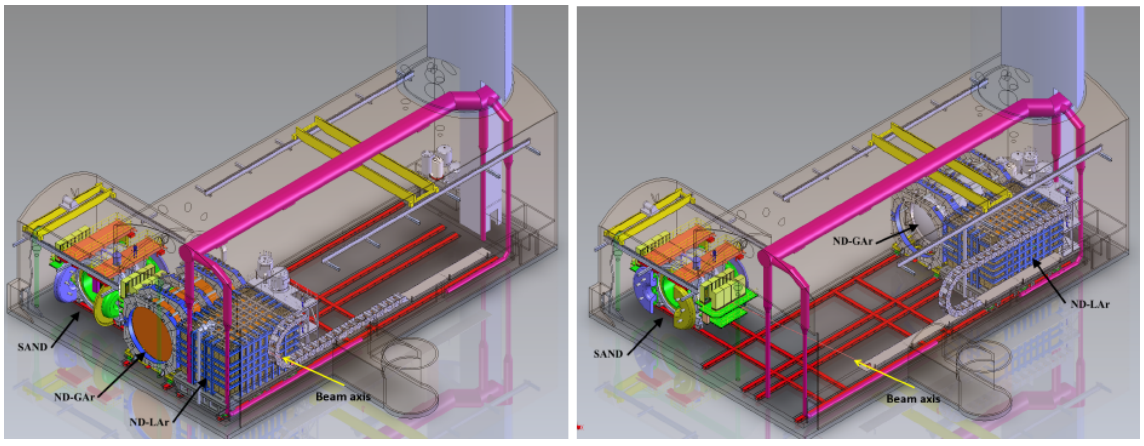

Figure 2.4: Near Detector hall with its components: SAND NDGAr and NDLAr. NDGAr and NDLAr detectors can be putted in on-axis (left) or off-axis (right) configuration [34].

The main goal of the near detector is to measure the unoscillated neutrino energy spectra that must be compared to the ones of the far detector to discover if some flavor is changed. In this way it is also possible to reduce the systematic. The near detector has

also its own scientific program.

SAND

The System for on-Axis Neutrino Detection (SAND) is the part of the near detector permanently on-axis. It will reuse the magnet and the electromagnetic calorimeter of the KLOE experiment. The magnet provide a magnetic field of 0.6 T. In the inner magnetized volume ($\sim$ 43 m^3) a target/tracking system is installed. In particular there are a liquid Argon detector of an active mass of $\sim$ 1 t called GRAIN and a low density tracker based on Straw Tubes (STT). More detailed description of SAND will be discussed in Chapter 3. One of the main goals of SAND is to monitor the beam in order to find some variation in the horn but it has also its own scientific program.

NDLAr

NDLAr is based on the same detection principle of the FD Single-Phase, for neutrino detection. In this way it is possible to reduce the systematics, including those related to nuclear effects on the FD but, due to the higher intensity of the beam, the technology will be a bit different. It is based on the ArgonCube technology [35], consisting of 35 optically separated LArTPC modules, in the same liquid Argon tank with a total fiducial mass of 50 t. Each module has the dimension of 7 m $\times$ 3 m $\times$ 5 m and has two different TPC with a drift path of 0.33 m each and a proper pixel charge readout. A sketch of NDLAr can be seen in Fig. (2.5).

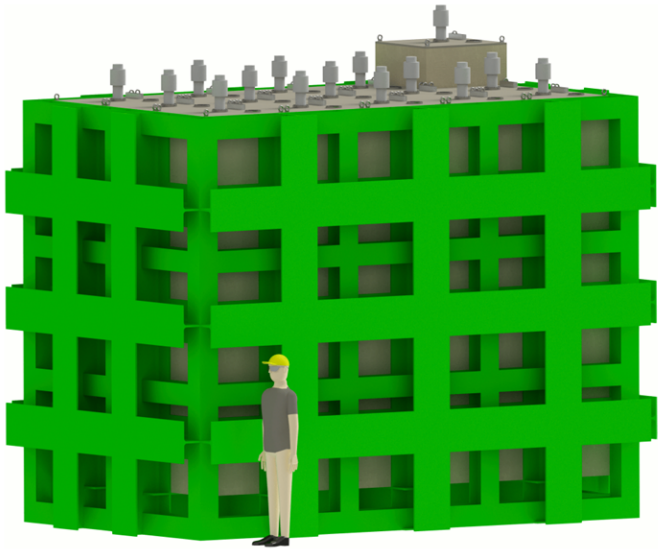

Figure 2.5: Sketch of NDLAr showing its 15 modules [35].

The dimensions of the detector allow a high statistics and also a containment of the hadronic shower events. The pixelized readout provides a 3D imaging that enhance the capability to distinguish the event in case of high multiplicity or pile-up. Each module ha also its Photo-detection system. This detector is sensible to muons below $\sim$ 0.7 GeV/c. Above this threshold, muons are not fully contained in the detector. In the energy region

of interest ($0.5 < E_\nu < 4\,\text{GeV}$), 59 million ν_μ CC events are expected in Forward Horn Current while in Revers Horn Current 20 million of $\bar{\nu}_\mu$ CC events are expected per year.

NDGAr

It is complementary to the NDLAr and consists of a gaseous Argon TPC surrounded by an electromagnetic calorimeter, all in a magnetic field of 0.5 T. The gas is a argon-CH4 mixture at 10 atmosphere with a fiducial mass of 1 t. The main goal of NDGAr is to act as a muon spectrometer of NDLAr: it must track, identify the charge sign and analyze the muons that exit from NDLAr in order to measure the energy spectrum of ν_μ and $\overline{\nu}_\mu$ charged current interactions that occurred in NDLAr [34].

At the center of the TPC an electrode is placed in order to provide the electric filed to drift the ionizing charges produces. A sketch of NDGAr can be seen in Fig. (2.6). The starting time for the event can be taken from the scintillating light, as in the liquid Argon technology. It will extend charged particle momentum measurement in particular at low energy and enhance the particle identification (PID) performance in the pion-proton separation. The expected rate in the on-axis configurations is 1.6×10^6 ν_μ CC events per year. In the first phase of the DUNE experiment, it will be replaced by a iron-scintillator detector acting as muon spectrometer.

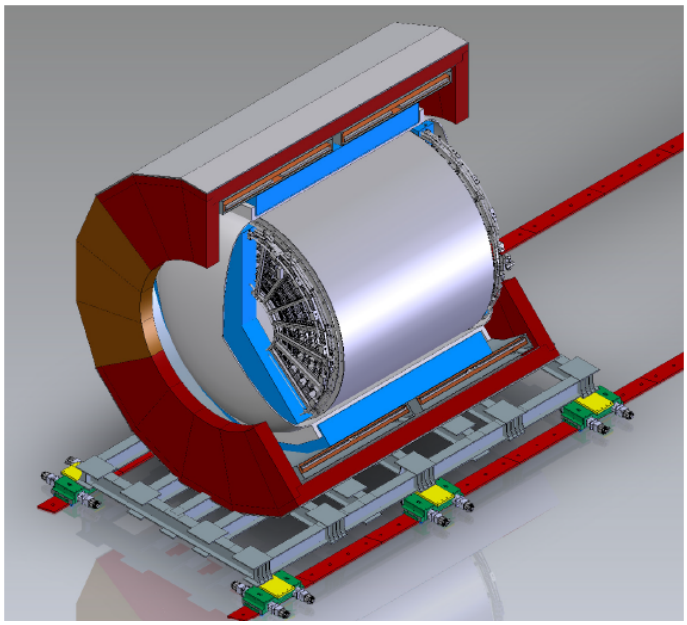

Figure 2.6: Sketch of NDGAr showing HPgTPC, the magnet and the ECAL [34].

2.2.2 Far Detector

DUNE Far Detector (FD) consists of four LArTPC detector modules, each with a total LAr mass of 17 kt, installed about 1.5 km underground at SURF in South Dakota. Each module fits inside a cryostat of dimensions $15.1\,\text{m} \times 14.0\,\text{m} \times 62.0\text{m}$. A sketch of a Far Detector module is represented in Fig. (2.7). The DUNE collaboration has developed

two different module designs: horizontal and vertical drift. Both operate in a single-phase configuration, with argon present exclusively in its liquid state.

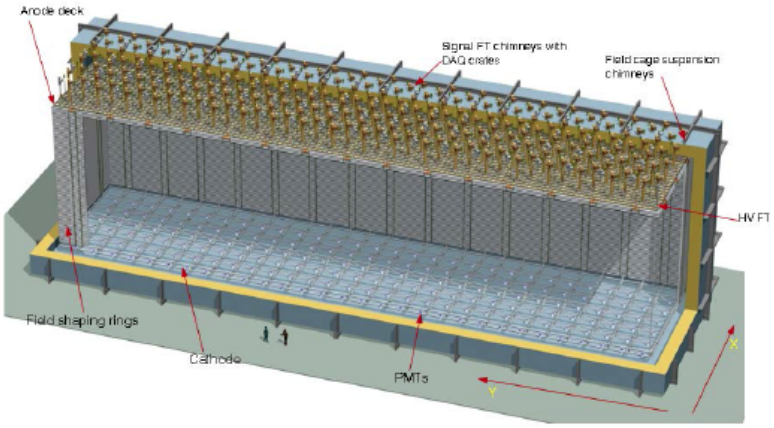

Figure 2.7: Far Detector module [32].

Horizontal Drift

This technology was pioneered by the ICARUS collaboration [36]. Recently, also ProtoDUNE-SP successfully validated it [37]. Charged particles produced by neutrinos in charged current interactions, travel in the TPC ionizing the argon; then the produced electrons drift, reaching the anode, where they are read out. In this configuration there is no amplification, so to have a good signal-noise ratio, the electronic noise must be small. Each module is divided in four drift volumes alternating anode and cathode planes. Each drift volume is 58.2 m long, 3.5 m wide and 12.0 m high. Argon is kept at a temperature of 88 K, the electron drift time is 3 ms, the electric field is set at 500 V/m and a bias voltage of -180 kV is applied. Anode is formed by 25 Anode Plane Assembly (APA). Each APA is 2.3 m wide, 6.3 m high and 12 cm thick and is composed of four layer of wires forming a grid: G, U, V and X. The internal layout is shown in Fig (2.9). There are also field cages (FC) and ground planes (GP). An illustration of a detection module is shown in Fig (2.8).

Argon is also a good scintillator and the light produced is used to provide the absolute timing of the observed event. Liquid Argon generates 40000 photons/MeV. A fourth of the photons emitted is fast signal and is used as starting time (t_0). The light produced has a wavelength of 128 nm, so in the UV range, and must be shifted in the visible one. Once shifted, it is collected by photo-detector, mounted on APAs, the ARAPUCA devices. They trap photons in a reflective box, keeping high the detection efficiency but reducing the dimensions. Also in this case, the photon is then detected and converted in signal by a SiPM.

Vertical Drift

The second module, called Vertical Drift will be a LArTPC of size $13.5\,\mathrm{m} \times 13.0\,\mathrm{m} \times 60\,\mathrm{m}$. It will be divided in two volumes. The cathode will be placed at mid-height, while two anode planes will be present: at the top and at the bottom of the module [39]. A voltage of -300

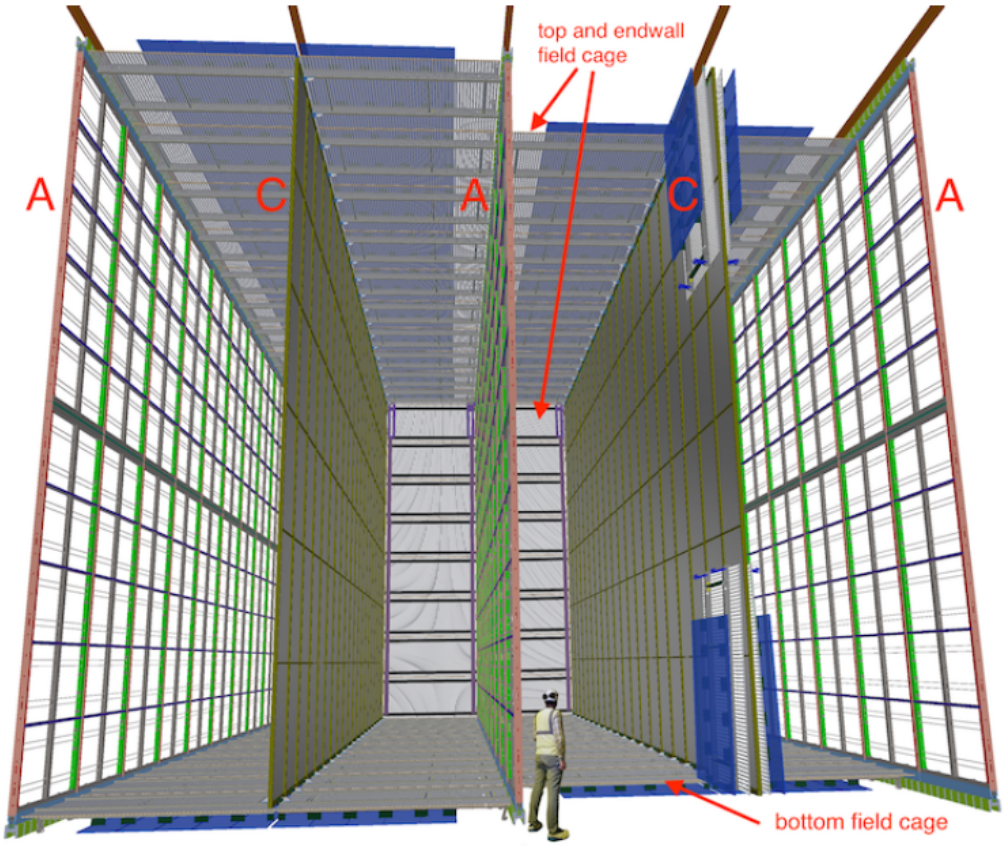

Figure 2.8: A 10 kt Single Phase module of Far Detector, in which is possible to see clearly the alternating of anodes and cathodes [38].

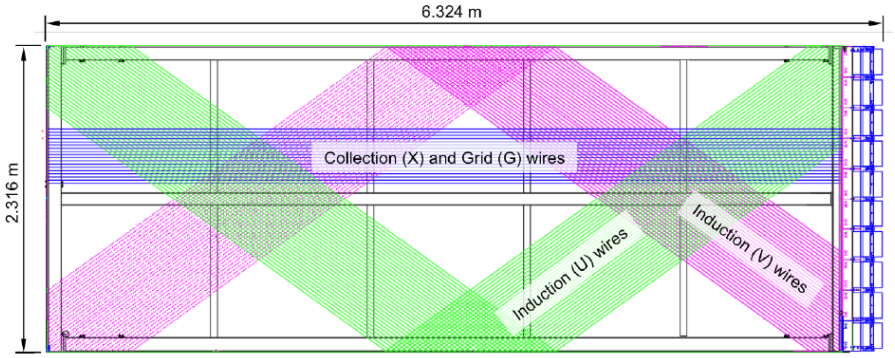

Figure 2.9: Representation of the layout of an APA [38].

kV will be applied to the cathode. The electric field will be set at 500 V/cm. Electrons drift 6.5 m vertically reaching the anodes, where they are read out. Photo-detection system will be composed of $60 \times 60\,\mathrm{cm}^2$ X-Arapucas, a box with reflective internal wall and wavelength shifter [40]. then light collected, will be detected by silicon potomultipliers. Differently from a traditional LArTPC, this photo-detector system will be placed on the cathode because the anodes will be opaque. In fact, they will be perforated printed circuit boards (PCBs). A representation of the vertical drift is shown in Fig. (2.10).

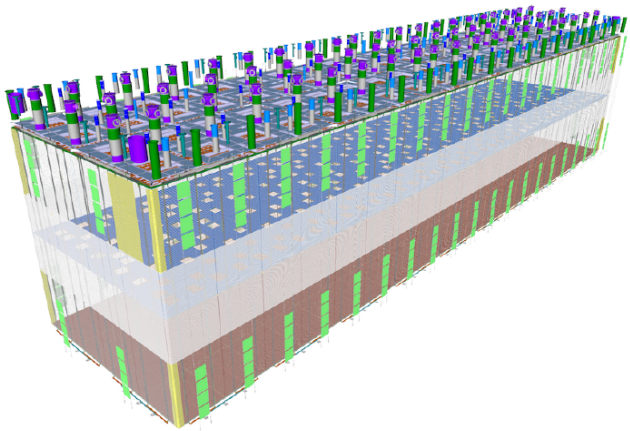

Figure 2.10: A representation of the vertical drift [41].

2.3 DUNE Scientific program

The DUNE experiment will aim to answer some fundamental questions for the understanding of our Universe.

- **What is the origin of the matter-antimatter asymmetry in the Universe?** Our Universe is made of ordinary matter but, after the Big Bang, matter and antimatter were created equally. Studying the CP violation in the lepton sector, DUNE will try to understand a possible cause of this asymmetry.
- **What are the fundamental underlying symmetries of the Universe?** By measuring the lepton parameters (neutrino masses, mixing angles...) and comparing with the ones of quark sector, DUNE could reveal new symmetries.
- **Is there a Grand Unification Theory?** Grand Unification Theories are theories that aim to unify all interactions in the Universe. They also predict some process never observed yet, such as proton decay. Dune will search for proton decay in the range of some GUT models.
- **How do supernovae explode and what new physics will we learn from neutrino burst?** Heavy elements are produced by core collapse of supernovae, DUNE will be able to detect neutrino from the core collapse of supernovae in our galaxy in order to provide information on neutrino properties.

To solve these questions, a scientific program has been developed. The scientific program of the DUNE experiment is divided in *primary science goals* and a *ancillary science goals*. In particular, the primary goals, the one for which the experiment is built, are [42]:

- make precise measurements, using ν_μ and $\overline{\nu}_\mu$ beams, of the oscillation parameters between $\nu_1 - \nu_3$ and $\nu_2 - \nu_3$, including the CP phase δ_{CP}, determine the ordering of the neutrino mass states, and test the 3ν paradigm;
- study neutrino emitted by core-collapse supernova that could explain the evolution of the universe;
- search for proton decay, predicted by most Grand Unification Theories.

Ancillary goals are the ones for which the experiment is not built but can be achieved. They are:

- further measurement of Beyond Standard Measurement interactions,
- atmospheric neutrino oscillation measurement,
- measurements of other astrophysical phenomena.

Near Detector has also its own scientific program, but it will be discussed in Chapter 3.

2.3.1 Sensitivities and Systematics

The energy spectrum of muon neutrino ν_μ measured at Near Detector is used to predict the spectra at Far Detector site (N_{FD}^{exp}) of ν_μ and ν_e. The observed spectrum of ν_μ at Near Detector is the product of: beam flux (Φ), detector efficiency (ϵ) and neutrino interaction cross section (σ).

$$N_{ND}^{data}(\nu_\mu) = \Phi_{ND}(\nu_\mu) \otimes \epsilon_{ND}(\nu_\mu) \otimes \sigma_{ND}(\nu_\mu) \tag{2.1}$$

In order to predict the the spectra at Far Detector site, some corrections must be done:

- **Differences in the beam flux between Near and Far Detectors site Φ_{FD}/Φ_{ND}.** Near Detector is much closer to neutrino beamline respect the Far Detector, so it sees an extended neutrino source. A Monte Carlo is used to simulate the propagation of the beam between the two sites and to correct these differences.
- **Differences in the efficiency between Near and Far Detectors site $\epsilon_{FD}/\epsilon_{ND}$.** These uncertainties arise from different event selection efficiencies and the imperfect modeling of the energy scales between Near and Far Detectors. The possibility to have the same technology for the detectors allow to cancel the uncertainties in the extrapolation of the ν_μ signal while residual ones in the ν_e signal are present.
- **Differences in the cross section between Near and Far Detectors site σ_{FD}/σ_{ND}.** These differences are canceled for the extrapolation of ν_μ expected signal if the target nuclei in Near and Far Detectors are the same. When the ν_μ signal is used to predict the ν_e one, instead, the uncertainties arising from differences in ν_e interaction dominate.

The expected ν_μ flux at Far site is:

$$N_{FD}^{exp}(\nu_\mu) = N_{ND}^{data}(\nu_\mu) \otimes \frac{\Phi_{FD}(\nu_\mu)}{\Phi_{ND}(\nu_\mu)} \otimes P(\nu_\mu \to \nu_\mu) \otimes \frac{\epsilon_{FD}(\nu_\mu)}{\epsilon_{ND}(\nu_\mu)} \otimes \frac{\sigma_{FD}(\nu_\mu)}{\sigma_{ND}(\nu_\mu)} \tag{2.2}$$

The expected ν_e flux at far site is instead:

$$\begin{aligned} ND_{FD}^{exp}(\nu_e) = & N_{ND}^{data}(\nu_\mu) \otimes \frac{\Phi_{FD}(\nu_\mu)}{\Phi_{ND}(\nu_\mu)} \otimes P(\nu_\mu \to \nu_e) \otimes \frac{\epsilon_{FD}(\nu_\mu)}{\epsilon_{ND}(\nu_\mu)} \otimes \frac{\sigma_{FD}(\nu_\mu)}{\sigma_{ND}(\nu_\mu)} \\ & + N_{ND}^{data}(\nu_e) \otimes \frac{\Phi_{FD}(\nu_e)}{\Phi_{ND}(\nu_e)} \otimes P(\nu_\mu \to \nu_e) \otimes \frac{\epsilon_{FD}(\nu_e)}{\epsilon_{ND}(\nu_e)} \otimes \frac{\sigma_{FD}(\nu_e)}{\sigma_{ND}(\nu_e)} \\ & + \text{NC background prediction from } N_{ND}^{data}(\nu_e) \\ & + \nu_\tau \text{ background prediction from } N_{ND}^{data}(\nu_\mu) \end{aligned} \tag{2.3}$$

From similar experiments (i.e. MINOS and T2K), it is possible to estimate the main sources of uncertainties, that are:

- **Beam flux uncertainties:** they are related to the precision with which the absolute normalization and shape of different components of the neutrino beam will be measured by the Near Detector. The ND is being designed to improve performance relative to the current generation of acceleration neutrino experiments.
- ν_μ **energy scale uncertainties:** the muon neutrino spectrum at Near Detector is used to predict the spectrum of the electron one at Far Detector, so the uncertainties on ν_μ are propagated to ν_e
- **Absolute** ν_e **energy scale uncertainty:** in order to obtain the proper mass ordering and CP-violation sensitivity, an accurate measurement of ν_e appearance signal shape is necessary. Detector response influences the determination of electron neutrino energy, that introduces systematic uncertainties in the determination of the ν_e absolute energy scale
- **Simulation uncertainties:** these type of uncertainties are referred to uncertainties in neutrino interaction with the target nucleus in Near and Far Detectors.

The main sources of uncertainties listed above are shown in Fig (**??**) compared to the ones of the other experiments.

2.3.2 CP violation and mass ordering

Some of the main goals of DUNE experiment are to determine the mass ordering between the neutrino mass states and the CP-violation. To do this task, very precise measurements of $\nu_\mu \to \nu_e$ and $\overline{\nu}_\mu \to \overline{\nu}_e$ oscillation probability are needed. In particular the $\nu_\mu \to \nu_e$ oscillation probability in matter is:

$$\begin{aligned} P(\nu_\mu \to \nu_e) = & \sin^2 2\theta_{23} \sin^2 2\theta_{13} \frac{\sin^2(\Delta_{31} - aL)}{(\Delta_{31} - aL)^2} \Delta_{31}^2 \\ & + \sin 2\theta_{23} \sin 2\theta_{13} \sin 2\theta_{12} \frac{\sin(\Delta_{31} - aL)}{(\Delta_{31} - aL)} \Delta_{31} \frac{\sin(aL)}{(aL)} \Delta_{21} \cos(\Delta_{31} + \delta) \\ & + \cos^2\theta_{23} \sin^2 2\theta_{12} \frac{\sin^2(aL)}{(aL)^2} \Delta_{21}^2 \end{aligned} \tag{2.4}$$

with $\Delta_{ij} = \Delta m^2_{ij} L/4E$, $a = G_F N_e/\sqrt{2}$; where G_F is the Fermi constant, N_e the density of electron in Earth, L the distance in Km and E the neutrino energy in GeV. The first term describes the atmospheric probabilities, while the last the solar one. The middle term is instead the mixing between atmospheric and solar contributions. Parameters Δ_{31} and Δ_{23} can be positive or negative, depending on the hierarchy (normal or inverted). Looking at the CP-conjugate process $\overline{\nu}_\mu \to \overline{\nu}_e$, both a and δ change sign. An asymmetry between neutrino and antineutrino process can be introduced:

$$\mathcal{A} = \mathcal{A}_{CP} + \mathcal{A}_{matter} = \frac{P(\nu_\alpha \to \nu_\beta) - P(\overline{\nu}_\alpha \to \overline{\nu}_\beta)}{P(\nu_\alpha \to \nu_\beta) + P(\overline{\nu}_\alpha \to \overline{\nu}_\beta)} \tag{2.5}$$

The origin of matter asymmetry is the presence of electron and the absence of positron in Earth, as exposed in Section (1.3.3). The two asymmetries have different behaviors increasing the distance, in particular:

$$\begin{aligned} \mathcal{A}_{CP} &\propto L/E \\ \mathcal{A}_{matter} &\propto L \times E \end{aligned} \tag{2.6}$$

The result is that in the few-GeV energy range and for a baseline greater than $\sim 1200\,Km$ the degeneracy between CP-violation and matter effects can be resolved, as shown in Fig. (2.11).

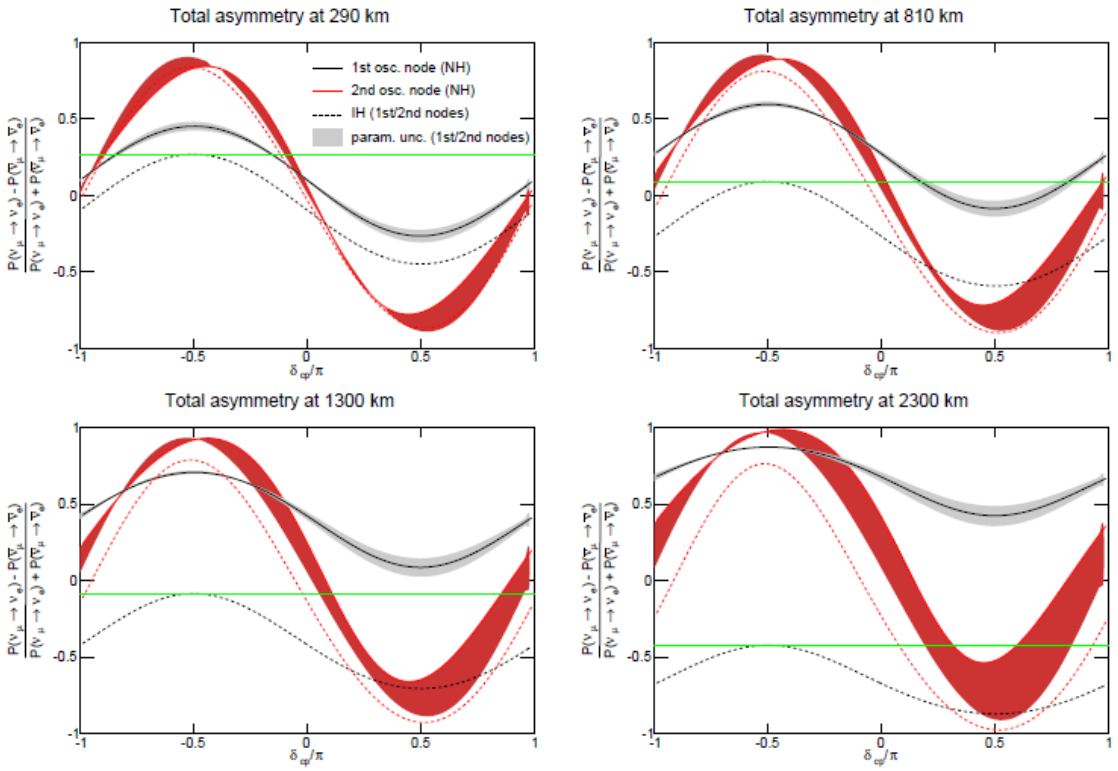

Figure 2.11: Oscillation probability asymmetry versus δ_{CP} for different values of source-detector distance. Black line is total asymmetry at the first node while the red one is at the second node; dotted lines are the same but in inverted hierarchy [3].

2.3.3 Precise measurements on oscillation parameters

DUNE will be able to improve the precision on key parameters of $\nu_\mu \to \nu_e$ and $\nu_\mu \to \nu_\mu$ oscillation; in particular, this experiment is interested in: $\sin^2\theta_{23}$ and the octant of θ_{23}, δ_{CP}, $\sin^2 2\theta_{13}$ and Δm^2_{31}.

The enhancement of the precision on oscillation parameters is crucial in order to improve the sensitivity to physics beyond the three-flavors paradigm [43].

Measuring with high precision the value of $\sin^2\theta_{23}$, DUNE will be able to solve the octant ambiguity. In fact, measurements of these parameters from previous experiments and global fit allow both possibilities: lower octant ($\theta_{23} < 45$) and upper octant ($\theta_{23} > 45$). Also the case of maximal mixing ($\theta_{23} = 45$) is allowed and it is very interesting because it would indicate that ν_μ and ν_τ have the same contribution from ν_3; this would be a hint of a possible unknown symmetry. DUNE will study the $\nu_\mu \to \nu_\mu$ oscillations, sensitive to $\sin^2 2\theta_{23}$ and $\nu_\mu \to \nu_e$ ones, sensitive to $\sin^2\theta_{23}$, in order to probe both maximal mixing and the octant. The $\Delta\chi^2$ for the determination of the octant is:

$$\Delta\chi^2_{octant} = \left|\chi^2_{\theta_{23}^{test}>45} - \chi^2_{\theta_{23}^{test}<45}\right| \tag{2.7}$$

Fig. (2.12) shows DUNE sensitivity to determine the octant as a function of θ_{23} taking the true value from the last global fit [28].

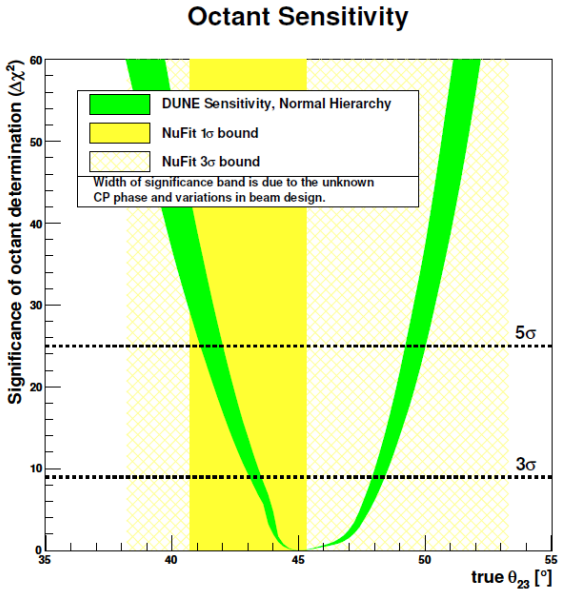

Figure 2.12: Significance with which DUNE will be able to resolve the octant as function of the true value of θ_{23}. Yellow and light yellow bands are the current 1σ and 3σ bands from NuFit while the green one is the range for DUNE due to potential variations in the beam and in the true value of δ_{CP} [43].

DUNE will be able not only to prove if there is CP violation, by looking at the differences in neutrino and antineutrino oscillations, but also to measure its value δ_{CP}.

The constraint on θ_{13} is important for the determination in DUNE of the value of δ_{CP}. Usually this value is measured by reactor neutrino experiments, as Daya Bay, studying

the $\overline{\nu}_e$ disappearance, but also DUNE will measure it through the ν_e and $\overline{\nu}_e$ appearance, proving an independent constraint on the mixing matrix.

DUNE will also improve the sensitivity on the other oscillation parameters, like $\sin^2\theta_{13}$ and Δm^2_{31}

Fig. (2.13) shows DUNE expected resolution on oscillation parameters as function of the exposure, taking the true value of them from the last global fit [28].

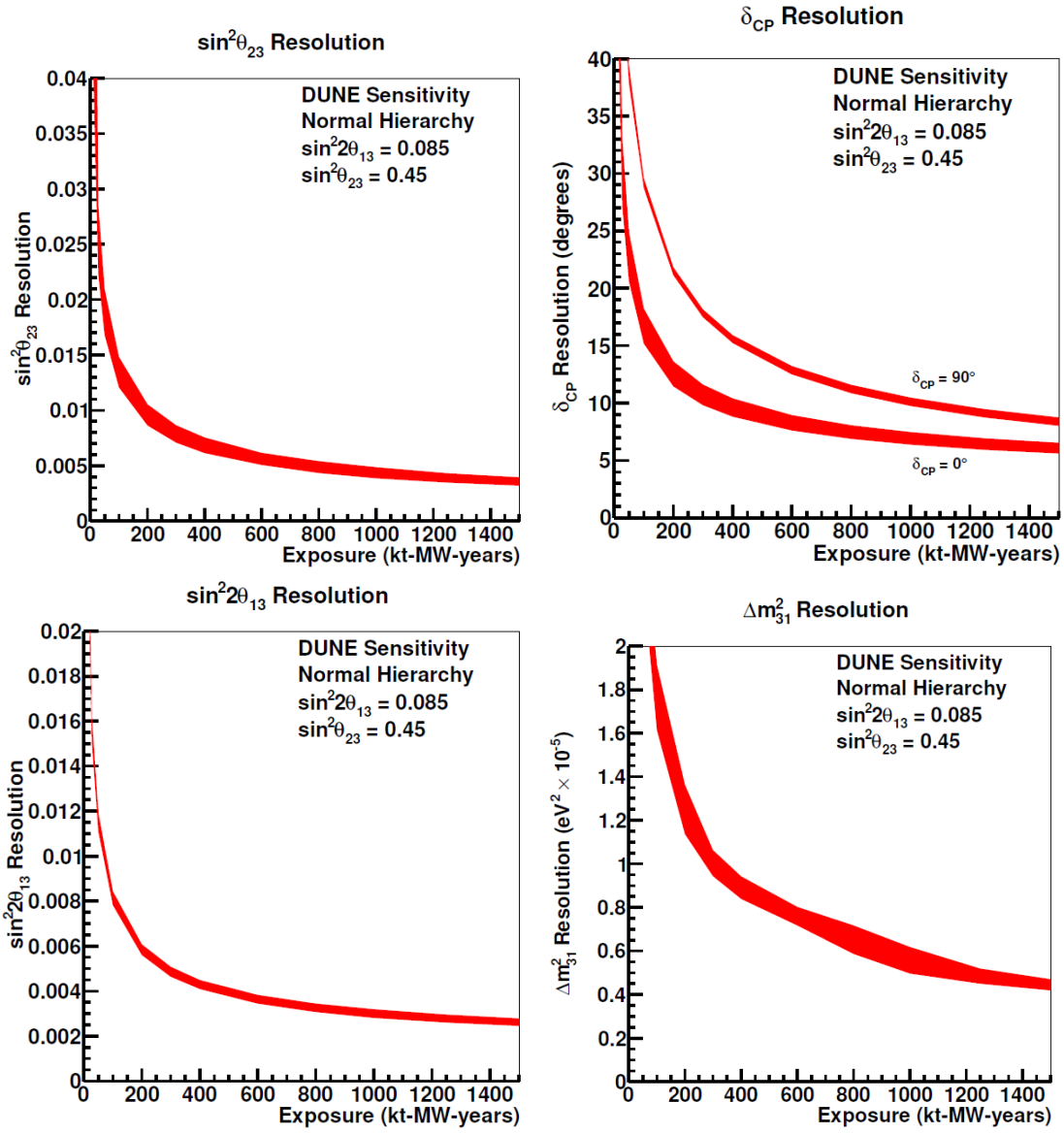

Figure 2.13: Oscillation parameters resolution expected in DUNE as function of exposure assuming Normal Hierarchy and values of the parameters from global fit. In case of δ_{CP} (top right), it is represented both for CP-conserving case ($\delta_{CP} = 0$) and maximal violation one ($\delta_{CP} = 90$) [43].

2.3.4 Barion number violation

One of the open questions in physics is whether protons are stable. Several experiments try to solve this problem, DUNE will contribute to it. No known symmetries require the conservation of barion number, so this decay should be observed. Furthermore, Barion Number Violation (BNV) contributes to explain the matter-antimatter asymmetry of the Universe [3]. On the other hand, the non-observation of this phenomenon can suggest a new symmetry that forbids it [32]. Observation of Barion Number Violation is also important for Grand Unified Theories (GUTs) that unify strong, weak and electromagnetic forces. The unification scale of GUTs is too high to be reached with accelerator experiments, the only way to study them is to test their predictions at low energies, for example proton decay. At now, using current experiments, only lower limits on proton lifetime can be set, because no evidence of proton decay has been detected; this is enough to exclude some GUT models, as shown in Fig. (2.14). Different decay channels for proton are

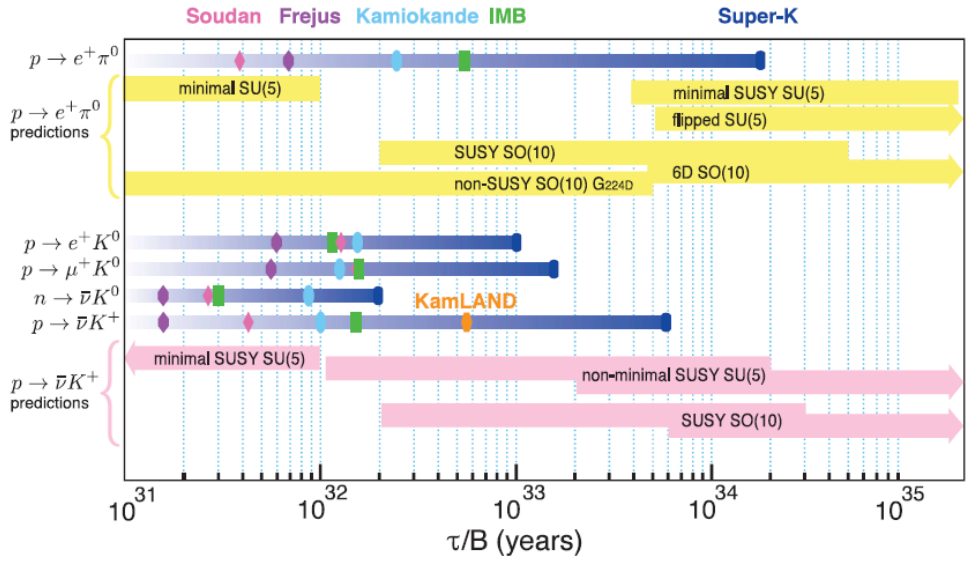

Figure 2.14: Proton decay lifetimes limits set from different experiments compared to the lifetimes regions allowed by some GUTs for different decay channels [32].

possible, according with GUTs, but DUNE will have the capability to detect two of them, which Feynman diagram are displayed in Fig. (2.15):

$$p \to K^+ \overline{\nu}$$
$$p \to e^+ \pi^0$$

In particular, the first decay channel is very interesting for DUNE because the LArTPC technology could identify the kaon track with high efficiency, due to kaons higher ionization density than lower-mass particles. Furthermore, final state of charged kaon decay would be fully reconstructible using this technology. The efficiency for this decay channel is estimated to be 97.5% with a background of one event per Mt · year. In the other decay channel, instead, the total mass of the proton is converted into electromagnetic shower of positron and photon from pion decay, so Cherenkov detectors are favored in this case.

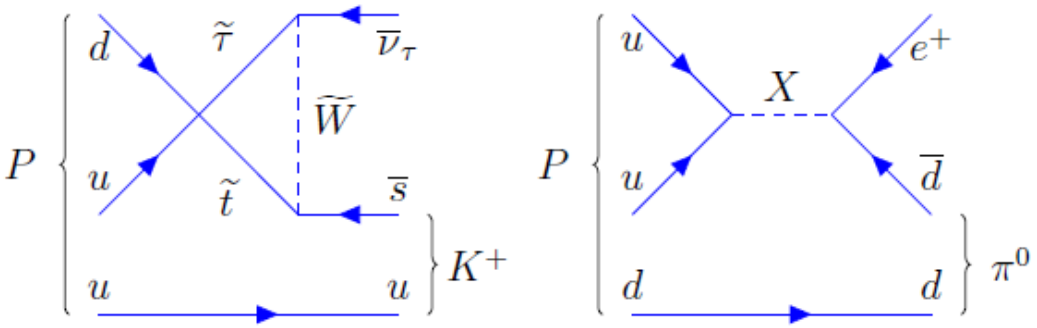

Figure 2.15: Two Feynman diagrams of proton decay that can be observed in DUNE experiment [3].

Although the higher branching fraction, the efficiency of DUNE LArTPC in this case is only 45% with one event per Mt · year.

2.3.5 Core-collapse supernova neutrinos

A core-collapse supernova occurs when a massive star dies. The central region of the star assumes a "onion" structure with iron at the center surrounded by concentric shells of lighter elements. At this stage, the iron core loses energy by the continuously emission of neutrinos and, since iron cannot be further burned, the core contracts and heats up. At the mass of $1.4\,M_\odot$ no stable configuration is possible, electrons are absorbed by protons and the core collapses in free fall. This collapse is then stopped when the nuclear density is reached (after $\sim 10^{-2}$ s) and the core bounces producing a shock wave. The medium created at this stage is so dense that even neutrinos cannot escape. The gravitational energy is stored in degenerate Fermi sea of electrons and electron neutrino, which are in equilibrium with each other. At the next stage, the trapped energy is released together with neutrinos and antineutrinos of all flavors. Over 99% of the gravitational energy of the $1.4\,M_\odot$ core collapse is released in neutrino at this stage [32]. The object that remains is a neutron star or a black hole.

The study of this low-energy neutrinos (tens-of-MeV) is important for the understanding of the evolution of the Universe. Observation from the SN1987A collapse in the Large Megellanic Cloud, outside the Milky Way, provided the qualitative confirmation of the basic picture of core-collapse. At the same time, the poor statistics kept some questions opened.

During its operation life, DUNE will be able to observe neutrino from core-collapse supernovae in the Milky Way, if they occur. DUNE will be sensitive to the ν_e component of the total flux from the supernova, via the absorption interaction:

$$\nu_e + {}^{40}\mathrm{Ar} \rightarrow e^- + {}^{40}\mathrm{K}^* \tag{2.8}$$

so the signal is given by the coincidence of electron with the gamma from the de-excitation of ${}^{40}K^*$. The behavior of the expected number of signal events as function of the distance of the source and for different detector masses is represented in Fig (2.16).

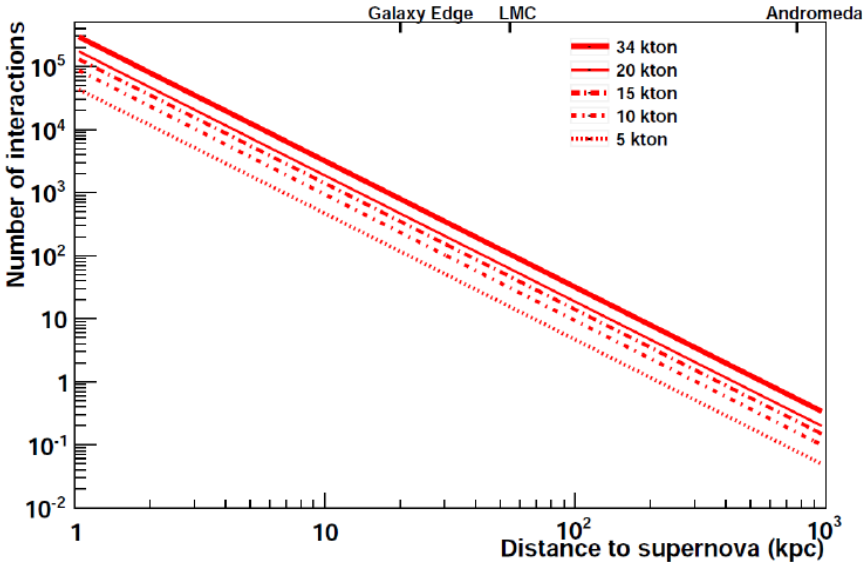

Figure 2.16: Number of supernova neutrino interactions expected in a liquid Argon detector as a function of distance to the source for different quantities of Argon [3].

2.3.6 Atmospheric neutrinos

DUNE will also be able to measure atmospheric neutrinos. These are neutrinos and antineutrinos of all flavors over a vast range of energies and path lengths, including the ones for which matter effects are relevant. In this way, all oscillation parameters could be measured, complementary to the ones made of using the beam. DUNE Far Detector, because of its large mass and the underground location, will be able to do this kind of study [43]. In Fig (2.17) the Mass Hierarchy sensitivity as function of fiducial exposure is shown: it is possible to see that for atmospheric neutrinos measurements, unlike for beam ones, sensitivity to MH is independent of CP-violating phase. This makes possible to resolve the mass ordering problem without ambiguities, using atmospheric neutrinos.

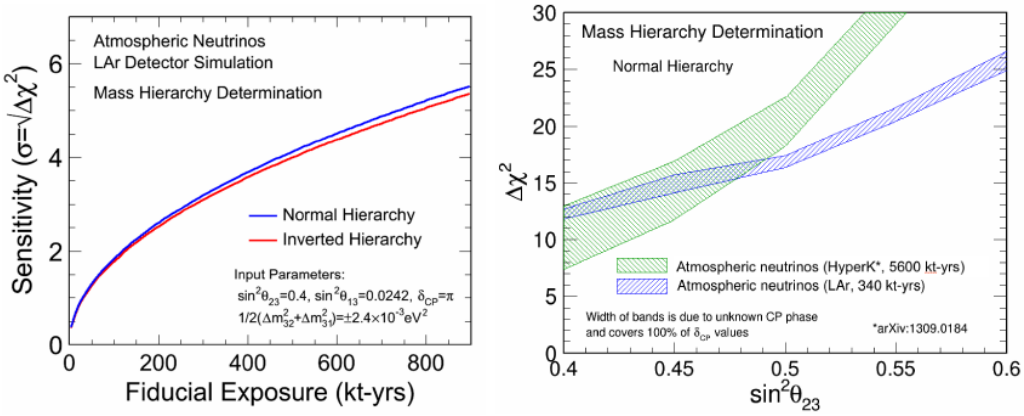

Figure 2.17: Sensitivity on the mass hierarchy, using atmospheric neutrinos, as function of exposure (left) and on $\sin^2\theta_{23}$ (right). In the second plot also values of HK are reported [43].

2.3.7 BSM physics

The combination of high intensity neutrino beam with near detector and massive far detector modules, gives the opportunity to probe Beyond Standard Model physics with unprecedented sensitivity [32].

Search for active-sterile neutrino mixing. Some experimental results are in tension with the three-neutrino-flavor paradigm: data from these experiments may suggest mixing between the known active neutrinos and one or more sterile states. DUNE is sensitive over a wide range of possible sterile neutrino mass, searching for disappearance in charge and neutral current interaction over the long baseline distance from ND and FD, as well as over the short baseline distance of the ND. DUNE will be able to improve significantly on the sensitivity of the existing measurements.

Searches for non-unitarity of the PMNS matrix. A lot of models that explain the neutrino mass pattern, for example the *see-saw mechanism* discussed in Chapter 1, introduce heavy neutrino states, additional to the three light ones of the Standard Model. The presence of these additional states implies a deviation from unitarity of the 3×3 PMNS matrix. For deviations of order of 10^{-2}, this would decrease the expected reach of DUNE to the standard parameters.

Searches for non-standard interactions (NSI). NSI can affect neutrino propagation in Earth, producing a significant change in the collected data, if the new physics parameters are large enough. Exploiting its long baseline and high neutrino beam intensity, DUNE will be sensitive to those probes.

Searches for violation of Lorentz or CPT symmetry. *CPT* symmetry is important because it is the cornerstone of physicist's model-building system; violation of this symmetry will have consequences on the SM of particle physics. DUNE will improve present constraints on Lorentz and *CPT* symmetry by several orders of magnitude, providing tests of these assumption of fundamental physics.

Searches for neutrino trident production. Neutrinos may be charged particles under new gauge symmetries beyond the SM, interacting with other particles via new gauge bosons. DUNE will be able to measure deviations from SM rates, testing the presence of new gauge symmetries, through ND measurements of neutrino-induced di-leptons production (also known as neutrino trident interaction).

Searches for light dark matter (LDM). Existence of dark matter is supported by a lot of cosmological observations. Searches of dark matter candidates, that interact with ordinary matter via a new mediator, are motivated in the case of dark matter mass below the electroweak scale. Exploiting neutral current interactions, Near Detector will be able to detect these particles. DUNE will be able to study by itself these kinds of particles but also to be complementary to other experiments.

Searches for boosted dark matter (BDM). In some cosmological model, two different types of dark matter are expected: light and heavy dark matter. Boosted dark matter is light dark matter produced by the annihilation of the heavy one and, due to the large mass difference between the two, it is relativistic. Through various mechanisms, dark matter particles can be emitted by the Sun to the Earth and detected with DUNE, in particular using the Far Detector.

Chapter 3

SAND

SAND (System for on-Axis Neutrino Detection) is the only component of the DUNE Near Detector to be fixed on axis. It composed of different part, some of them re-used from other experiments. It has different functions, the main are beam monitoring and validate measurements made at Far Detector site. In fact, some important quantities like neutrino flux, are convoluted together and the unfolding is needed in order to disentangle each of them.

In this Chapter, we will introduce SAND detector requirements, its components and its physic program.

3.1 Requirements

The general expression for the number of expected events valid both at Near and Far Detector is:

$$N_X(E_{rec}) = \int_{E_\nu} dE_\nu \, \Phi(E_\nu) P_{osc}(E_\nu) \sigma_X(E_\nu) R_{phys}(E_\nu, E_{vis}) R_{det}(E_{vis}, E_{rec}) \tag{3.1}$$

where Φ is the neutrino flux, σ_X the cross section of the process on a given nucleus, R_{phys} is the physic response introduced by the nuclear smearing and R_{det} is the detector acceptance for the final state particles. The term P_{osc} is the oscillation probability, not present at the Near Detector. Finally, E_ν, E_{vis} and E_{rec} are respectively: the true neutrino energy, the total energies of the visible final-state particle and the reconstructed neutrino energy.

SAND will operate with neutrinos in a wide range of energies ($0.5 < E_\nu < 10\,GeV$), so the processes involved in the interaction between neutrino and nuclei are different: quasi-elastic scattering (QES), resonances (RES) and deep inelastic scattering (DIS).

All the terms in eq. (3.1) are combined and, to unfold them, different detectors using different target nuclei are required. The main goal of the Near Detector is the beam monitoring and the reduction of systematics; moreover it has also its own scientific program. The fundamental requirement is that the combined systematics must be smaller than the correspondent statistical uncertainties.

Argon in the Near Detector (NDLAr, NDGAr, GRAIN) has the advantage of being the same target exploited in the Far Detector and of providing high statistics. This choice has some drawbacks: this target nucleus is not good for flux measurements, since it is a heavy nucleus and introduces a significant nuclear smearing R_{phys}. The solution implemented

in SAND involves using lighter target nuclei (C and H) in the Straw Tube Tracker. This allows us to study nuclear smearing of different targets, constraining models of nuclear effects. Nuclear effects are given by the fact that the target particles of the reaction are inside the nucleus. This adds smearing caused by the effect of strong interaction with different nucleons inside nucleus. In this way, SAND will be able to disentangle the physics response R_{phys}, due to the smearing of the target nucleus, from the detector one R_{det}.

3.2 SAND components

AS said before, SAND is the only one component of the Near Detector that is fixed in on-axis position. It is composed of 4 different parts: the magnet, the electromagnetic calorimeter (ECAL), the inner tracker and GRAIN. The magnet and the ECAL are the same used by KLOE (K^0_L LOng Experiment) collaboration [44]. KLOE detector was designed for the study of the CP violation in the decay of neutral kaons. It started taking data in 2000 at DAϕNE, the Frascati ϕ-factory.

3.2.1 Magnet

The magnet that would be used in SAND is the same of the KLOE experiment. It produces a magnetic field of 0.6 T and a magnetized cylindrical volume 4.3 m long and with a diameter of 4.8 m. It is cooled by Helium: gaseous Helium at 5.2 K and at a pressure of 3 bar is liquefied and put in thermal contact with the coil. The coil operates at a current of 2902 A and the stored energy is 14.32 MJ. The radiation shield is instead cooled by gaseous Helium at 70 K from the cryogenic plant. A schematic of the magnet is given in Fig. (3.1).

3.2.2 Electromagnetic calorimeter

SAND will use the same electromagnetic calorimeter (ECAL) of the KLOE experiment, as done for the magnet. It is a lead/scintillating-fiber sampling calorimeter that offers a good light transmission and timing accuracy. The barrel is composed of 24 modules 4.3 m long, 23 cm thick and trapezoidal cross-section, with bases of 59 cm and 52 cm. There are also the two endcaps, each composed of 32 vertical modules 0.7-3.9 m long and 23 cm thick. Due to the overlap between barrel and endcaps, this calorimeter has a 4π hermeticity and no inactive volume. The total weight of the ECAL is $\sim$ 100 t. Each modules is composed of 200 grooved lead foil 0.5 mm thick alternated by as many cladded scintillating fibers with a diameter of 1 mm. All these components are glue together with a special epoxy. The ratio between lead:fiber:glue is 42:48:10. Thanks to the elevated fraction of scintillated fiber, it is possible to achieve a good energy resolution. The average density is 5 g/cm^3, the radiation length is $\sim$ 1.5 cm and the calorimeter thickness is 15 radiation lengths. The read-out is composed of 4880 phototubes. The read-out subdivides each module in five planes: the first four are 4.4 mm thick, the fifth is 5.2 mm. The read-out segmentation gives an $r-\phi$ or $x-y$ resolution of $\sim$ 1.3 cm ($4.4/\sqrt{12}$ cm). Energy and time resolutions

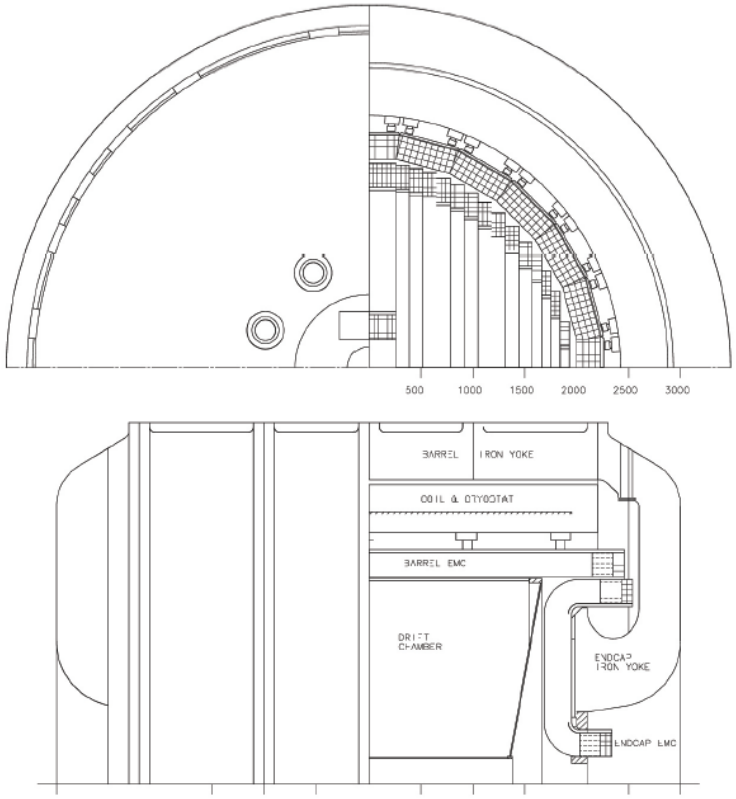

Figure 3.1: Schematic of the KLOE magnet used in SAND [34].

obtained during commissioning and running phase of KLOE experiments are:

$$\begin{aligned} \frac{\sigma_E}{E} &= \frac{5\%}{E(\text{GeV})} \\ \sigma_t &= \frac{54}{E(\text{GeV})}\,\text{ps} \end{aligned} \tag{3.2}$$

Fig. (3.2) offers a picture of the KLOE ECAL used in SAND.

3.2.3 Inner tracker

The Inner Tracker occupies most of the volume inside the ECAL. The technology is based on tungsten straws, with a diameter of 12 μm that are filled with a mixture of Xe and CO_2 (70/30) at the pressure of 1.9 atm. The spatial resolution is $< 200\mu$m, the angular one is ~ 2 mrad, the momentum resolution is $\sim 3\%$. They have a target mass and chemical composition similar to the ones in the electron scattering experiments. This system is divided in STT modules, each composed of: a tunable target layer, a transition radiator and four layers of Straw Tubes. The target layer is made of polypropylene (CH_2) slab with a thickness of 5.3 mm. Also the radiator is made of polypropylene and is composed of 150 foils, each 15 μm thick, with a 120 μm air gap among themselves. Thanks to the exploitation of both the dE/dx and the transition radiation, this radiator is optimized for the e/π separation. These two components constitute about 97% of the module mass. The remain 3% is composed of the straw layers. They are placed in XXYY configuration:

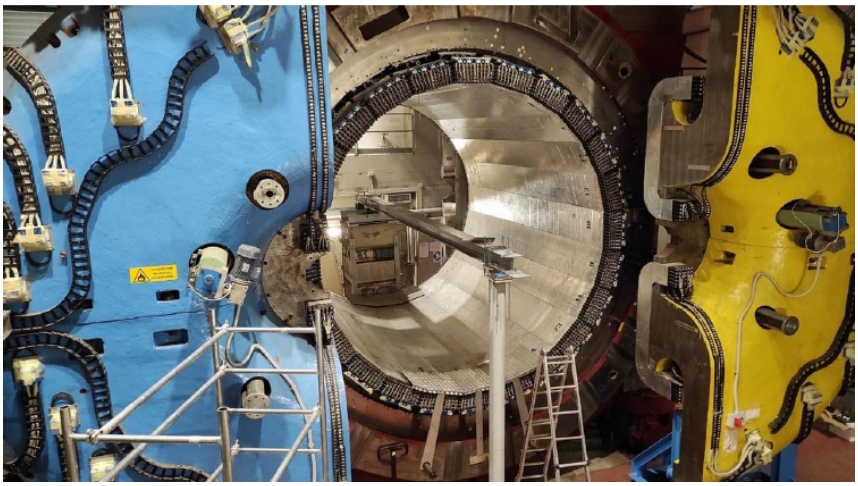

Figure 3.2: KLOE magnet and barrel part of electromagnetic calorimeter [45].

two layer along the x-axis, the other two along the y-axis. A sketch of a STT module is represented in Fig. (3.3).

An important feature of the STT module is the fact that the radiator and the target can be substituted by other target materials like C, Ca, Fe, Pb. The carbon case is very interesting as it allows the study of neutrino interaction with hydrogen through the subtraction technique. This technique prescribes the analysis of a material incorporating the atom of interest and a congruent material without it. Subsequently, a data difference is performed. In the STT, the difference between data with polypropylene and carbon will be computed.

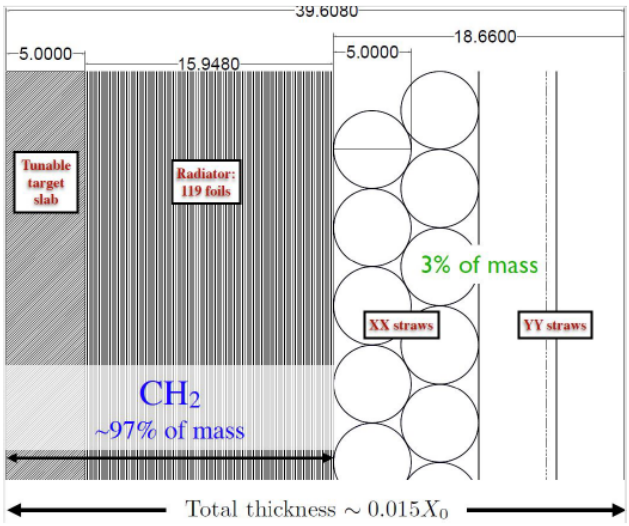

Figure 3.3: Representation of a STT module. There are: target slab, radiator and XXYY straw tubes [34].

3.2.4 GRAIN

GRAIN (GRanular Argon for Interaction of Neutrinos) is a liquid Argon target with the fiducial mass of ~ 1 t. The main goal is to reduce the systematics and study nuclear effects on Argon, in this case fixed in on-axis position. In this way it is possible to study nuclear effects on different target nuclei (Argon, Carbon, Hydrogen) using the same detector. It will be placed inside the magnetized volume, in particular in the upstream part of the barrel. It will be enough thin ($\sim 1\,X_0$) along neutrino beam axis in order to reduce energy loss, showering and multiple scattering of particle produced. In fact they will be analyzed in the downstream elements of the detector and, in order to reconstruct correctly neutrino properties, they must not loose too much energy or being modified in the trajectory. There are two cryostat: an inner vessel and an outer vessel. Inner vessel is made of Aluminum 147 cm height, 150 cm in width and with a maximum depth of 47 cm. The outer one is composed of layer of Aluminum alloy, honeycomb and Carbon fiber and it measures 190 cm in height, 200 cm in width and 83 cm in maximum depth. The inner vessel will be provided of Vacuum UltraViolet cameras to collect the light from liquid argon (78 K) and two different approach for the reconstruction of the event are under studying: one based on lenses and the other based on Coded Aperture Mask. They both need to be coupled with light sensors, in particular silicon photomultipliers (SiPM) matrix are chosen. Two different options are available: S14160 or S13615 Hamamatsu array; the first option is a 8×8 SiPM matrix while the second is 16×16 matrix. In this type of sensors, a wavelength shifter is needed in order to convert the UV light in visible one matching in this way the optimal SiPM photo detection efficiency. A sketch of GRAIN design is shown in Fig. (3.4).

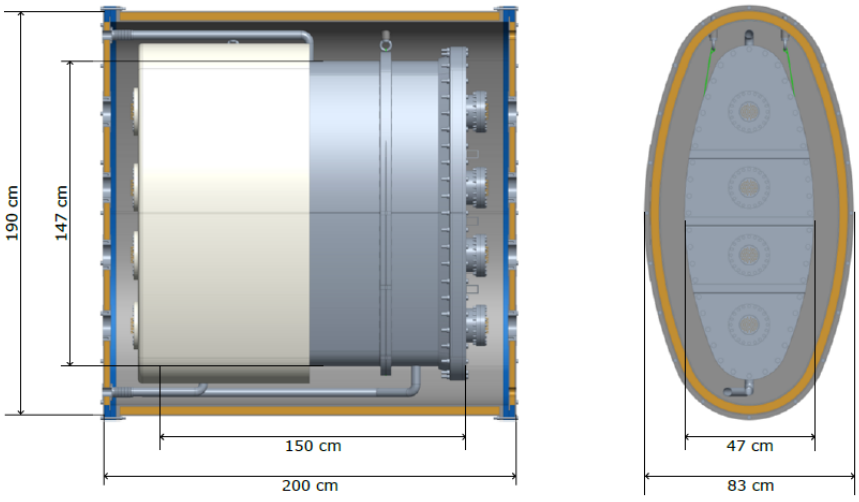

Figure 3.4: Representation of GRAIN [45].

3.3 Physic program

As said before, SAND will have a vast physic program that includes not only measurements to reduce the systematics and validate the ones made at Far Detector site, but also the precise measurements of some relevant physics quantities and the search of new physics.

3.3.1 Reducing systematics

In order to reduce the systematic uncertainties at the proper level needed for the DUNE experiment, all the variables present in eq. (3.1) must be decoupled and measured independently:

- $\Phi(E_\nu)$: due to the usage of low-density materials for the tracker system, SAND will be able to reach high resolution on flux and precise neutrino energy scale measurements. The system will also perform measurements with high accuracy of fluxes of all neutrino and antineutrino flavor components in the beam.

- $R_{phys}(E_{vis}, E_{rec})$: different target nuclei (Ar, C and H) are present in SAND to disentangle the detector response R_{det} from the physical smearing caused by the interaction between neutrino and a certain nucleus. In this detector, in fact, both liquid Argon meniscus and low-density STT modules are presents for this purpose.

- $\sigma_X(E_\nu)$: from the large sample of interactions provided by GRAIN, an estimation of the cross section of Argon can be performed. This can be done if the terms R_{det} and R_{phys} are known precisely.

- $R_{det}(E_\nu, E_{vis})$: a determination of the detector response for the Far Detector is possible if the Near Detector exploits the same technology; LArTPC will provide this quantity. Anyway, SAND will be able to measure the convolution $\sigma_X R_{phys}$ in order to provide another way to find R_{det} in LAr.

SAND will perform precise measurements of all fluxes that are needed in order to unfold all the other terms described above, and therefore to analyze data in the Far Detector. Different processes are considered to obtain the absolute and relative fluxes [46]:

– absolute ν_μ flux from $\nu\, e \to \nu\, e$ elastic scattering,

– absolute and relative $\overline{\nu}_\mu$ fluxes from $\overline{\nu}_\mu\, p \to \mu^+\, n$ on H with $Q^2 \sim 0$, in which the cross section for the process is a constant determined by neutron β-decay,

– relative ν_μ and $\overline{\nu}_\mu$ fluxes in function of E_ν from $\nu_\mu(\overline{\nu}_\mu)\, p \to \mu^\mp\, p\, \pi^\pm$ on H with neutrino energy below 0.5 GeV,

– relative $\overline{\nu}_\mu$ flux in function of E_ν from Quasi-Elastic scattering $\overline{\nu}_\mu\, p \to \mu^+ n$ on Hydrogen with energy below 0.25 GeV,

– ratio of $\overline{\nu}_\mu/\nu_\mu$ vs. E_ν from coherent π^-/π^+, measuring it in the same beam polarity,

– ratio of ν_e/ν_μ and $\overline{\nu}_e/\overline{\nu}_\mu$ in function of E_ν from charged current interactions on CH_2 target; these ratios are independent of the target nuclei,

– ratio of ν_e/ν_μ and $\overline{\nu}_e/\overline{\nu}_\mu$ from charged current interactions on hydrogen,

– determination of parent $\mu/\pi/K$ distributions from charged current on hydrogen and CH_2 at low neutrino energy.

Once the fluxes are measured, the other parameters $R_{phys}R_{det}\sigma_X$ remain still convoluted together. To unfold $\sigma_X\, R_{phys}$ the presence of both argon and light nuclei as target in the same near detector is required in order to have the same value of R_{det} between the different measurements. Of particular interest is the case of hydrogen as target: in this case $R_{phys} = 1$ and the cross section on this target can be determined precisely; the initial unfolding problem depends only on the detector response R_{det} with is $\delta p/p$. Comparing these data with the Ar interactions in STT, it is possible to determine the product $\sigma_X R_{phys}$ on this target. For a separate constraint on R_{phys}, it is possible to determine a set of kinematics variables sensitive to the effect of nuclear smearing and compare the obtained distribution with the observation of CC interaction with H and Ar as targets. In this way it's possible to determine the smearing for a certain Near Detector beam spectrum, that is different from the one in the Far Detector, putting constraint on physics response function and resolving potential degeneracies. Data on the convolution $\sigma_X R_{phys}$ and the constraint on R_{phys} from SAND can be compared with the high statistics sample of interaction in the LArTPC Near Detector in order to unfold the R_{det} term in LAr and validate the prediction for the Far Detector.

3.3.2 Precision measurements and new physics

As said above, SAND will be used not only to validate the measurements of the Far Detector, but it will also have its own scientific program. It will include precision measurements of certain physical quantities and search of new physics.

Precise measurements in the electroweak sector

Using SAND it is possible to measure the weak mixing angle (Weinberg angle) $\sin^2\theta_W$ in neutrino or antineutrino Deep Inelastic Scattering (DIS), the same measurement made by NuTeV collaboration [47]. In this way it is possible to determine the coupling between neutrino and Z^0 boson. The Weinberg angle is measured from the ratio of NC and CC interactions in DIS

$$R = \frac{\sigma^{NC}}{\sigma^{CC}}$$

This measurement is possible in SAND thanks to the STT high capability to reduce systematic uncertainties, permitting a good efficiency in the separation between NC and CC events from a ν_e. In fact, the uncertainties on the measurements of the ratio will be dominated by the ones from theoretical models used for the target. It will be possible to achieve the uncertainty on the $\sin^2\theta_W$ measurement of 0.35% from DIS channel.

Another way to measure the Weinberg angle is to study the $\nu_e - e$ elastic scattering in neutral current. This channel is free from hadronic uncertainties but is limited by statistics. In this case the angle can be obtained from the ratio:

$$R_{\nu e} = \frac{\sigma(\bar{\nu}_\mu e \to \bar{\nu}_\mu e)}{\sigma(\nu_\mu e \to \nu_\mu e)}$$

To increase the statistics it's possible to perform a combined analysis with NDLAr detector, obtaining an expected precision on $\sin^2\theta_W$ measurement of 1%.

Due to the different momentum transfer scale with respect to the DIS case, a comparison among them would test the running of $\sin^2\theta_W$. Considering all possible channels, a global fit on electroweak parameters, including $\sin^2\theta_W$, can be performed.

Isospin physics test

The large statistics in neutrino-hydrogen interactions in SAND can be used to test different sum rules, including the Adler one, $S_A = 0.5\int_0^1 dx/x(F_2^{\overline{\nu}p} - F_2^{\nu p})$, and the Gross-Llewellyn-Smith one, $S_{GLS} = o.5\int_0^1 dx/x(xF_3^{\overline{\nu}p} + xF_3^{\nu p})$. The first returns the value of the isospin of the target nucleus, while second the number of valence quarks in the nucleon. Both can be measured as functions of momentum transfer Q^2. The sum S_A is interesting because it is sensitive to possible violations of some symmetries, as the $s-\overline{s}$ sea quark asymmetry. The sum S_{GLS}, instead, can be used to extract the coupling constant of the strong interaction $\alpha_s(Q^2)$.

Combining measurements on hydrogen and other nuclear targets, SAND will be able to perform various tests on isospin symmetry from the measurements of form factors as function of Q^2 and Bjorken x. The isospin symmetry implies that $F_{2,3}^{\overline{\nu}p} = F_{2,3}^{\nu n}$ and for a isoscalar target $F_{2,3}^{\overline{\nu}} = F_{2,3}^{\nu}$.

Strangeness measurements of the nucleon

Differently from the strange quark vector elastic form factors that have been measured with high accuracy, the strange axial-vector form factors G_A^s are still slightly determined. SAND will increase the precision on these terms exploiting the NC elastic scattering off protons $\nu_\mu(\overline{\nu}_\mu)\, p \to \nu_\mu(\overline{\nu}_\mu)\, p$. In the limit $Q^2 \to 0$. the differential cross section becomes:

$$\frac{d\sigma}{dQ^2} \propto G_1^2 = \left(-\frac{G_A}{2} + \frac{G_A^s}{2} \right)^2 \tag{3.3}$$

The term G_A is the known axial form factor and can be obtained in SAND from the ratios of the NC elastic scattering and the corresponding quasi-elastic process: $R_{\nu p}(Q^2) = \sigma(\nu_\mu\, p \to \nu_\mu\, p)/\sigma(\nu_\mu\, n \to \mu^-\, p)$ and $R_{\overline{\nu}p} = \sigma(\overline{\nu}_\mu\, p \to \overline{\nu}_\mu\, p)/\sigma(\overline{\nu}_\mu\, p \to \mu^+\, n)$.

Furthermore, the resolution of STT will enable SAND to measure different decay channels of some charmed hadrons, including $\mu\mu$ and μe inclusive semi-leptonic channels with high statistics. These measurements on charm fragmentation can probe the strange quark content of the nucleon.

Nucleon structure and QCD test

Thanks to the high precision in determination of neutrino and antineutrino fluxes, SAND will be able to measure the structure functions and cross sections, in particular F_2, xF_3, F_L, F_T studying both neutrino and antineutrino DIS process. Given the statistics and energy range in DUNE, it will be possible to perform global fit on QCD in order to study Parton Distribution Functions (PDFs) as well as perturbative and non-perturbative corrections over a wide range of Q^2 and Bjorken x. To separate valence and sea quark distributions, d and u distribution, s and $\overline{s}$ distributions, the presence of both hydrogen and other target

nuclei is needed. All these analyses can be included in ongoing development of collider and fixed-target electron experiments.

Other tests on QCD can be done, in particular through the study on QE interactions on hydrogen, it will be possible to test radiative correction to β-decay and possible violations of CKM matrix unitarity.

Neutrino-Nucleus interaction study

Exploiting the possibility for the STT to be instrumented with different target nuclei, SAND will study the internal structure of the nucleus by measuring the form factors and cross-sections, paying attention to nucleon structure modifications inside a heavy nucleus.

Also final state interactions are important, since they can introduce smearing in the reconstruction of kinematic variables of final state particles.

New physics searches

Beyond Standard Model (BSM) effects would manifest as deviation respect SM predictions, so all precision measurements already listed above are sensitive to some of them.

Also direct searches of new physics are possible, in particular the study and test of MiniBooNE low energy anomaly, thanks to the similar ratio of L/E and the good electron identification capability of the STT. The explanation given by MiniBooNE collaboration is the oscillation into sterile neutrinos and can be tested measuring the CC ratio for both neutrinos and antineutrinos as a function of L/E:

$$R_{e\mu}(L/E) = \frac{(\nu_e N \to e^- X)}{(\nu_\mu N \to \mu^- X)}$$
$$\bar{R}_{e\mu}(L/E) = \frac{(\bar{\nu}_e N \to e^+ X)}{(\bar{\nu}_\mu N \to \mu^+ X)}$$

as well as NC/CC ratios ($R_{\nu p}$ and $R_{\bar{\nu} p}$) as functions of L/E. These measurements are sensitive to both appearance and disappearance mode.

SAND has also an excellent sensitivity on ν_τ appearance, thanks to the STT. The τ neutrino could be the result of oscillation with sterile neutrinos or some non-standard interactions (NSI). This detector will be able also to enhance the sensitivity on Dark Sector physics, that includes for examples heavy sterile neutrinos, dark photons, axions, WIMPs and others.

Chapter 4

Simulation tools

In order to evaluate the feasibility of a project, make decision about a certain detector design, estimate the physic performance of an experiment, simulations are mandatory. In particular, in this thesis work, the simulation chain is composed of a first part of event generation and a second part of event reconstruction. All these steps are performed using different software. In this Chapter all these steps of the chain will be described.

4.1 GENIE

GENIE (Generate Events for Neutrino Interaction Experiments) is widely used in the neutrino physics community as a general-purpose neutrino Monte Carlo event generator. It provides a detailed simulation of neutrino interactions across a broad energy range, from MeV to PeV, with emphasis for the few-GeV scale [48]. Released for the first time in 2007, after three years of work, it is ROOT-based and developed entirely in C++ language using object-oriented methodologies [49]. Many developers of this software were part of other Monte Carlo generators used in neutrino experiments; this guarantees knowledge exchange from previous experiments and continuity.

The large neutrino energy range that GENIE wants to cover gives rise to some challenges, in particular in the few-GeV range. This range, in fact, is the boundary between perturbative and non-perturbative regimes and is very interesting for current and future long-baseline precision experiments using accelerator-made neutrino beam. GENIE provides detailed description of the main scattering mechanisms for all neutrino flavors and target types, which can be categorized into three groups: nuclear physics models, cross-section models and hadronization models. At different neutrino energies, in fact, neutrino-nucleus interaction involves different parts of the nucleus and processes. At high energies ($E_\nu > 10$ GeV) neutrino interact with a single quark of the nucleon, at lower energies instead the interaction involves a single nucleon (proton or neutron). As said before, the few-GeV is a sort of *transition region* that is boundary for different models and the code must pay attention to not generate inconsistency, discontinuities or double counting here.

To simulate the interactions in the Near Detector, a GENIE-based application is used, which manages the definition of the detector geometry in a `gdml` file; allowing for flexibility in selecting whether the interactions take place in the whole geometry or only in a specific

region of the detector. As input, GENIE also requires the fluxes of all the neutrinos produced by the beam. Flux descriptions are derived from accurate beamline simulations [49] specific to each experiment. Neutrinos are generated randomly, on a surface perpendicular to the beam axis, accordingly to energy distribution passed as input and with direction parallel to the beam axis. Once generated, they are propagated and interact with the detector using GENIE.

In this thesis work, events were generated by GENIE using the SAND geometry [46] as input, along with `dk2nu` files [50]. These files contain all the information about the parent particles, such as momentum and energy of mesons that decay into neutrinos. These files alone are not sufficient and a flux driver file is also required to provide information about the beam's direction and interaction positions at the detector site. The flux driver used for this work was `GNuMi` [51], a standard GENIE format originally developed for reading NuMI neutrino flux ntuples but widely adopted by various neutrino experiments, including DUNE.

4.2 Geometry

The geometry of the Near Detector is created using the General Geometry Description (GGD) application [52]. It is a python-based library that creates `GDML` files with a description of a constructive solid geometry, using conventions from ROOT [53] or GEANT4 [54, 55]. The DUNE collaboration exploits `dunendggd` [56], which is a tool for the creation of the geometry based on GGD and customized for the DUNE Near Detector. The directions of the axes are defined as follows: the positive z-axis coincides with the projection of the beam on the horizontal plane, the positive y-axis is vertical upwards, while the x-axis is along the symmetry axis of the magnet.

The KLOE magnet geometry is modeled using several coaxial cylindrical shells to describe the barrel and two flat disks for the endcaps. The magnet barrel is composed of different layer: an external layer made of iron 37 cm thick, then a 1.5 cm thick aluminum layer, then a copper layer 1 cm thick, and finally another aluminum layer identical to the one just described. Inside the magnet, there is the electromagnetic calorimeter which barrel is composed of 24 modules. Each module is 4.3 m long, 23 cm thick and with bases of 59 cm and 52 cm. Finally, each module is placed at a distance of 2 m from the axis of the cylinder. Endcaps are made of 23 cm thick modules with a variable length depending on the position. Both barrel and endcaps modules are made of a sequence of lead foils 400 μm thick and polystyrene scintillator foils 700 μm thick.

The tracker subdetector used by this analysis is the Straw Tube Tracker, as described in Section 3.2.3. Its geometry is implemented as tracking modules, each composed of a sequence of different layers: the target slab, the radiator foils, two layers of straw tubes along the x-axis direction, and finally two layers of straw tubes along the y-axis direction. The target foil is made of C_3H_6 or graphite. Radiator foils are modeled as a unique volume composed of air and C_3H_6 material. The straw tubes are filled with a mixture of Argon and carbon dioxide. There are 78 modules with C_3H_6, 7 modules with graphite as target, and 5 modules without the radiation foils. In order to cover all the available internal volume of the calorimeter, the area on the xy plane varies for each module.

As the final element of the SAND geometry, GRAIN is also included, represented as a

liquid argon volume positioned upstream in the inner volume.

A representation of SAND geometry is shown in Fig. (4.1).

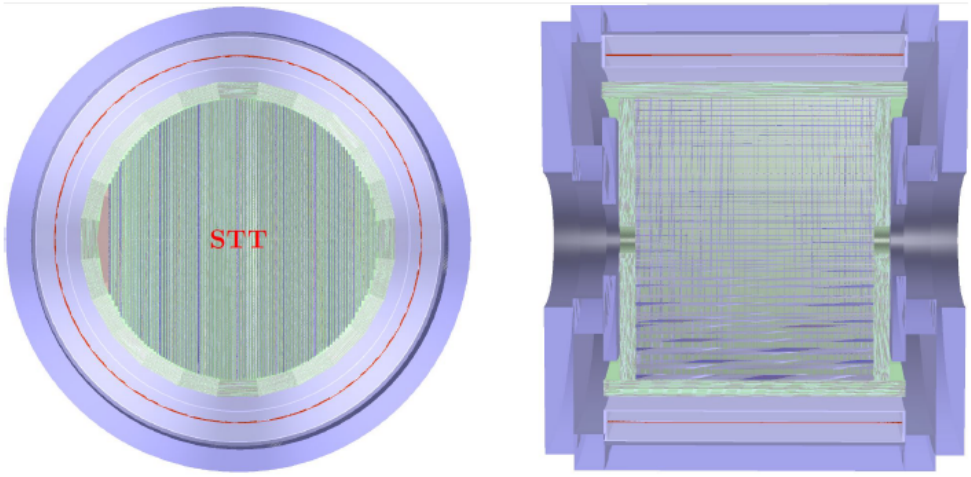

Figure 4.1: Geometry of the SAND detector [34].

4.3 Edep-sim

The energy deposition simulation (edep-sim) [57] is a wrapper around GEANT4 [54] particle propagation simulation toolkit. It propagates particles in a certain geometry that is given as input, as well as particles kinematics. The input files are GDML or ROOT file for the geometry while different formats are supported for the kinematics, including both GENIE and NEUT [58] output files. The GENIE output file format used in this work is RooTracker, a ROOT tree developed by the T2K collaboration.

Different options are possible in edep-sim when compiling a macro in `.mac` format. Included in *edep-sim* there is also a simple event display that reads the output ROOT file and can be useful to debug the geometry and other input files. It can be useful in order to understand how events look like; it can be run using *edep-disp* command.

4.4 Sandreco

Sandreco is the code that the collaboration uses for event reconstruction in SAND [59]. It is written in C++ and it can be installed both on CNAF and FNAL computing farms. For this thesis, it was used on CNAF machine, on which is build with *CMake*. It takes, as input, the output file of *edep-sim* producing different files containing trees with the desired quantities. It is made up of six different executables, each with a specific function.

- **Digitize** performs digitization: the conversion from simulated energy deposition in the detector to digital signal obtained from it.
- **SANDECALClustering** clusterizes the ECAL DAQ in clusters of reconstructed cells.

- **Reconstruct** reconstructs track in STT and cluster in ECAL.
- **Analyze** identifies particles and assign to them different quantities, as momentum.
- **FastCheck** produces plots to check if everything is ok.
- **Display** displays the events.

Some of these executables produce outputs that are used as inputs by others. The *sandreco* software is available on GitHub and is still under development. A first official release is expected to be issued in the near future. Not all executables need to be run; it is possible to execute only a subset, as was done in this work. Specifically, we used only the *Digitize* and *Reconstruct* executables, as shown in the simulation and reconstruction chain of Fig. (4.2).

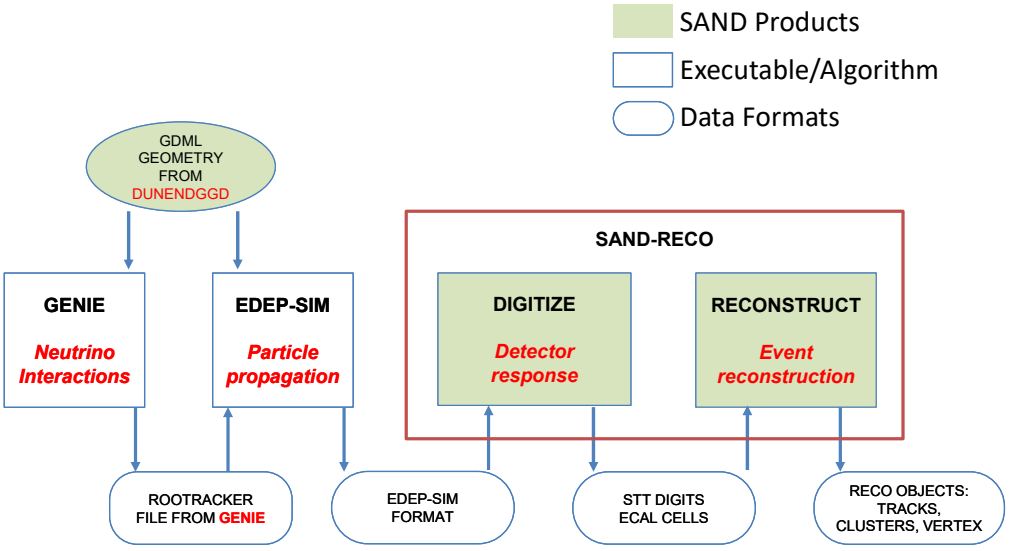

Figure 4.2: Block diagram of sand simulation and reconstruction.

4.4.1 Digitization

Digitization is the simulation of the digital signal response obtained from the DAQ system. It is implemented differently for the calorimeter and for the straw tubes. In the ECAL, the digitization requires the segmentation into cells and the corresponding simulation of the photo-electron production. The STT digits are obtained simply by assigning the energy deposition to the corresponding tube. In both cases, the output of *edep-sim* is input to the digitization process that produces a `TTree` [60] stored in a ROOT file. The output tree has two branches: one for the ECAL and another for the STT, named `cell` and `tube`, respectively.

ECAL Digitization

As just said, the ECAL digitization involves the detector segmentation and signal formation. Each module is divided in 5 layers, numbered from 0 (the inner one) to 4 (the outer).

The thickness of each layer is 4.4 cm except for the outer that is 5.4 cm. Each layer is suddenly divided in 12 cells numbered from 0 to 11 for what concerns the barrel modules, while for the endcaps, each module is divided in 45 cells with equal area. Each module is numerated: from 00 to 23 in the clockwise direction along x-axis for the barrel, number 30 and 40 for the endcaps. In this way each cell can be uniquely associated to a 5 numbers ID: cell + 100*layer + 1000*module.

For each cell, the light produced in it is read out from both side of the module by PMTs. The number of photo-electron produced by a hit is simulated taking into account the attenuation of light in the fiber and the energy to photo-electron conversion factor. Each hit is associated to the correspondence cell position, time and energy deposition dE, in order to compute the number of photo-electron produced by a hit. Collecting all hits in a certain cell, it's possible to determine the response of that cell. The number of photo-electron produced a hit (N_{pe}) can be obtained from a Poisson distribution with mean value given by:

$$\mu_{pe} = dE\, A\, E_{pe} \tag{4.1}$$

where A is the attenuation factor and E_{pe} the conversion factor between energy deposited and photo-electron produced. This quantity has been calculated from the KLOE collaboration and is equal to 18.5 [61]. The attenuation factor can be expressed as:

$$A = p_1 \cdot \exp(-\frac{d}{alt_1}) + (1 - p_1) \cdot \exp(-\frac{d}{alt_2}) \tag{4.2}$$

where d is the distance between the hit and the photo-cathode, p_1 is equal to 0.35, alt_1 is 50 cm and alt_2 changes with layers id. It is equal to 430 cm for layers 0 and 1, 380 cm for layer 2 and 330 cm for layers 3 and 4.

Once number of photo-electrons produced by a hit is calculated and grouped in the correct cell, the ADC (Analog to Digital Converter) signal must be assigned to the Photo-Multiplier for each event. In this simulation the two number coincide.

Also an arrival time to the PMT must be assigned to each photo-electron produced. It is given by:

$$t_{pe} = t_{cross} + t_{decay} + d \cdot u_{ph} + \text{Gauss(1 ns)} \tag{4.3}$$

where t_{cross} is the time associated to the particle that crosses the the cell, t_{decay} is the scintillation decay time, $d \cdot u_{ph}$ is the time needed to the signal to propagate from the hit to the PMT: u_{ph} in fact is the velocity of the photon in the fiber. Finally Gauss(1 ns) is the gaussian smearing that corresponds to the PMT uncertainty. The value of t_{decay} is obtained from the same formula used by the KLOE collaboration:

$$t_{decay} = t_{scint}\left(\frac{1}{r_{ph}(1)} - 1\right)^{t_{scex}} \tag{4.4}$$

where $t_{scint} = 3.08$ ns and $t_{scex} = 0.588$ while r_{ph} is a random number between 0 and 1. These values were taken from the KLOE collaboration. Two different TDC times (t_{TDC_1} and t_{TDC_2}) are computed as 15% of each constant fraction.

STT digitization

In the STT, digitization is done by grouping together the hits produced in the same Straw Tube and assigning position, time and deposited energy to each group. Each STT module

has its own identifier that increases from the upstream to the downstream side of SAND; each module has two different orientations of the tubes: XX or YY. Due to this, only two coordinates can be associated with the digit: z and y for the vertical orientation, while z and x for the horizontal one. The time is instead assigned as the mean between the time coordinate of the first start point and the last end point of the hits in the tube. The energy is simply the sum of all energies deposited in that tube.

4.4.2 Reconstruction

The event reconstruction takes as input both the output from the digitization process and the output of *edep-sim* (Monte Carlo truth). Of course, the second one will not be available with real data. The reconstruction involves two distinct algorithms: one for the STT, which searches for tracks and another for the ECAL, which identifies clusters. The output is a ROOT file, as before, containing a tree with two branches with name `track` and `cluster`.

ECAL reconstruction

In the ECAL, reconstruction is performed by grouping cell digits into clusters and associating a track to each of them. This job is performed by an algorithm that identifies the particle with the highest energy deposition in each cell, currently based on the MC truth. Then, it groups the cell digits in which that particle is the one that released the largest amount of the energy.

For each digit, the position is evaluated in the following way: the z coordinate is the center of the cell for both barrel and endcaps. For barrel, the y coordinate is computed as the center of the cell, while the x coordinate is obtained from the following formula:

$$x = \frac{t_{TDC_1} - t_{TDC_2}}{2u_{ph}} + x_{cell} \tag{4.5}$$

where x_{cell} is the x coordinate of the center of the cell and t_{TDC_1}, t_{TDC_2} and u_{ph} are defined in eq. (4.3). For what concerns the endcap module cell digits, the definition of y and x are switched.

Finally, the time of the cell digit is evaluated starting from the two TDC times:

$$t = \frac{1}{2}(t_{TDC_1} + t_{TDC_2} - u_{ph} \cdot L) \tag{4.6}$$

Once the spatial position and time are assigned to each cell digit, the coordinates of the cluster center $(x_{cl}, y_{cl}, z_{cl}, t_{cl})$ are computed. They are taken as the weighted mean of the coordinates of all digits which belong to the cluster, using the energy deposited E_{cell} as weight.

STT reconstruction

In the STT, the reconstruction algorithm aims to group digits that produce the same track. Once the track is found, a fit is performed, and the parameters are inferred. Two different assumptions are made in the reconstruction: uniform magnetic field along the x-axis and energy loss not taken into account. This implies that the trajectory of the

particle describes a helix with linear motion along x and circular motion in the zy plane. It's possible to write the parametric equations expressed as function of the path along the helix s, in order to fit the track of charged particle [62]:

$$\begin{cases} z(s) = z_0 + R\big[\cos\left(\Phi_0 + \frac{hs\cos\lambda}{R}\right) - \cos\Phi_0\big] \\ y(s) = y_0 + R\big[\sin\left(\Phi_0 + \frac{hs\cos\lambda}{R}\right) - \sin\Phi_0\big] \\ x(s) = x_0 + s\sin\lambda \end{cases} \tag{4.7}$$

where x_0, y_0 and z_0 are the starting point of the track (at $s = 0$), R the radius of the helix, Φ_0 is the angle between the z-axis and the segment that connects the center of the circle (y_0, z_0) and the starting point of the track (y_c, z_c), λ is the *dip-angle*: angle between the initial velocity of the particle and the zy plane. Finally, $h = \pm 1$ is the sense of rotation of the helix (+1 if clockwise, -1 if counter-clockwise). Representation of the particle's trajectory is given in Fig. (4.3).

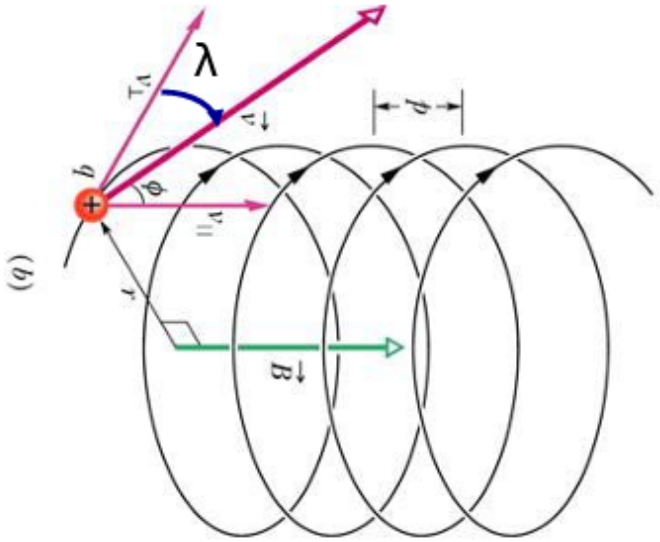

Figure 4.3: Representation of the trajectory of a particle in a magnetic field [62].

The trajectory of the charged particle can be projected onto the z-y plane describing a circle defined as:

$$(z - z_0 + R\cos\Phi_0)^2 + (y - y_0 + R\sin\Phi_0)^2 = (z - z_c)^2 + (y - y_c)^2 = R^2 \tag{4.8}$$

where y_c and z_c are the coordinates of the center of the circle on this plane. Starting from the information on the hit position recorded in the horizontal straw tubes, on the z-y plane, it's possible to perform a circular fit in order to obtain the most probable values of the radius R and the center of the circle (y_c, z_C). Projection in the *zy-plane* is reported in Fig. (4.4).

Once these two quantities are defined, it necessary to reconstruct also the *dip-angle* λ. To do that, an approximation is done: circular trajectory is approximated to a parabolic one. This can be done applying Taylor expansion in s/R, possible if this quantity is much less than unity. This is true if the circular trajectory described by the particle is small

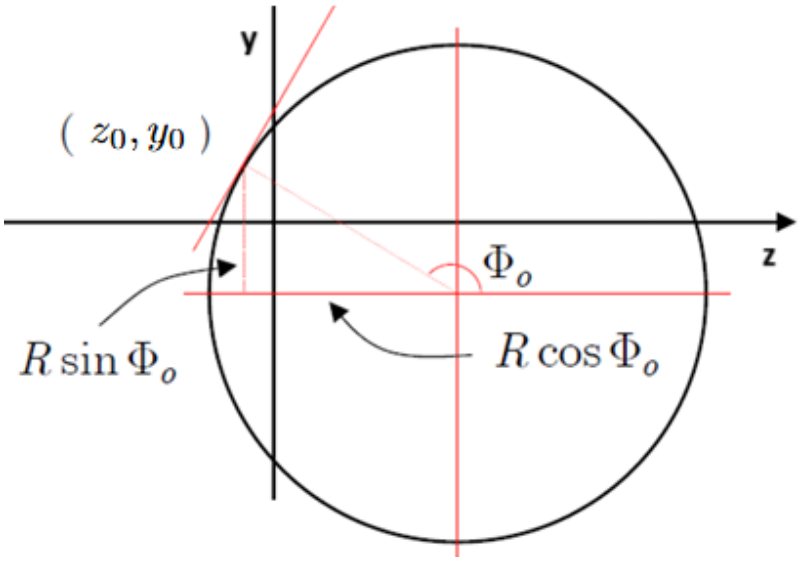

Figure 4.4: Projection in the zy-plane of the particle's trajectory in a magnetic field along x-axis.

with respect to the radius R, this is true for muons in SAND. With this approximation, the eq. 4.7 becomes:

$$\begin{cases} z(s) = z_0 - hs\cos\lambda\sin\Phi_0 - \frac{s^2\cos^2\lambda}{2R}\cos\Phi_0 \\ y(s) = y_0 - hs\cos\lambda\cos\Phi_0 - \frac{s^2\cos^2\lambda}{2R}\sin\Phi_0 \\ x(s) = x_0 + s\sin\lambda \end{cases} \tag{4.9}$$

Then, it's possible to apply a coordinates transformation making a rotation of the z-y plane by an angle $\varphi_0 = \pi/2 - \Phi_0$ obtaining the $\rho - y'$ plane:

$$\begin{cases} \rho = z\cos\varphi_0 + y\sin\varphi_0 \\ y' = -z\sin\varphi_0 + y\cos\varphi_0 \end{cases} \tag{4.10}$$

and the equations of motion in the x-y' plane become:

$$\begin{cases} x = x_0 + \rho\tan\lambda \\ y' = d_0 - \frac{h}{2R}\rho^2 \end{cases} \tag{4.11}$$

where d_0 is the impact parameter: the distance in the z-y plane between the starting point and the origin of coordinates. Using the x and z position from the straw tubes and the values y_c, z_c and R from the previous fit, coordinate y can be extrapolated using:

$$y = y_c + h\sqrt{R^2 - (z - z_c)^2} \tag{4.12}$$

while for the coordinates ρ and$y$' the values of sine and cosine of φ_0 is needed. They can be calculated from:

$$\begin{cases} \cos\varphi_0 = \frac{h(y_0 - y_c)}{R} \\ \sin\varphi_0 = -\frac{h(z_0 - z_c)}{R} \end{cases} \tag{4.13}$$

Using all these quantities obtained, we can infer the value of the *dip-angle* λ from a linear fit on the first line in eq. 4.11.

These information can be used to compute the transverse momentum of the particle:

$$p_T = 0.3 \cdot B\, R \tag{4.14}$$

and consequently the three components of the momentum:

$$\begin{cases} p_z = p_T \cos\varphi_0 \\ p_y = p_T \sin\varphi_0 \\ p_x = p_T \tan\lambda \end{cases} \tag{4.15}$$

Finally, summing in quadrature the three components, it's possible to recover the total module of the total momentum; that can be approximated to the energy for relativistic particle:

$$E \simeq p = \sqrt{p_x^2 + p_y^2 + p_z^2} \tag{4.16}$$

Chapter 5

Neutrino beam monitoring analysis

Beam monitoring at Near Site is a crucial element in a neutrino experiment. In order to validate observations at the Far Detector site, is critical to detect any potential variations in the neutrino beam caused by an improper acceleration operation and anomalies. This can be done by comparing nominal and altered spectra, using various possible observables and datasets.

In this study, muon momentum of neutrinos interacting in the upstream calorimeter was selected for analysis. The description of all considered beam variations can be found in the Appendix and in Ref. [63].

In this Chapter, all the steps for the analysis will be described: starting from the event selection, passing trough the detector efficiency, the description of the statistical tests and finally the results.

5.1 Simulated dataset

For this work, a sample of $\sim 10^6$ ν_μ events has been generated, following the simulation procedure described in the Chapter 4. This dataset corresponds to 10^{18} protons on target (POT) or, approximately, to 4.5 hours of data taking. In this sample, the interactions take place in the entire SAND volume.

A second sample has been generated, forcing the neutrino interactions in the calorimeter. Considering both samples, a dataset equivalent to 20 hours of data taking was simulated.

5.2 Characterization of neutrino interaction in SAND

In order to make a correct beam monitoring, a preliminary characterization of the sample considered is required. To this purpose, we take the nominal sample (the one without variations) and we look at different quantities using the SAND detector. Some important quantities are: vertex position, selection efficiency and reconstruction resolution.

In this section, we considered only the first simulated dataset, composed of interactions in the entire SAND volume.

5.2.1 Event selection

As just said, a sample of ∼1 million events have been generated in the entire SAND volume. Some cuts have been made to select only the events that are useful for beam monitoring. There are different reasons that explain the choices made in this work.

First of all, we simulated both neutral and charged current neutrino interactions. The first cut is applied on the type of interaction: we select only **charged current** ones. This is performed looking at the Monte Carlo truth, because the software does not provide currently a way to recover this quantity from the reconstruction.

The second cut performed regards the **position of the interaction vertex**. From the initial simulation of interactions in all SAND volume, we selected the subsample that includes events whose interaction vertices are placed in the front calorimeter. For us, this means the region of the calorimeter that has a value of z coordinate less than 23000 mm, in the Near Detector hall coordinate system. This region was chosen because it has more statistics, thanks to its greater density, than the inner tracker region. Another reason that justifies this choice is the following: muons generated in the front calorimeter are expected to have a long track in the tracker. We expect longer tracks to be reconstructed better than shorter ones. Also in this case, we apply the cut, using the Monte Carlo truth vertex positions, for the same reason as before.

The third cut is applied on the **neutrino energy**. We selected events whose neutrino energy is less than 20 GeV. We made this choice because for this study we need to re-weight the reconstructed muon momentum nominal distribution. To this purpose, the weights used are the bin contents of a histogram whose range is from 0 to 20 GeV. This fact forced us to cut the energy greater than this value. This cut does not significantly impact our work, because the vast majority of muon neutrinos from the beam are expected to be below 20 GeV. The peak of the distribution is placed at few GeV, then decreases rapidly, as it is possible to see from the blue line in Fig. (5.1). Also here, neutrino energies are taken from the Monte Carlo truth.

Finally, the last cut was applied on the reconstruction's results. We selected events whose **muon momentum** has been **reconstructed correctly** in the inner tracker: we mean muons whose circular and linear fits described in Section (4.4.2) both produce non-null values. As described in Chapter 4, *sandreco* uses some information from the Monte Carlo truth; so, the reconstruction itself is partially cheated.

Applying all these cuts we obtained a sample of charged current events whose vertices are placed in the front calorimeter and that have an energy less than 20 GeV, and produce well reconstructed muons in the inner tracker. In this way, each event in the sample will have a neutrino energy and an associated reconstructed muon momentum. Distributions of the neutrino energy for the initial and the selected samples are displayed in Fig. (5.1).

The ratio between the number of selected events and the total number of simulated events is:

$$R = \frac{N_{reco}^{ECAL}}{N_{tot}} \tag{5.1}$$

All values are reported in Tab. (5.1). This ratio is important to recover the total number of POT that corresponds to a certain number of interactions in the selected sample. From the POT, it is easy to compute the run time.

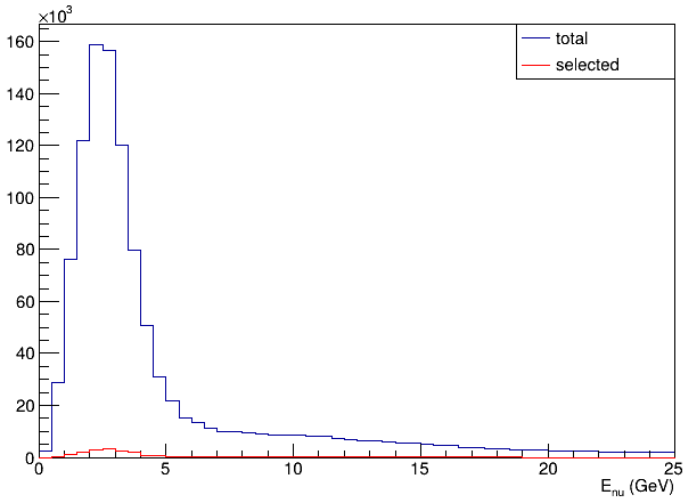

Figure 5.1: Distribution of the neutrino energy for the initial total sample (blue) and the selected one (red).

N_{tot}	1121444
N_{reco}^{ECAL}	18881
R	0.0168 ± 0.0001

Table 5.1: Number of entries in the total SAND volume, in the selected sample and its ratio for the dataset corresponding to 10^{18} POT.

5.2.2 Muon reconstruction performance

To evaluate the muon reconstruction performance, a comparison between the true momentum and the reconstructed one has been performed.

First of all, the reconstruction efficiency has been computed. It is the ratio between the number of selected events with a well reconstructed muons (N_{reco}^{ECAL}), and the total number of events in the selected sample (N_{CC}^{ECAL}).

$$\epsilon^{ECAL} = \frac{N_{reco}^{ECAL}}{N_{CC}^{ECAL}} \tag{5.2}$$

This quantity can be evaluated as a function of the true muon momentum, as shown in Fig. (5.2) and in Fig. (5.3). It is possible to see that the reconstruction efficiency increases with the true muon momentum.

The difference between the true and the reconstructed momentum is shown in Fig. (5.4), along with the interpolation with a Gaussian curve. It worth noting that the mean of the fit is pretty close to zero, with a positive value. This indicates that our reconstructed momentum tends to be underestimated. This could be caused by a muon energy loss in the calorimeter. Anyway, for the purpose of this work, this is not relevant. In fact, beam monitoring is based on the comparison of two different distributions, the nominal and the varied. Any systematic effect that equally affects both distributions is negligible.

The scatter plot of the true versus the reconstructed muon momentum is shown in Fig. (5.5). As expected, the majority of points are placed on the straight line with slope of 1,

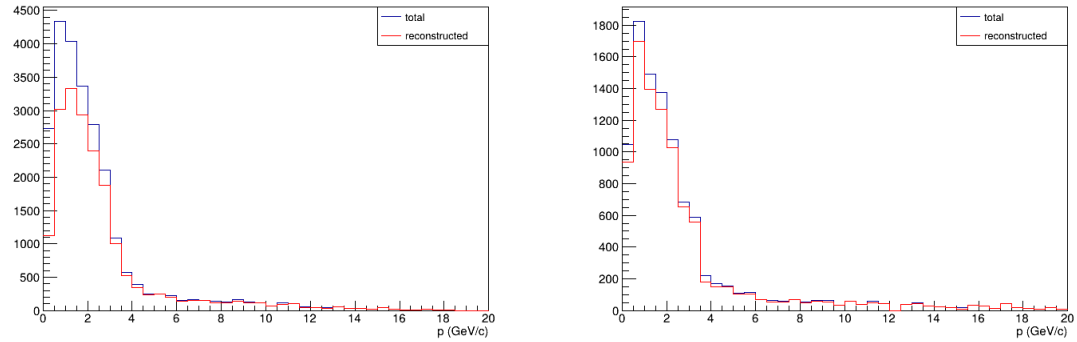

Figure 5.2: Distribution of the true muon momentum before (blue) and after (red) the muon reconstruction for neutrino interactions in the front calorimeter (left) and in the inner tracker (right).

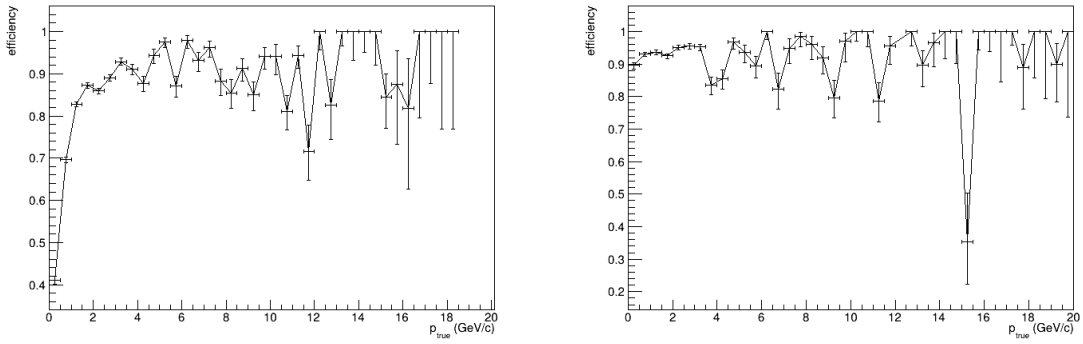

Figure 5.3: Efficiency of muon reconstruction as a function of the true muon momentum for neutrino interactions in the front calorimeter (left) and in the inner tracker (right).

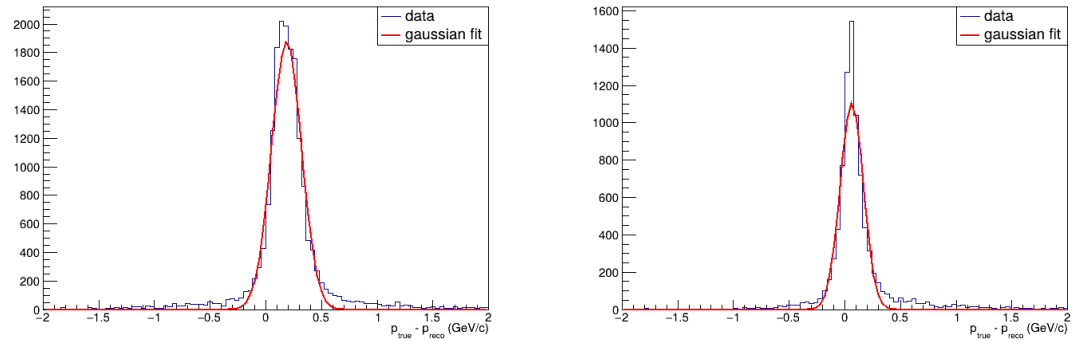

Figure 5.4: Difference between true and reconstructed muon momentum for events passing the kinematical cuts for neutrino interactions in the front calorimeter (left) and in the inner tracker (right).

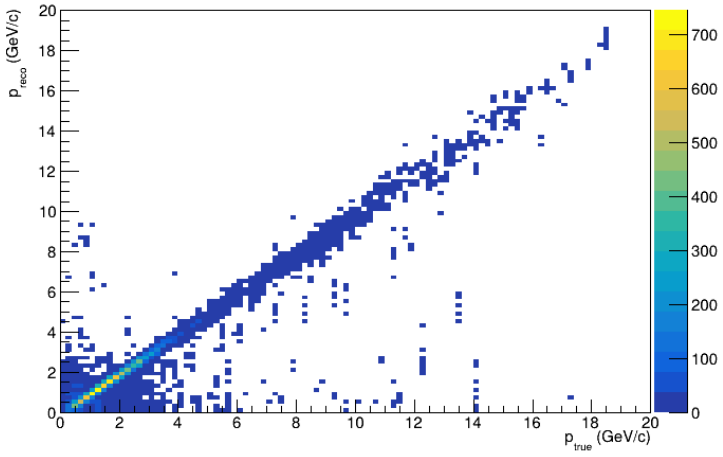

Figure 5.5: Scatter plot of the true versus the reconstructed muon momentum. As expected, the majority of points lie in the straight lines with slope of 1.

showing that the reconstruction has a good linearity.

Furthermore, we did the same calculations also for a sample composed of charged current events in the inner tracker obtained with the same kinematical cuts. As before, we define the efficiency as the ratio between the number of well-reconstructed events N_{reco}^{STT} and the number of charged current events N_{CC}^{STT}:

$$\epsilon^{STT} = \frac{N_{reco}^{STT}}{N_{CC}^{STT}} \tag{5.3}$$

As shown in Fig. (5.3, right), in this case the efficiency doesn't depends so much on the muon momentum, and it is pretty stable near 1. Residuals between true and reconstructed muon momentum is closer to zero, as shown in Fig. (5.4, right). This is expected because the density, and consequently the muon energy loss, is less in the inner tracker with respect to the calorimeter. The bias is also significantly reduced, even if not fully removed. Further investigatios on reconstruction performances are necessary but beyond the scope of this work.

Results are summarized in Tab. (5.2).

	inner tracker	front calorimeter
N_{CC}	10125	108665
N_{reco}	9341	18881
ϵ_{reco}	0.92 ± 0.02	0.79 ± 0.01
μ (GeV)	0.062 ± 0.001	0.185 ± 0.001
σ (GeV)	0.104 ± 0.001	0.135 ± 0.001
χ^2	1555	2527
$d.o.f$	92	96

Table 5.2: Number of charged current events, the ones that are well reconstructed, the reconstruction efficiency and all parameters from the Gaussian fit for the selected sample and the inner tracker one.

5.2.3 Vertex position

The knowledge of the position of the neutrino interaction vertex is crucial in this work because it is a quantity used to select the sample considered. As just said, *sandreco* has been used as reconstruction software; at this stage, it does not provide a reconstructed position of the interaction vertex. Because of this, we were forced to take the interaction position from the Monte Carlo truth.

If we simplify the detector geometry, SAND is made up of different areas with different uniform densities. This implies that, in each part, the distribution of the number of vertices is uniform. We expect areas with higher density to have a higher number of interactions. The plots of the interaction distributions are shown in Fig. (5.6). From the figure, it is possible to see that many interactions are placed in the iron joke and in the calorimeter, both in the barrel and in the endcaps. This matches our expectations because their densities is greater than the tracker.

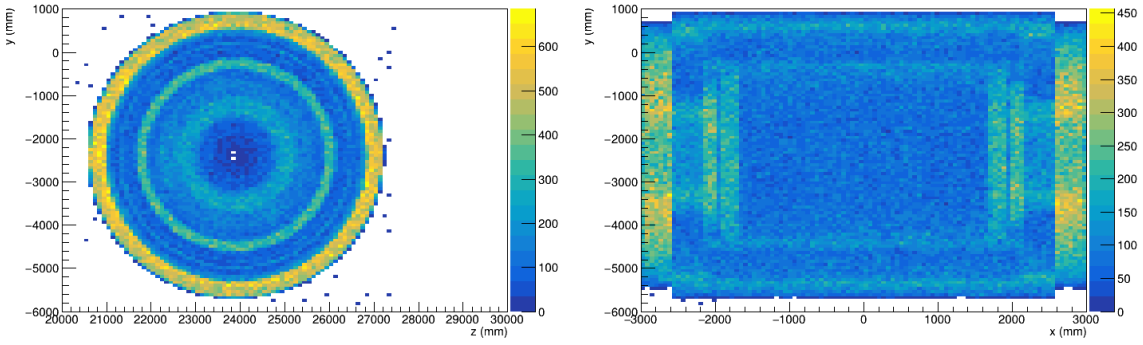

Figure 5.6: Position of the interaction vertices from Monte Carlo truth in the zy-plane (left) and xy-plane (right). Areas with more vertices densities are the iron joke and the calorimeter, both barrel (left) and endcaps (right).

From this initial sample, we selected interactions using the criteria already discussed in Section (5.2.1). In this way, we obtained the initial nominal sample, for which the distributions of the interaction vertices positions are shown in Fig. (5.7). The calorimeter has a uniform density, this implies that the number of interactions has a uniform distribution as well.

5.3 Generation of varied spectrum

After having generated the total number of events, they are selected following the criteria already mentioned in Section (5.2.1): charged current events whose vertices are placed in the front calorimeter with a neutrino energy less than 20 GeV, whose muon is well reconstructed in the STT. This sample is the nominal sample: the sample without variations. From that, we can produce the distributions of neutrino energy and muon reconstructed momentum.

Due to the fact that only flat flux histograms were provided by DUNE for the varied beams, we could not perform a full simulation and generate events with different fluxes to

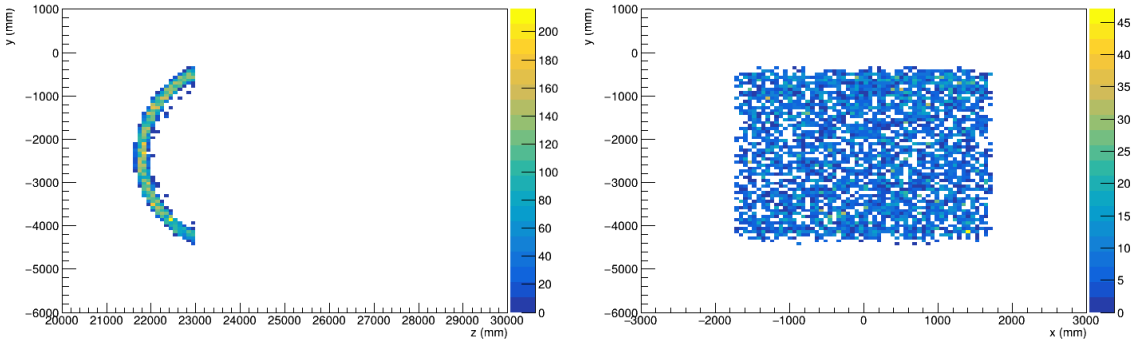

Figure 5.7: Position of the interaction vertices from Monte Carlo truth for the selected sample in the zy-plane (left) and xy-plane (right).

compute the distributions of the reconstructed muon momentum. The solution we opted for was to re-weight the reconstructed muon nominal distribution. Weights were computed making the ratio bin-by-bin between the two fluxes: we computed the ratio between each bin entry of the altered and nominal flux.

For this work, 93 different neutrino fluxes were considered corresponding to the beam anomalies reported in the Appendix and taken from Ref. [63].

In following, the variation called `BuffletScrapingInX_pos_1_sigma` was used as example. This choice was driven by the fact that it is one of he most sensitive variation among the available options. It corresponds to a displacement of the pencil beam of 8.001 mm in the positive x direction.

The varied flux is reported in Fig. (5.8), where the nominal flux is also shown. Weights, instead, are reported in Fig. (5.9).

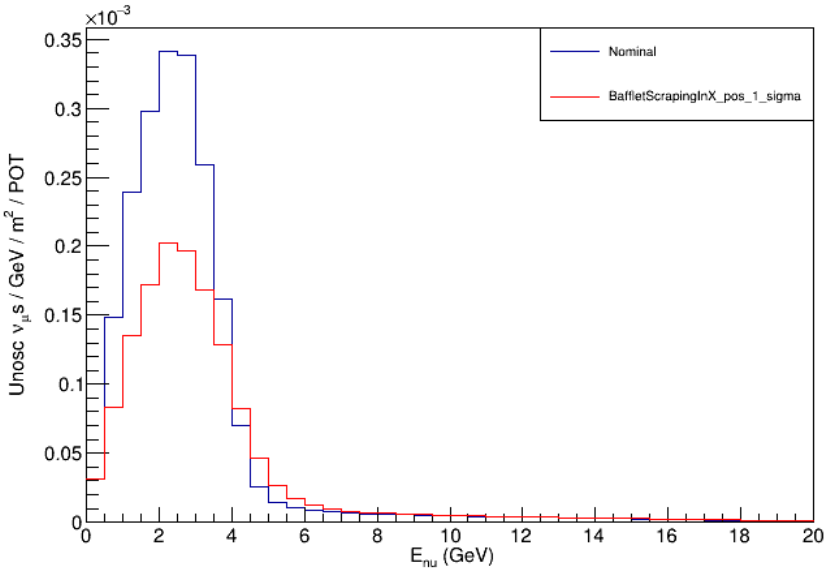

Figure 5.8: Distribution of the nominal neutrino flux (blue) and the altered one (red).

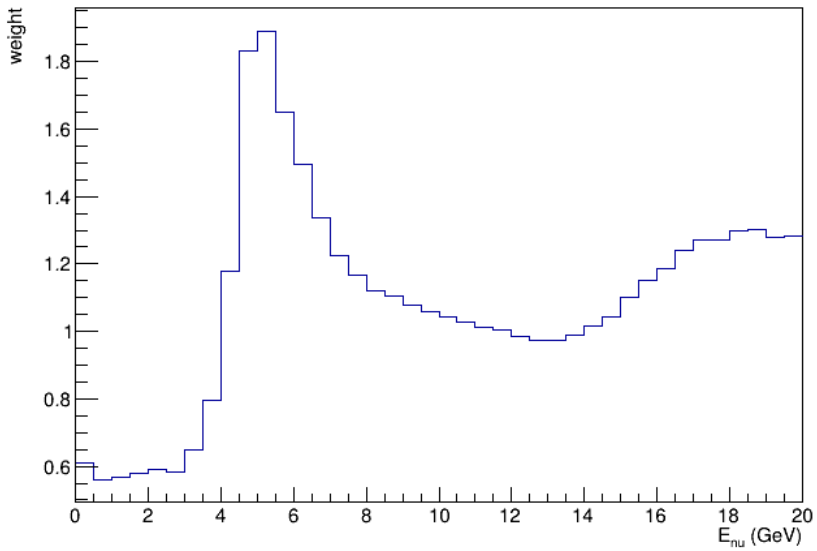

Figure 5.9: Weights for the beam variation `BuffletScrapingInX_pos_1_sigma`.

Note that the binning and range of the histograms were dictated by the flux files, which contain 40 bins in a range from 0 to 20 GeV of neutrino energy. This is not a significant issue, as the neutrino energy spectrum peaks at a few GeV and subsequently exhibits a rapid decline. Moreover, the muon total momentum is about one half of the energy of the neutrino that generates it.

Now we have all the ingredients to build the varied histogram: we fill the histogram with nominal reconstructed muon momentum using the weight from bin of the correspondence neutrino true energy. In this way, we obtain the varied spectrum that must be compared with the nominal one to perform beam monitoring. Plots of neutrino energy and muon reconstructed momentum for nominal and altered case are displayed in Fig. (5.10) and Fig. (5.11) for the beam variation `BuffletScrapingInX_pos_1_sigma`.

5.4 Two-sample test

In order to check if some variations in the beam occurred, a comparison between nominal and varied spectra is needed. In other words, we want to check if the hypothesis that the two spectra are taken from the same distribution is wrong. We can only compare two histograms bin-by-bin using a two-sample test. Many tests are available, but for this work two of them are used: Kolmogorov-Smirnov test and Anderson-Darling test. Both are already implemented in ROOT [64, 65].

5.4.1 Kolmogorov-Smirnov test

The Kolmogorov-Smirnov test consists of measuring the maximum difference between two CDFs (Cumulative Distribution Functions), comparing it with the null homogeneity hypothesis expectation [66]. This test requires unbinned samples, but it can also be used for binned ones if some considerations are done: the size of bins must be small enough.

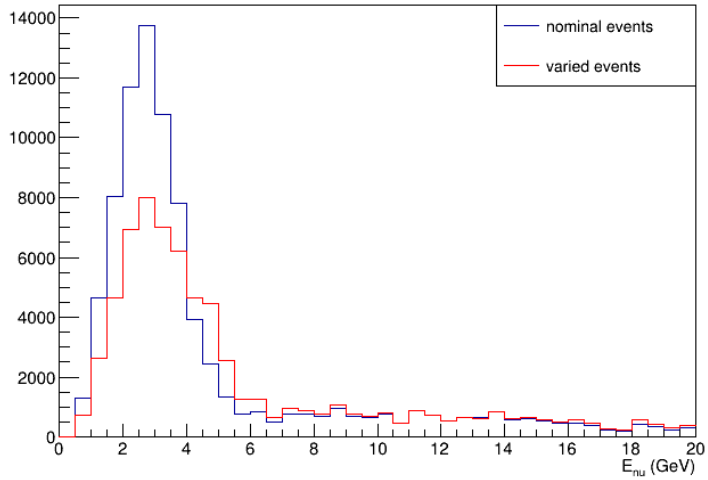

Figure 5.10: Distributions of neutrino energy for nominal (blue) and varied (red) case for the beam variation `BuffletScrapingInX_pos_1_sigma`.

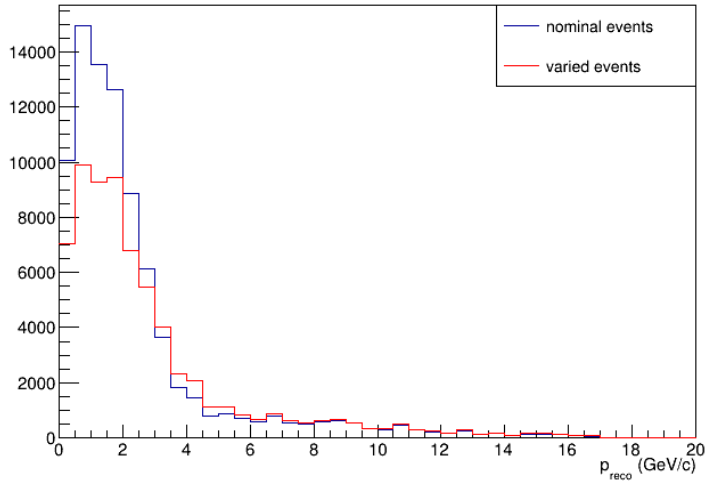

Figure 5.11: Distributions of reconstructed muon momentum for nominal (blue) and varied (red) case for the beam variation `BuffletScrapingInX_pos_1_sigma`.

This is also the strategy used in this work. The CDFs are approximated to histograms as [65]:

$$\begin{aligned} u_{ci} &= \sum_{j=1}^{i} u_i / N_u \\ v_{ci} &= \sum_{j=1}^{i} v_i / N_v \end{aligned} \tag{5.4}$$

The test is then defined as:

$$T_{KS} = \max_i |u_{ci} - v_{ci}| \tag{5.5}$$

The null hypothesis is rejected if:

$$T_{KS} \geq c(\alpha) \sqrt{\frac{N_u + N_v}{N_u \cdot N_v}} \tag{5.6}$$

where $c(\alpha)$ can be approximates as:

$$c(\alpha) = \sqrt{-\ln(\alpha/2) \cdot (1/2)} \tag{5.7}$$

Clearly, this test emphasizes the differences near the peak of two distributions, where most fluctuations are expected for Poisson distribution.

5.4.2 Anderson-Darling test

The Anderson-Darling test is a modified version of the Kolmogorov-Smirnov one, designed to be sensitive to the tail of the CDF. The original test was designed to compare a dataset $x_1, ..., x_m$, that has an empirical CDF $F_m(x)$ with a continuous distribution that has CDF $F_0(x)$ under the null hypothesis [65]:

$$A_m^2 = m \int_{-\infty}^{\infty} \frac{[F_m(x) - F_0(x)]^2}{F_0(x)[1 - F_0(x)]} dF_0(x) \tag{5.8}$$

Scholz and Stephens [67] provided a form of this test in the k-sample case, which in our case becomes:

$$\begin{aligned} T_{AD} = \frac{1}{N_u + N_v} \sum_{j=k_{min}}^{k_{max}-1} \frac{u_i + v_i}{\Sigma_j (N_u + N_v - \Sigma_j)} \Big\{ & [(N_u + N_v)\Sigma_{uj} - N_u \Sigma_j]^2 / N_u \\ & + [(N_u + N_v)\Sigma_{vj} - N_v \Sigma_j]^2 / N_v \Big\} \end{aligned} \tag{5.9}$$

where k_{min} is the first bin where either histogram has non-zero entry, k_max is the last bin where either histogram has non-zero entry. The other terms in the previous equation are:

$$\Sigma_{uj} = \sum_{i=1}^{j} u_i \qquad\qquad \Sigma_{vj} = \sum_{i=1}^{j} v_i$$

$$\Sigma_j = \sum_{i=1}^{j} u_i + v_i = \Sigma_{uj} + \Sigma_{vj}$$

The null hypothesis is rejected at α confidence level if:

$$\frac{T_{AD} - 1}{\sigma_{(N_u+N_v)}} \geq z_2(1-\alpha) \tag{5.10}$$

where $z_2(1-\alpha)$ is the $(1-\alpha)$-percentile of the standard asymptotic function $Z_{k-1} = [T_{AD} - 1]/\sigma_{(N_u+N_v)}$ and $\sigma_{(N_u+N_v)}$ is the standard deviation of T_{AD}.

5.5 Results

Once the nominal events are selected, the spectrum of the varied reconstructed muon momentum is computed in the way described above and compared using Kolmogorov-Smirnov and Anderson-Darling tests. As said before, these two tests are already implemented in ROOT and they are tests on the shape of the two distributions.

In fact, variations can cause a reduction (or an enhancement) of the number of selected events. Because of that, the altered distribution has been normalized to the same number of nominal entries. In reality, Kolmogorov-Smirnov test implemented in ROOT has the option to consider also the different normalization of the two distribution. So, we run the test also with this option, in order to obtain more precise results.

The threshold for the p-value of the tests in order to say that a variation has occurred is set at 0.01. So, if the p-value of the test considered is less than 0.01, we can say that there is a variation of the beam. In other words, if resolved, we can say at 99% of C.L. that a variation in the beam is occurred.

The comparison is done for different numbers of initial nominal events in order to find the minimum number of them needed to discover a variation. This number of events can be converted into protons on target (POT) using the values in the Table (5.1).

Plots of p-value as function of POT are shown in Fig. (5.12) and Fig. (5.13) for all the tests and for the beam variation `BuffletScrapingInX_pos_1_sigma`, which is used as an example. We can see that few 10^{16} POT are sufficient for all tests to find this variation. From the figure, it is evident that the Anderson-Darling test is the most effective. The number of POT can be also converted in time. These correspond to a few hundreds of seconds for all tests.

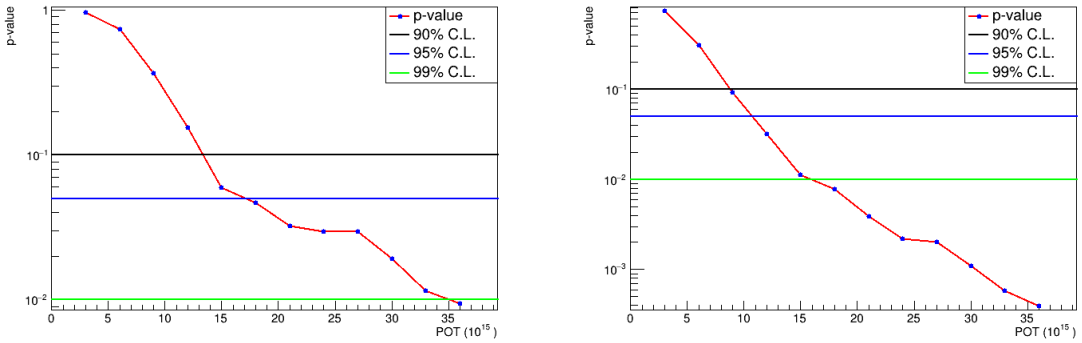

Figure 5.12: p-value of the Kolmogorov-Smirnov (left) and Anderson-Darling (right) shape-only tests as function of POT. The thresholds at 10% (black), 5% (blue), and 1% (green) of confidence level are reported.

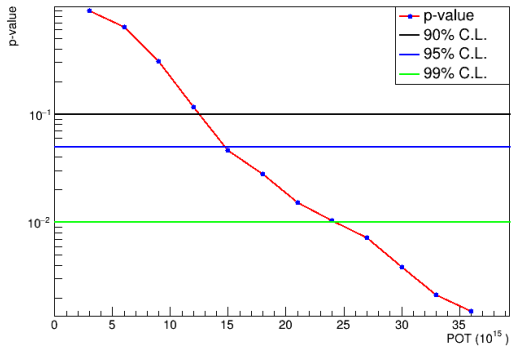

Figure 5.13: p-value for the Kolmogorv-Smirnov test as function of POT, including the different normalization of distribution in the test. The thresholds at 10% (black), 5% (blue), and 1% (green) of confidence level are reported.

As said before, some variations can also cause a modification of the total number of events that pass the selection cut. This is the case for the beam variation used as an example; a reduction of the selected events is evident in Fig. (5.11). Therefore, this quantity can be used for beam monitoring in some cases. The variation considered in this study causes a reduction of $\sim 20\%$ of the number of reconstructed muons that pass the cut.

In this work, we tried to analyze all the other available beam variations. The results are reported in the Appendix. It is possible to see that only variations caused by a displacement of the pencil beam can be discovered with our statistics, which is limited to 20 hours of data acquisition due to the computing power available at the time of this thesis. For the other variations, only lower limits on the required POT, therefore the time spent, can be set.

Nevertheless, data show that the p-value starts decreasing for some variations, even if it doesn't reach any threshold to observe a beam anomaly. These variations are: `HornCurrent`, `HornWaterLayerThickness_neg_1_sigma` and `ProtonBeamRadius`. For a description of them, see the Appendix.

It is reasonable to think that with higher statistics, we will be able to resolve further variations, with specific emphasis on those listed previously.

Another way to improve our results could be to pass through our simulation chain starting from the varied neutrino flux. This was not possible here because the variation's input file format is not compatible with our chain.

Conclusions and outlook

Neutrino physics is one of the most interesting branches in modern particle physics because it proves that the Standard Model is not a complete theory and that there is something beyond it. In fact, a lot of questions in this field are still open. DUNE aims to answer some of them, in particular, the ones regarding oscillations. The main goal of this experiment will be to measure the δ_{CP} oscillation parameter and determine the neutrino mass ordering.

The SAND detector is part of the Near Detector for DUNE experiment. Its main goal will be to reduce systematic uncertainties relevant to the oscillation analysis. Among these, one of the detector's main tasks is the beam monitoring. In order to validate results at Far Detector site, it is crucial to find any possible variations of the beam caused by improper acceleration operation and anomalies.

The purpose of this thesis is to study the feasibility of beam monitoring using SAND via simulations. Among the total number of generated events, we selected the samples containing charged current events that interact in the front calorimeter and that have an energy less than 20 GeV with a muon correctly reconstructed in the inner tracker. This sample corresponds to 4.4×10^{18} POT or, in other words, 20 hours of beam time.

First, a characterization of neutrino interactions of the selected sample was performed. We computed the muon momentum reconstruction efficiency and resolution and analyzed the vertex position distribution. The current reconstruction software shows a small bias in the muon momentum reconstruction. However, since beam monitoring involves comparing two different spectra, any systematic effect of the detector can be neglected as long as it affects both spectra equally.

In this study, 93 different neutrino fluxes were analyzed, each corresponding to a distinct anomaly of the beam or target complex. Beam monitoring is performed by comparing the nominal reconstructed muon momentum spectrum and the varied one using two-sample tests: Kolmogorov-Smirnov and Anderson-Darling. The tests were applied on the shape of the distributions and, for the Kolmogorov-Smirnov test, the different number of events was also considered. The goal is to determine the minimum number of Protons on Target (or equivalently, the beam time) required to observe a beam variation with a p-value threshold of 0.01.

We primarily focus on the most significant variation, caused by a displacement of the beam, resulting in the beam scraping the baffle upstream of the first horn. The results show that a few minutes of data collection are sufficient to observe this effect.

These tests were also repeated for the other variations, but they could not be resolved due to limited statistics, which were constrained by the computing resources available at the time of this thesis.

Appendix

In the following tables, results are reported; in particular, the number of POT and beam time required to obtain a p-value of 0.1, 0.05 and 0.01 (from the top to the bottom) for the considered test. The first column describes the type of variation. Terms "KS", "shape KS" and "shape AD" indicate respectively: Kolmogorov-Smirnov test considering the different normalization, shape-only Kolmogorov-Smirnov test and shape-only Anderson-Darling test.

Shape-only test means that the different shapes of the distributions are compared, so the altered one has been normalized to the total number of nominal entries. For what concerns the name of the variations: the letter `X`, `Y`, `Z` in the variations name indicate the axis on which it is applied; the suffix `pos_1_sigma` (`neg_1_sigma`) indicates a variation of 1 sigma in the positive, or negative direction of the respective axis.

The list of variations is the following:

- `BaffletScraping`: displacement of 8.001 mm of the pencil beam;
- `DecayPipe3SegmentBowing`: decay pipe is segmented in three pieces. The central one is shifted by 2.5 cm;
- `DecayPipeDisplaceTransverse`: displacement of 2.5 cm of the decay pipe;
- `DecayPipeEllipticalCrossSection`: ellipse with A (x-axis) or B (y-axis) varied by 2.5 cm, while other dimension fixed to nominal radius;
- `DecayPipeGeoBField`;
- `DecayPipeRadius`: difference of 2 cm in the decay pipe radius;
- `DecayPipeTilt_DSOA`: displacement of 2.5 cm of the decay pipe constraining the downstream part to remain fixed on-axis;
- `HornADisplaceLongitudinal`: displacement of 2 mm of the first horn in the longitudinal direction;
- `HornADisplacetransevrese`: displacement of 0.5 mm of the first horn in the transverse direction;
- `HornAEccentricityXInducedBField`: eccentric (off-axis) deformation of 0.035 mm of the Inner Conductor of the first horn;
- `HornAEllipticityXInducedBField`: elliptical deformation of 0.120 mm of the Inner Conductor of the first horn;

- `HornATiltTransverse`: upstream and downstream ends of the first hon shifted by 0.5 mm;
- `HornBDisplaceLongitudinalZ`: displacement of 3 mm of the first horn in the longitudinal direction;
- `HornBDisplaceTransverse`: displacement of 0.5 mm of the first horn in the transverse direction;
- `HornBEllipticityXInducedBField`: elliptical deformation of 0.120 mm of the Inner Conductor of the second horn by 0.180 mm;
- `HornBTiltTransverse`: upstream and downstream ends of the second horn shifted by 0.5 mm;
- `HornCDisplaceLongitudinalZ`: displacement of 3 mm of the third horn in the longitudinal direction;
- `HornCDisplaceTransverse`: displacement of 0.5 mm of the third horn in the transverse direction;
- `HornCEccentricityXInducedBField`: eccentric (off-axis) deformation of 0.070 mm of the Inner Conductor of the third horn;
- `HornCEllipticityXInducedBField`: elliptical deformation of 0.120 mm of the Inner Conductor of the third horn by 0.180 mm;
- `HornCTiltTransverse`: upstream and downstream ends of the third horn shifted by 0.5 mm;
- `HornCurrent`: simultaneous change of all three horns current from the nominal 300 kA by a shift of 3 kA;
- `HornWaterLayerThickness`: simultaneous change of all three horn from a nominal 1 mm by a shift of 0.5 mm;
- `ProtonBeamAngle`: shift of $\delta\theta = 70\,\mu\text{rad}$ $\phi = 0, \pi, \pm\pi/2$ of the proton beam angle keeping the target interaction point fixed to center of target;
- `ProtonBeamRadius`: change X and Y sigmoid simultaneously of 0.27 mm;
- `ProtonBeamTransverse`: interaction position shifted by 0.5 mm;
- `TargetDensity`: approximate target degradation of 2% (0.0356g/cm^3);
- `TargetDisplaceTransverse`: displacement of 0.5 mm of the target position;
- `TargetLength`: target length changed by 1.5 mm;
- `TargetTiltTransverse`: upstream and downstream ends shifted in opposite direction by 0.5 mm;
- `DecayPipeLength`: decay pipe length changed by 2.5 cm.

Variations	KS		shape KS		shape AD	
	POT	time	POT	time	POT	time
BaffletScrapingInX_pos_1_sigma	$1.1 \cdot 10^{16}$	176 s	$1.2 \cdot 10^{16}$	192 s	$7.9 \cdot 10^{15}$	126 s
BaffletScrapingInX_neg_1_sigma	$1.1 \cdot 10^{16}$	176 s	$1.2 \cdot 10^{16}$	192 s	$7.9 \cdot 10^{15}$	126 s
BaffletScrapingInY_pos_1_sigma	$1.1 \cdot 10^{16}$	176 s	$1.2 \cdot 10^{16}$	192 s	$7.9 \cdot 10^{15}$	126 s
BaffletScrapingInY_neg_1_sigma	$1.1 \cdot 10^{16}$	176 s	$1.2 \cdot 10^{16}$	192 s	$7.9 \cdot 10^{15}$	126 s

Variations	KS		shape KS		shape AD	
	POT	time	POT	time	POT	time
BaffletScrapingInX_pos_1_sigma	$1.31 \cdot 10^{16}$	208 s	$1.56 \cdot 10^{16}$	250 s	$9 \cdot 10^{15}$	144 s
BaffletScrapingInX_neg_1_sigma	$1.31 \cdot 10^{16}$	208 s	$1.56 \cdot 10^{16}$	250 s	$9 \cdot 10^{15}$	144 s
BaffletScrapingInY_pos_1_sigma	$1.31 \cdot 10^{16}$	208 s	$1.56 \cdot 10^{16}$	250 s	$9 \cdot 10^{15}$	144 s
BaffletScrapingInY_neg_1_sigma	$1.31 \cdot 10^{16}$	208 s	$1.56 \cdot 10^{16}$	250 s	$9 \cdot 10^{15}$	144 s

Variations	KS		shape KS		shape AD	
	POT	time	POT	time	POT	time
BaffletScrapingInX_pos_1_sigma	$2.13 \cdot 10^{16}$	341 s	$3.14 \cdot 10^{16}$	502 s	$1.55 \cdot 10^{16}$	248 s
BaffletScrapingInX_neg_1_sigma	$2.13 \cdot 10^{16}$	341 s	$3.14 \cdot 10^{16}$	502 s	$1.55 \cdot 10^{16}$	248 s
BaffletScrapingInY_pos_1_sigma	$2.13 \cdot 10^{16}$	341 s	$3.14 \cdot 10^{16}$	502 s	$1.55 \cdot 10^{16}$	248 s
BaffletScrapingInY_neg_1_sigma	$2.13 \cdot 10^{16}$	341 s	$3.14 \cdot 10^{16}$	502 s	$1.55 \cdot 10^{16}$	248 s

For the other variations, the statistics are too low to achieve p-values below the established thresholds (0.1, 0.05, 0.01). Therefore, we can put only lower limits on them: more than 4.4×10^{18}, or 20 hours of data taking, are required to resolve them.

In the following table, results of all p-values from tests are reported. We used the entire nominal sample, that corresponds to 4.4×10^{18} POT or, in other words, 20 hours of data taking.

Variations	KS	shape KS	shape AD
BaffletScrapingInX_pos_1_sigma	$< 10^{-15}$	$< 10^{-15}$	$< 10^{-15}$
BaffletScrapingInX_neg_1_sigma	$< 10^{-15}$	$< 10^{-15}$	$< 10^{-15}$
BaffletScrapingInY_pos_1_sigma	$< 10^{-15}$	$< 10^{-15}$	$< 10^{-15}$
BaffletScrapingInY_neg_1_sigma	$< 10^{-15}$	$< 10^{-15}$	$< 10^{-15}$
HornCurrent_pos_1_sigma	0.999	0.994	0.867
HornCurrent_neg_1_sigma	0.999	0.999	0.937
HornWaterLayerThickness_pos_1_sigma	1	1	1
HornWaterLayerThickness_neg_1_sigma	0.999	0.998	0.951
ProtonBeamRadius_pos_1_sigma	0.995	0.922	0.469
ProtonBeamRadius_neg_1_sigma	0.999	0.998	0.846
DecayPipe3SegmentBowingX(Y)_pos(neg)_1_sigma	1	1	1
DecayPipeDisplaceTransverseX(Y)_pos(neg)_1_sigma	1	1	1
DecayPipeEllipticalCrossSectionXA(YB)_pos(neg)_1_sigma	1	1	1
DecayPipeGeoBField_pos(neg)_1_sigma	1	1	1
DecayPipeRadius_pos(neg)_1_sigma	1	1	1
DecayPipeTiltX(Y)_DSOA_pos(neg)_1_sigma	1	1	1
HornADisplaceLongitudinalZ_pos(neg)_1_sigma	1	1	1
HornADisplaceTransverseX(Y)_pos(neg)_1_sigma	1	1	1
HornAEccentricityXInducedBField_pos(neg)_1_sigma	1	1	1
HornAEllipticityXInducedBField_pos(neg)_1_sigma	1	1	1
HornATiltTransverseX(Y)_pos(neg)_1_sigma	1	1	1
HornBDisplaceLongitudinalZ_pos(neg)_1_sigma	1	1	1
HornBDisplaceTransverseX(Y)_pos(neg)_1_sigma	1	1	1
HornBEllipticityXInducedBField_pos(neg)_1_sigma	1	1	1
HornBTiltTransverseX(Y)_pos(neg)_1_sigma	1	1	1
HornCDisplaceLongitudinalZ_pos(neg)_1_sigma	1	1	1
HornCDisplaceTransverseX(Y)_pos(neg)_1_sigma	1	1	1
HornCEccentricityXInducedBField_pos(neg)_1_sigma	1	1	1
HornCEllipticityXInducedBField_pos(neg)_1_sigma	1	1	1
HornCTiltTransverseX(Y)_pos(neg)_1_sigma	1	1	1
ProtonBeamAngleX(Y)_pos(neg)_1_sigma	1	1	1
ProtonBeamTransverseX(Y)_pos(neg)_1_sigma	1	1	1
TargetDensity_pos(neg)_1_sigma	1	1	1
TargetDisplaceTransverseX(Y)_pos(neg)_1_sigma	1	1	1
TargetLength_pos(neg)_1_sigma	1	1	1
TargetTiltTransverseX(Y)_pos(neg)_1_sigma	1	1	1
DecayPipeLength_pos(neg)_1_sigma	1	1	1

Bibliography

[1] Atlas Collaboration et al. Observation of a new particle in the search for the standard model higgs boson with the atlas detector at the lhc. *arXiv preprint arXiv:1207.7214*, 2012.

[2] Pushpalatha C Bhat, CMS Collaboration, et al. Observation of a higgs-like boson in cms at the lhc. *Nuclear Physics B-Proceedings Supplements*, 234:7–14, 2013.

[3] Corey Adams, David Adams, Tarek Akiri, Tyler Alion, Kris Anderson, Costas Andreopoulos, Mike Andrews, Ioana Anghel, João Carlos Costa dos Anjos, Maddalena Antonello, et al. The long-baseline neutrino experiment: exploring fundamental symmetries of the universe. *arXiv preprint arXiv:1307.7335*, 2013.

[4] E. Ambler, R. W. Hayward, D. D. Hoppes, R. P. Hudson, and C. S. Wu. Further experiments on β decay of polarized nuclei. *Phys. Rev.*, 106:1361–1363, Jun 1957.

[5] Carlo Giunti and Chung W Kim. *Fundamentals of neutrino physics and astrophysics*. Oxford university press, 2007.

[6] Ettore Majorana. Teoria simmetrica dell'elettrone e del positrone. *Il Nuovo Cimento (1924-1942)*, 14(4):171–184, 1937.

[7] DQ Adams, C Alduino, F Alessandria, K Alfonso, E Andreotti, FT Avignone III, O Azzolini, M Balata, I Bandac, TI Banks, et al. Cuore opens the door to tonne-scale cryogenics experiments. *Progress in Particle and Nuclear Physics*, 122:103902, 2022.

[8] Carlo Giunti. Theory of neutrino oscillations. In *Particle Physics in Laboratory, Space and Universe*, pages 35–44. World Scientific, 2005.

[9] Carlo Giunti and Marco Laveder. The physical significance of confidence intervals. *International Journal of Modern Physics C*, 12(08):1155–1168, 2001.

[10] Max Aker, Konrad Altenmüller, M Arenz, M Babutzka, J Barrett, S Bauer, M Beck, A Beglarian, J Behrens, T Bergmann, et al. Improved upper limit on the neutrino mass from a direct kinematic method by katrin. *Physical review letters*, 123(22):221802, 2019.

[11] Kai Zuber. *Neutrino physics*. Taylor & Francis, 2020.

[12] K Abe, H Aihara, A Ajmi, C Andreopoulos, M Antonova, S Aoki, Y Asada, Y Ashida, A Atherton, E Atkin, et al. T2k nd280 upgrade–technical design report. *arXiv preprint arXiv:1901.03750*, 2019.

[13] Francesca Di Lodovico, Hyper-Kamiokande Collaboration, et al. The hyper-kamiokande experiment. In *Journal of physics: conference series*, volume 888, page 012020. IOP Publishing, 2017.

[14] MA Acero, P Adamson, L Aliaga, N Anfimov, A Antoshkin, E Arrieta-Diaz, Lily Asquith, A Aurisano, A Back, C Backhouse, et al. Improved measurement of neutrino oscillation parameters by the nova experiment. *Physical Review D*, 106(3):032004, 2022.

[15] John N Bahcall and Carlos Pena-Garay. Solar models and solar neutrino oscillations. *New Journal of Physics*, 6(1):63, 2004.

[16] Bruce T Cleveland, Timothy Daily, Raymond Davis Jr, James R Distel, Kenneth Lande, CK Lee, Paul S Wildenhain, and Jack Ullman. Measurement of the solar electron neutrino flux with the homestake chlorine detector. *The Astrophysical Journal*, 496(1):505, 1998.

[17] Wolfgang Hampel, J Handt, G Heusser, J Kiko, T Kirsten, M Laubenstein, E Pernicka, W Rau, M Wojcik, Yu Zakharov, et al. Gallex solar neutrino observations: Results for gallex iv. *Physics Letters B*, 447(1-2):127–133, 1999.

[18] Yoichiro Suzuki. The super-kamiokande experiment. *The European Physical Journal C*, 79:1–18, 2019.

[19] Alain Bellerive, JR Klein, AB McDonald, AJ Noble, AWP Poon, SNO Collaboration, et al. The sudbury neutrino observatory. *Nuclear Physics B*, 908:30–51, 2016.

[20] Q Retal Ahmad, RC Allen, TC Andersen, JD Anglin, JC Barton, EW Beier, M Bercovitch, J Bigu, SD Biller, RA Black, et al. Direct evidence for neutrino flavor transformation from neutral-current interactions in the sudbury neutrino observatory. *Physical review letters*, 89(1):011301, 2002.

[21] Takaaki Kajita. Discovery of atmospheric neutrino oscillations. *Int. J. Mod. Phys. A*, 31:1630047, 2016.

[22] Roger Wendell, Super-Kamiokande Collaboration, et al. Atmospheric results from super-kamiokande. In *AIP Conference Proceedings*, volume 1666. AIP Publishing, 2015.

[23] Toshiyuki Toshito et al. Super-kamiokande atmospheric neutrino results. *arXiv preprint hep-ex/0105023*, 2001.

[24] Frederick Reines and Clyde L Cowan. The neutrino. In *Neutrinos And Other Matters: Selected Works of Frederick Reines*, pages 548–551. World Scientific, 1991.

[25] KamLAND& Eguchi, S Enomoto, K Furuno, J Goldman, H Hanada, H Ikeda, K Ikeda, K Inoue, K Ishihara, W Itoh, et al. First results from kamland: evidence for reactor antineutrino disappearance. *Physical review letters*, 90(2):021802, 2003.

[26] Takeshi Araki, K Eguchi, S Enomoto, K Furuno, K Ichimura, H Ikeda, K Inoue, K Ishihara, T Iwamoto, T Kawashima, et al. Measurement of neutrino oscillation with kamland: Evidence of spectral distortion. *Physical review letters*, 94(8):081801, 2005.

[27] E Aliu, S Andringa, S Aoki, J Argyriades, K Asakura, R Ashie, H Berns, H Bhang, A Blondel, S Borghi, et al. Evidence for muon neutrino oscillation in an accelerator-based experiment. *Physical Review Letters*, 94(8):081802, 2005.

[28] Ivan Esteban, MC Gonzalez-Garcia, Michele Maltoni, Ivan Martinez-Soler, João Paulo Pinheiro, and Thomas Schwetz. Nufit-6.0: Updated global analysis of three-flavor neutrino oscillations. *Journal of High Energy Physics*, 2024(12):1–33, 2025.

[29] JUNO collaboration et al. Juno physics and detector. *Progress in Particle and Nuclear Physics*, 123:103927, 2022.

[30] Babak Abi, Roberto Acciarri, Mario A Acero, Giorge Adamov, David Adams, Marco Adinolfi, Zubayer Ahmad, Jhanzeb Ahmed, Tyler Alion, S Alonso Monsalve, et al. Volume i. introduction to dune. *Journal of instrumentation*, 15(08):T08008, 2020.

[31] S. Navas et al. Review of particle physics. *Phys. Rev. D*, 110(3):030001, 2024.

[32] Babak Abi, Roberto Acciarri, Mario A Acero, Giorge Adamov, David Adams, Marco Adinolfi, Zubayer Ahmad, Jhanzeb Ahmed, Tyler Alion, S Alonso Monsalve, et al. Deep underground neutrino experiment (dune), far detector technical design report, volume ii: Dune physics. *arXiv preprint arXiv:2002.03005*, 2020.

[33] James Strait, Elaine McCluskey, Tracy Lundin, Joshua Willhite, Thomas Hamernik, Vaia Papadimitriou, Alberto Marchionni, Min Jeong Kim, Marzio Nessi, David Montanari, et al. Long-baseline neutrino facility (lbnf) and deep underground neutrino experiment (dune) conceptual design report volume 3: Long-baseline neutrino facility for dune june 24, 2015. *arXiv preprint arXiv:1601.05823*, 2016.

[34] A Abed Abud, Babak Abi, Roberto Acciarri, Mario A Acero, Giorge Adamov, David Adams, Marco Adinolfi, Antoni Aduszkiewicz, Zubayer Ahmad, Jhanzeb Ahmed, et al. Deep underground neutrino experiment (dune) near detector conceptual design report. *Instruments*, 5(4):31, 2021.

[35] M Auger, A Ereditato, and JR Sinclair. Argoncube: A modular approach for liquid argon tpc neutrino detectors for near detector environments. Technical report, 2017.

[36] C Rubbia, M Antonello, P Aprili, B Baibussinov, M Baldo Ceolin, L Barze, P Benetti, E Calligarich, N Canci, Francesco Carbonara, et al. Underground operation of the icarus t600 lar-tpc: first results. *Journal of Instrumentation*, 6(07):P07011, 2011.

[37] Oliver Lantwin. The dune vertical drift tpc. *arXiv preprint arXiv:2211.11339*, 2022.

[38] Babak Abi, Roberto Acciarri, Mario A Acero, Giorge Adamov, David Adams, Marco Adinolfi, Zubayer Ahmad, Jhanzeb Ahmed, Tyler Alion, S Alonso Monsalve, et al. Volume iv. the dune far detector single-phase technology. *Journal of instrumentation*, 15(08):T08010, 2020.

[39] Sabrina Sacerdoti. A lartpc with vertical drift for the dune far detector. Technical report, Fermi National Accelerator Lab.(FNAL), Batavia, IL (United States), 2022.

[40] Laura Paulucci, DUNE collaboration, et al. The dune vertical drift photon detection system. *Journal of Instrumentation*, 17(01):C01067, 2022.

[41] Dune Collaboration et al. The dune far detector vertical drift technology technical design report. *Journal of Instrumentation*, 19(8):T08004, 2024.

[42] A Abed Abud, B Abi, R Acciarri, MA Acero, MR Adames, G Adamov, M Adamowski, D Adams, M Adinolfi, C Adriano, et al. Snowmass neutrino frontier: Dune physics summary. *arXiv preprint arXiv:2203.06100*, 2022.

[43] DUNE Collaboration, R Acciarri, MA Acero, M Adamowski, C Adams, P Adamson, S Adhikari, Z Ahmad, CH Albright, T Alion, et al. Long-baseline neutrino facility (lbnf) and deep underground neutrino experiment (dune) conceptual design report volume 2: The physics program for dune at lbnf. *arXiv*, 2015.

[44] Wojciech Krzemien and Elena Pérez Del Río. The kloe-2 experiment: Overview of recent results. *International Journal of Modern Physics A*, 34(25):1930012, 2019.

[45] V Pia, DUNE collaboration, et al. Reconstruction of neutrino interactions in sand with an innovative liquid argon imaging detector. *Journal of Instrumentation*, 19(02):C02073, 2024.

[46] P Bernardini, S Bertolucci, S Biagi, A Caminata, A Cervelli, S Davini, S Di Domizio, C Distefano, S Di Noto, H Duyang, et al. A proposal to enhance the dune near-detector complex v6. 6. 2019.

[47] Kevin Scott McFarland, T Adams, A Alton, S Avvakumov, L de Barbaro, P de Barbaro, RH Bernstein, A Bodek, T Bolton, J Brau, et al. Measurement of sin2thetaw from neutrino-nucleon scattering at nutev. *Arxiv preprint hep-ex/9806013*, 1998.

[48] C Andreopoulos. The genie universal, object-oriented neutrino generator. *Nuclear Physics B-Proceedings Supplements*, 159:217–222, 2006.

[49] Costas Andreopoulos, A Bell, D Bhattacharya, F Cavanna, J Dobson, S Dytman, H Gallagher, P Guzowski, R Hatcher, P Kehayias, et al. The genie neutrino monte carlo generator. *Nuclear Instruments and Methods in Physics Research Section A: Accelerators, Spectrometers, Detectors and Associated Equipment*, 614(1):87–104, 2010.

[50] Robert Hatcher. Proposal for a unified flux n-tuple format. *MINOS Internal Document*, pages 9070–v4, 2012.

[51] Costas Andreopoulos, Christopher Barry, Steve Dytman, Hugh Gallagher, Tomasz Golan, Robert Hatcher, Gabriel Perdue, and Julia Yarba. The genie neutrino monte carlo generator: physics and user manual. *arXiv preprint arXiv:1510.05494*, 2015.

[52] `https://github.com/brettviren/gegede`.

[53] `https://root.cern/`.

[54] Sea Agostinelli, John Allison, K al Amako, John Apostolakis, Henrique Araujo, Pedro Arce, Makoto Asai, D Axen, Swagato Banerjee, GJNI Barrand, et al. Geant4—a simulation toolkit. *Nuclear instruments and methods in physics research section A: Accelerators, Spectrometers, Detectors and Associated Equipment*, 506(3):250–303, 2003.

[55] John Allison, Katsuya Amako, JEA Apostolakis, HAAH Araujo, P Arce Dubois, MAAM Asai, GABG Barrand, RACR Capra, SACS Chauvie, RACR Chytracek, et al. Geant4 developments and applications. *IEEE Transactions on nuclear science*, 53(1):270–278, 2006.

[56] `https://github.com/gyang9/dunendggd`.

[57] `https://github.com/ClarkMcGrew/edep-sim`.

[58] Yoshinari Hayato. A neutrino interaction simulation program library neut. *Acta Physica Polonica B*, 40(9), 2009.

[59] `https://github.com/DUNE/sandreco`.

[60] `https://root.cern.ch/doc/master/classTTree.html`.

[61] M Adinolfi, Fabio Ambrosino, A Antonelli, M Antonelli, F Anulli, G Barbiellini, G Bencivenni, S Bertolucci, Cesare Bini, C Bloise, et al. The kloe electromagnetic calorimeter. *Nuclear Instruments and Methods in Physics Research Section A: Accelerators, Spectrometers, Detectors and Associated Equipment*, 482(1-2):364–386, 2002.

[62] `http://www2.sica.unimi.it/andreazz/AATrackingSystems.pdf`.

[63] Pierce Weatherly. G4lbnf neutrino beam focusing uncertainties update. `https://indico.fnal.gov/event/44538/contributions/192084/attachments/131838/161596/20200723_BeamFocusingUncert.pdf`.

[64] https://root.cern.ch/doc/master/classTH1.html.

[65] Frank C Porter. Testing consistency of two histograms. *arXiv preprint arXiv:0804.0380*, 2008.

[66] John Winsor Pratt and Jean Dickinson Gibbons. *Concepts of nonparametric theory*. Springer Science & Business Media, 2012.

[67] Fritz W Scholz and Michael A Stephens. K-sample anderson–darling tests. *Journal of the American Statistical Association*, 82(399):918–924, 1987.